

Sohail

by Chairperson PublicAdmn

Submission date: 10-Jan-2018 03:05PM (UTC+0530)

Submission ID: 890423940

File name: Thesis.pdf (4.3M)

Word count: 38015

Character count: 186260

5
**DIFFERENTIAL CROSS SECTION MEASUREMENT OF
Z BOSON IN LEPTONIC DECAYS AT $\sqrt{s} = 13$ TeV
WITH CMS DETECTOR AT LHC**

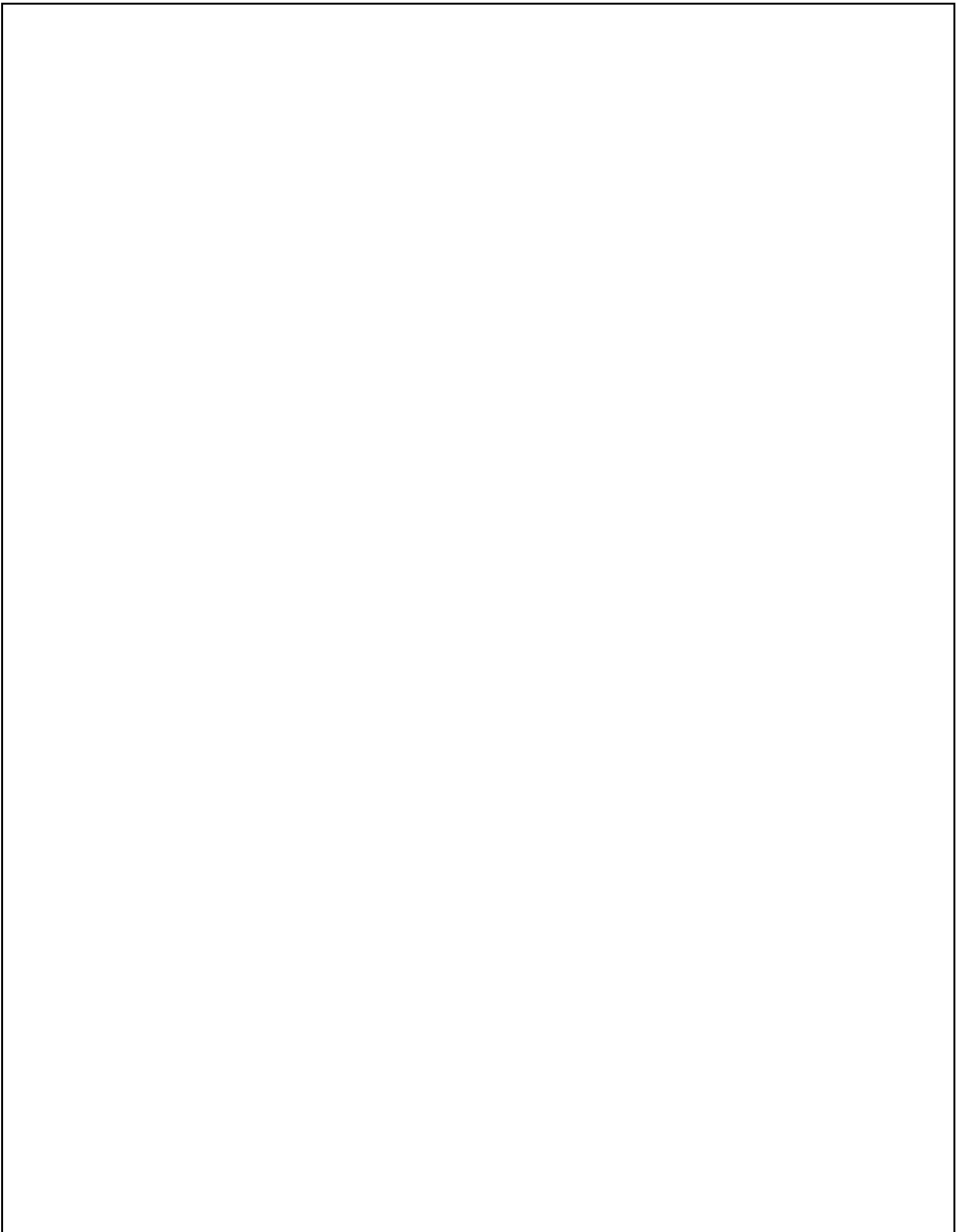
87
A THESIS

Submitted to the
FACULTY OF SCIENCE
PANJAB UNIVERSITY, CHANDIGARH
for the degree of
DOCTOR OF PHILOSOPHY

2018

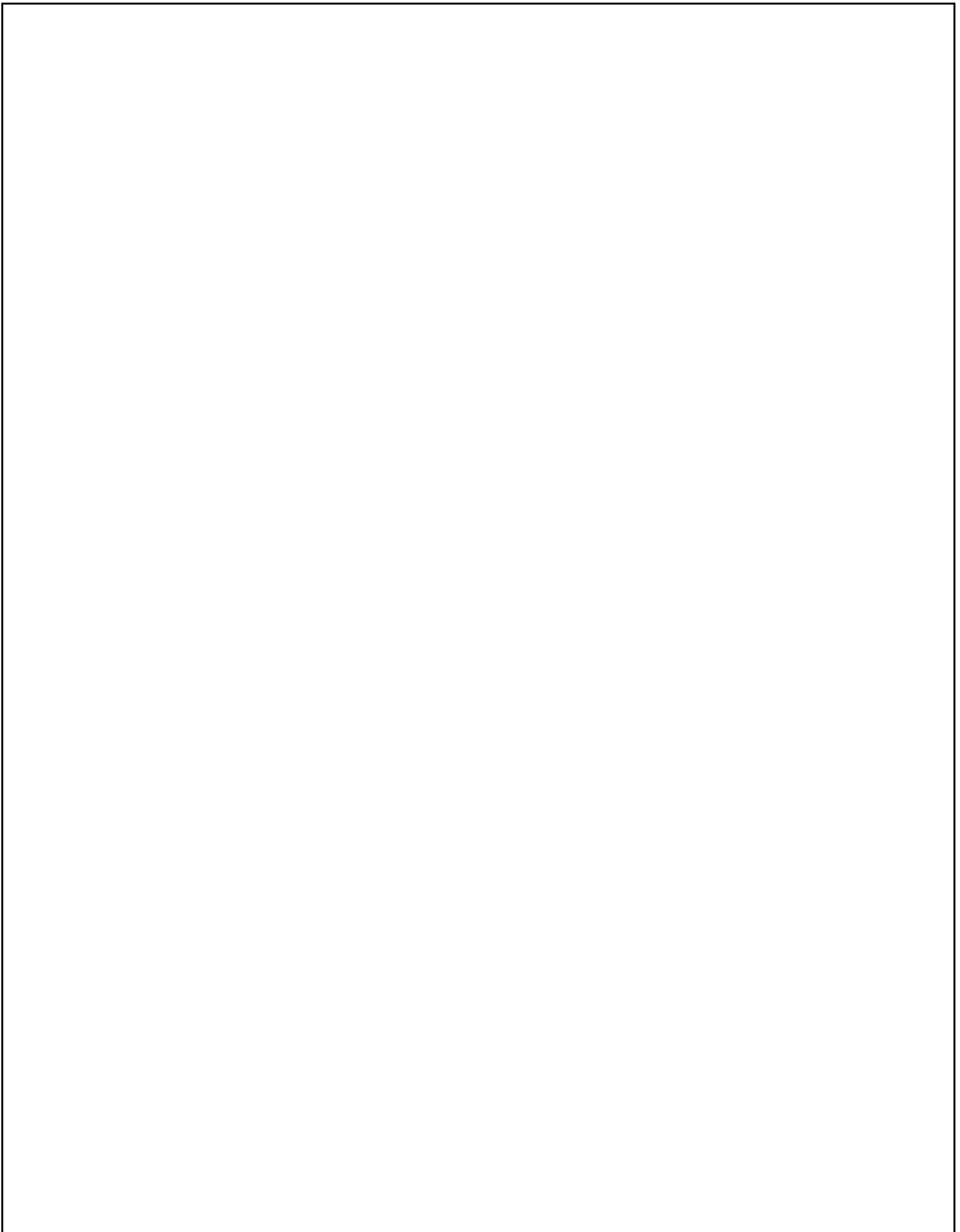
Ridhi Chawla

DEPARTMENT OF PHYSICS
CENTRE OF ADVANCED STUDY IN PHYSICS
PANJAB UNIVERSITY, CHANDIGARH
INDIA

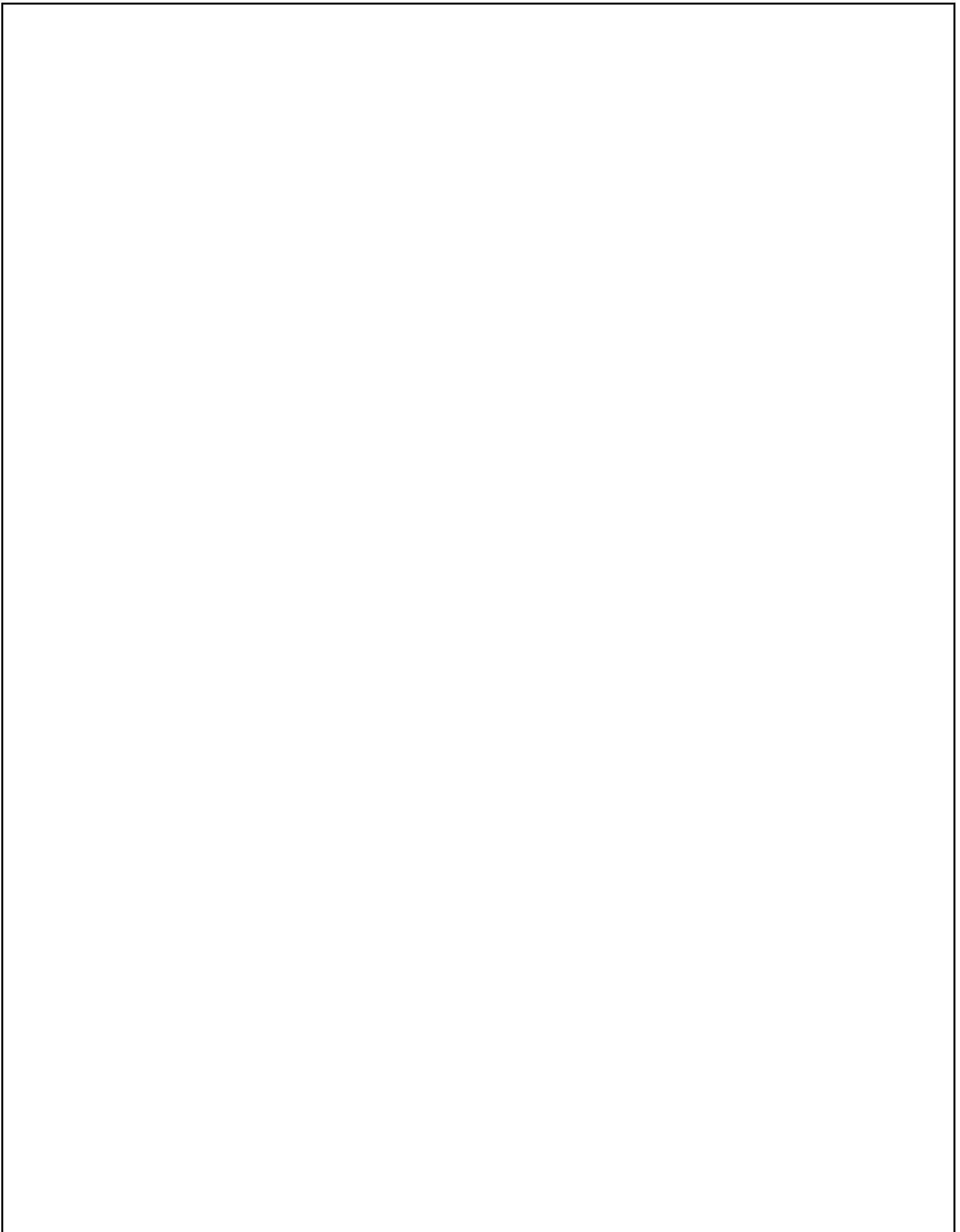


Dedicated to

My Loving Parents



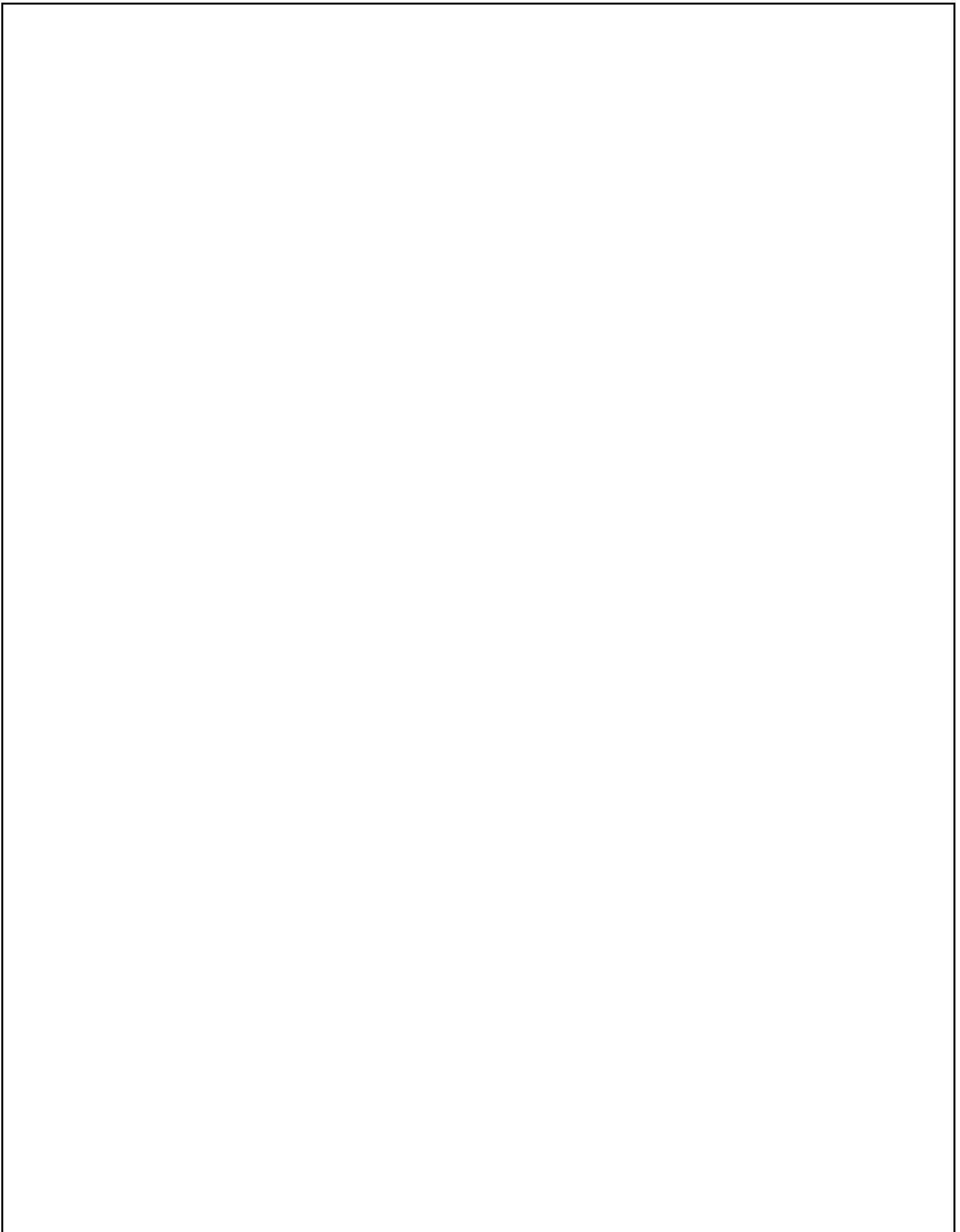
Acknowledgements



Abstract

The proton-proton collisions in the Large Hadron Collider (LHC) build at the European Center for Nuclear Research (CERN) is the begining of a new era in the physics at high energies. It allows to test the predictions of the Standard Model with high precision and to search for new physics which has yet not been explored.

In this thesis, the differential cross section measurement of the Drell-Yan process, $q\bar{q} \rightarrow \gamma^*/Z \rightarrow e^+e^-$, using the proton-proton collision data collected by the Compact Muon Solenoid (CMS) experiment during the year 2015 is reported. The analyzed data corresponds to an integrated luminosity of 2.3 fb^{-1} at the center-of-mass energy $\sqrt{s} = 13 \text{ TeV}$ at the LHC. The production cross section of the Drell-Yan process is well established up to next-to-next leading order accuracy and provides the very first validation of the Standard Model at this new energy arena. The Drell-Yan process is an irreducible background to many searches beyond the Standard Model, including the high-mass dilepton resonance, Higgs and other exotica searches, which makes it neccessary to accurately measure the production of the Drell-Yan process with the LHC data. Hence, in the present work, the Drell-Yan production cross section has been measured in the electron final state. The cross section measurement is performed in the bins of dielectron invariant mass in the range $15 < m < 3000 \text{ GeV}$. The measured yield is corrected for the migration effects due to limited detector resolution, coverage of detector, selection inefficiencies and the final state radiation effects. The experimental cross section is computed in the full phase space and in the detector acceptance region. The results are compared with various theoretical predictions of the Standard Model available at next-to-leading order and next-to-next-to-leading order.



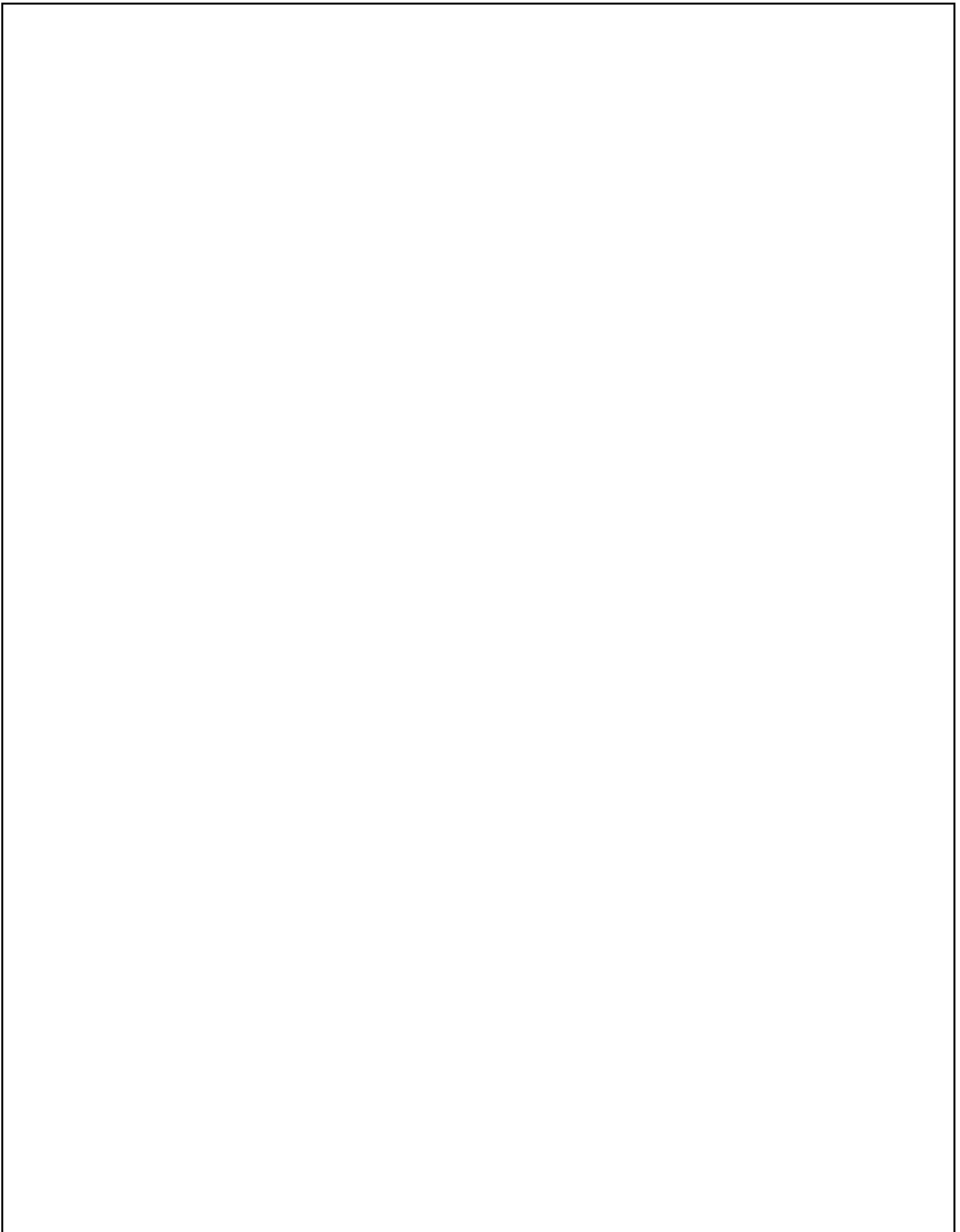
Contents

¹⁷⁰ List of Figures	xv
<hr/>	
List of Tables	xxiii
<hr/>	
¹⁰⁰ 1 Introduction	1
2 Theory	5
2.1 The Standard Model	5
2.1.1 Electroweak Theory	8
2.1.2 Quantum Chromodynamics	11
2.2 Proton-Proton Collisions	13
2.2.1 Structure of Protons	14
2.2.2 Underlying Events and Pileup Contribution	15
2.3 Drell-Yan Production	17
2.3.1 Cross Section	17
2.3.2 Perturbative QCD Corrections	20
3 Experimental Details	23
3.1 The Large Hadron Collider	23
3.1.1 LHC Design	24

3.1.2	Luminosity and Machine Parameters	26
124		
3.1.3	The Compact Muon Solenoid	27
3.1.4	Coordinate Conventions	29
3.1.5	Superconducting Magnet	31
26		
3.1.6	Inner Tracking System	31
3.1.7	Electromagnetic Calorimeter	34
3.1.8	Hadron Calorimeter	36
3.1.9	Muon System	40
3.1.10	Trigger System	43
35		
3.1.10.1	Level 1 Trigger	44
3.1.10.2	High Level Trigger	44
3.1.10.3	Electron Trigger	45
4	Event Simulation and Reconstruction	49
		47
4.1	Event Generators	48
4.2	Detector Simulation	50
4.3	Event Reconstruction	51
4.3.1	Primary Vertex Reconstruction	52
4.3.2	Pileup Reweighting	53
4.3.3	Electron Reconstruction	54
4.3.3.1	Clustering	54
4.3.3.2	Track Reconstruction	56
4.3.4	Energy Scale Corrections	57
4.3.5	Electron Selection Strategy	58
4.3.5.1	Identificaton	58
4.3.5.2	Isolation	59

4.3.6	Software and Computing	60
4.3.6.1	CMSSW	60
4.3.6.2	ROOT	61
4.3.6.3	Computing Model	61
5	Measurement of Drell-Yan Differential Cross section	62
5.1	Data and Monte Carlo Samples	63
5.1.1	Collision Data	63
5.1.2	Drell-Yan Signal	63
5.1.3	Background Processes	65
5.2	Reweighting	68
5.2.1	Pileup Reweighting	69
5.2.2	Scale Corrections	69
5.3	Drell-Yan Event Selection	70
5.4	Background Estimation	74
5.4.1	Measurement of Dielectron Background using $e\mu$ Method	75
5.4.2	Measurement of Dielectron Background using Fake Rate Method	79
5.5	Corrections	85
5.5.1	Unfolding	86
5.5.2	Acceptance and Efficiency	88
5.5.3	Selection Efficiency	89
5.5.3.1	Reconstruction Efficiency	91
5.5.3.2	Identification and Isolation Efficiency	92
5.5.3.3	Trigger Efficiency	93

5.5.4	Final State Radiation Effects	94
81 5.6	Systematic Uncertainties	96
5.6.1	Luminosity Uncertainty	96
5.6.2	Statistical Uncertainty	96
5.6.3	Scale Correction	97
5.6.4	Background Estimation	97
5.6.5	Detector Resolution	98
5.6.6	Acceptance Correction	99
5.6.7	Efficiency Correction	99
5.6.8	FSR Correction	101
5.6.9	Total Uncertainty	101
6	Results	103
6.1	Z-peak Cross section Measurement	103
6.2	Differential Cross section Measurement	104
7	Summary	112
Appendix A		115
2 A.1	Summary of the systematic uncertainties for $d\sigma/dm$ measurement . .	116
2 A.2	Summary of the results for full phase space $d\sigma/dm$ measurement in dielectron channel	118
2 A.3	Summary of the results for post-FSR $d\sigma/dm$ measurement in dielectron channel	120
2 A.4	Summary of the results for full phase space $d\sigma/dm$ measurement in combined channel	122
List of publications		125



³²

List of Figures

2.1	The elementary particles of the Standard Model	6
2.2	A symbolic representation of the DGLAP evolution equation for quark	14
2.3	The parton distribution functions for quarks, anti-quarks and gluons for energy scale $Q^2 = 1.9 \text{ GeV}^2$ (left) and $Q^2 = 10 \text{ GeV}^2$ (right). The distributions are determined from the H1 and ZEUS Collaborations from global fits to data.	15
2.4	A schematic representation of $2 \rightarrow 2$ hard scattering event.	16
2.5	The Drell-Yan $q\bar{q} \rightarrow Z/\gamma^* \rightarrow l^+l^-$ production in a proton-proton collision [11]. $P_{1,2}$ are the four-momenta of the protons, $p_{1,2}$ are the four-momenta of the partons initiating the hard scattering, depending on the momentum fractions $x_{1,2}$	17
2.6	The LO and NLO feynman diagrams for the Drell-Yan process. The solid lines represent quarks or anti-quarks, the spiral lines represent gluons and the wavy lines correspond to Z/γ^*	20
3.1	Accelerator Complex at CERN.	25
3.2	Total integrated luminosity in 2015.	27
3.3	A schematic diagram of Compact Muon Solenoid.	28
3.4	Relation between the polar angle and pseudorapidity.	30
3.5	CMS tracking system.	32

3.6 Tracker material thickness ⁵ as a function of η , expressed in relative radiation length x/X_0 of the different components of the tracker.	33
⁵⁷ 3.7 Layout of the CMS Electromagnetic Calorimeter showing the arrangement of crystal modules, supermodules and endcaps with the preshower detector in front of it.	34
3.8 Longitudinal view of CMS Electromagnetic Calorimeter.	35
3.9 CMS Hadron calorimeter.	37
3.10 The layers of Hadron Outer.	39
3.11 CMS Muon Chambers.	41
3.12 CMS Trigger and Data Acquisition System.	44
4.1 Flowchart of the electron reconstruction chain.	54
4.2 Domino construction step in the Hybrid algorithm used in the barrel region of Electromagnetic Calorimeter.	55
²⁹ 5.1 Leading order Feynman diagram of Drell-Yan process.	63
5.2 Generator-level mass distribution of the Drell-Yan signal sample (using aMC@NLO generator). Dielectron mass is constructed by two electrons with “isHardProcess” Gen-Flag.	65
⁷⁸ 5.3 Leading order Feynman diagram for τ decay.	66
⁷⁴ 5.4 Leading order Feynman diagram for the $t\bar{t}$ pair production.	66
¹¹ 5.5 Leading order Feynman diagrams of the single top processes. From left to right: s-channel, t-channel and tW-channel.	⁹ 67
⁵⁷ 5.6 Leading order Feynman diagram for diboson production contributions from s-channel (left) and t-channel (right).	67
5.7 Leading order Feynman diagram for $W + jets$ production.	68

5.8	The distribution for number of reconstructed primary vertices in data (black circles) and Monte-Carlo prediction (histograms) before (left) and after (right) applying the pileup reweighting.	19 66 69
5.9	The left and right plots show the mass distribution for the Z -peak region, before and after applying the energy scale and smearing corrections respectively, for data (black circles) and Monte-Carlo prediction (yellow histogram). The Drell-Yan signal is normalized to the number of data events.	19 70
5.10	Electron identification variables for data (black circles) and Monte-Carlo prediction (histograms) listed in Table 5.2	72
5.11	Electron kinematic variables p_T , η and ϕ after pre-selection (kinematic and identification cuts) in data (black circles) and Monte-Carlo prediction (histograms).	73
5.12	Dielectron kinematic variables p_T , η and ϕ after pre-selection (kinematic and identification cuts) in data (black circles) and Monte-Carlo prediction (histograms).	74
5.13	Drell-Yan mass distribution in data (black circles) and Monte-Carlo prediction (histograms for signal and backgrounds) from 15 to 3000 GeV.	65 75
5.14	Kinematic variables p_T , η and ϕ for electron (left) and muon (right) candidates after pre-selection (kinematic and identification cuts for $e\mu$ selection) in data (black circles) and Monte-Carlo prediction (stack histograms).	80 77

5.15 Left: The number of observed e^+e^- events from Monte-Carlo prediction (stacked histograms) and the number of estimated e^+e^- events obtained from $e\mu$ MC (black circles). Right: The number of observed $e\mu$ events in data (black circles) and Monte-Carlo prediction (stacked histograms).	79
5.16 The number of observed e^+e^- events from Monte-Carlo prediction (stacked histograms) and the number of estimated e^+e^- events obtained from $e\mu$ data (black circles) using the $e\mu$ method.	80
5.17 E_T distribution of the HLT photon object before (red) and after (black) applying the trigger prescale. The distribution is common after $E_T = 175$ GeV, which is the maximum threshold of single photon trigger.	81
5.18 Electron fake rate obtained as a function of p_T in barrel and endcap regions separately, after performing the electroweak subtraction from Monte-Carlo prediction.	82
5.19 The number of e^+e^- events for QCD (left) and $W + jets$ (right) backgrounds estimated from data using the fake rate method.	83
5.20 The observed dielectron invariant mass spectra for data (black circles) and Monte-Carlo (stacked histograms) events and the corresponding ratio of observed to expected yields. EW means the contribution from WW, WZ, ZZ and $DY \rightarrow \tau\tau$, Fakes corresponds to the contribution from QCD and $W + jets$	84
5.21 The fraction of the number of dielectron events from each background process with respect to the total observed number of data events. 'Total' corresponds to the combined fraction for all the backgrounds estimated from data-driven methods and Monte-Carlo simulation.	85

5.22 The response matrix computed within the detector acceptance from aMC@NLO simulation to unfold the background subtracted yield.	87
5.23 Closure test: The comparison of measured (reco-level) distribution and unfolded yield from Monte-Carlo simulation to the true (gen-level) distribution in bins of dielectron invariant mass using D'Agostini's iteration method with 21 iterations.	88
5.24 Detector acceptance, event efficiency and their product as a function of post-FSR dielectron invariant mass.	90
5.25 Reconstruction Efficiency in data and the corresponding scale factor obtained after dividing the efficiencies for data and Monte-Carlo simulation as a function of p_T (left) and supercluster η_{sc} (right).	91
5.26 Electron Identification and Isolation Efficiency in data and the corresponding scale factor obtained after dividing the efficiencies for data and Monte-Carlo simulation as a function of p_T (left) and supercluster η_{sc} (right).	92
5.27 HLT Efficiency for the trigger <i>HLT_Ele23_WP Loose_Gsf</i> in data and the corresponding scale factor obtained after dividing the efficiencies for data and Monte-Carlo simulation as a function of p_T (left) and electron η (right).	93
5.28 The response matrix computed in full phase space from aMC@NLO simulation to correct for the Final State Radiation (FSR) effects using the iterative D'Agostini unfolding method.	94
5.29 Closure test: The comparison of gen-level (post-FSR) invariant mass distribution and FSR corrected unfolded yield from Monte-Carlo simulation to the dressed mass (pre-FSR) distribution in bins of dielectron invariant mass using D'Agostini's iteration method with 21 iterations.	95

5.30 The statistical, luminosity, acceptance and the total systematic (quadrature sum of efficiency scale factor (SF), detector resolution, background and FSR correction) uncertainties obtained in the bins of dielectron invariant mass.	102
6.1 The Drell-Yan differential cross section measurement corrected for radiation effects in full phase space as a function of dielectron invariant mass compared to the NNLO theoretical prediction from FEWZ (blue) and the NLO prediction MADGRAPH_AMC@NLO (red). The coloured band in the middle and bottom plots denotes theoretical uncertainty and the shaded band denotes the total uncertainty which is the combination of statistical, systematic and luminosity uncertainties. The error bar on the data points denote the statistical uncertainty only.	105
6.2 The Drell-Yan differential cross section measurement performed in the fiducial region without FSR correction as a function of dielectron invariant mass compared to the NLO theoretical prediction from MADGRAPH_AMC@NLO. The red band in the bottom plot denotes theoretical uncertainty and the shaded band denotes the total uncertainty which is the combination of statistical, systematic and luminosity uncertainties. The error bar on the data points denote the statistical uncertainty only.	106
6.3 The Drell-Yan differential cross section measurement performed as a function of dielectron invariant mass compared to the NNLO theoretical prediction from FEWZ for the full phase space. The data point abscissas are obtained according to eq. (6) in [112]. The bottom plot shows the ratio between data and theoretical prediction where the coloured box denotes theoretical uncertainty.	107

6.4 Ratio of theory to experimental data for the differential cross section as a function of dielectron invariant mass in the range $m < 200$ GeV (left) and $m > 200$ GeV (right). The blue band denotes the theoretical uncertainty on the ratio. In the right plot, the contribution from Photon Induced backgrounds is shown in red colour and has a visible effect in the high mass region.	107
6.5 Ratio between experimental result and theoretical prediction from various PDFs for $m > 200$ GeV. The coloured band in the plot denotes the theoretical uncertainty and the shaded band denotes the total experimental uncertainty excluding the luminosity uncertainty. The error bar on the data points denote the statistical uncertainty only.	108
6.6 The Drell-Yan differential cross section measurement performed as a function of dielectron invariant mass compared to the NNLO theoretical prediction from FEWZ for the full phase space. The data point abscissas are obtained according to eq. (6) in [112]. The bottom plot shows the ratio between data and theoretical prediction where the coloured box denotes theoretical uncertainty.	110
6.7 Ratio of theory to experimental data for the differential cross section as a function of dielectron invariant mass in the range $m < 200$ GeV (left) and $m > 200$ GeV (right). The blue band denotes the theoretical uncertainty on the ratio. In the right plot, the contribution from Photon Induced backgrounds is shown in red colour and has a visible effect in the high mass region.	110
6.8 Ratio between experimental result and theoretical prediction from various PDFs for $m > 200$ GeV. The coloured band in the plot denotes the theoretical uncertainty and the shaded band denotes the total experimental uncertainty excluding the luminosity uncertainty. The error bar on the data points denote the statistical uncertainty only.	111

List of Tables

2.1	The four fundamental forces in physics and their properties.	7
5.1	Names of the datasets and corresponding cross section values for the Monte-Carlo signal and background samples used.	64
5.2	Summary of Medium Working Point for the identification of electrons using cut-based approach in the barrel and endcap regions [96]. . . .	73
5.3	Summary of Tight Identification and Particle Flow Isolation for the selection of muon [97] for $e\mu$ method.	78
5.4	Total number of $e\mu$ and e^+e^- events observed in data and Monte-Carlo prediction and the estimated number of e^+e^- events from data and Monte-Carlo simulation, where all errors are statistical.	79
5.5	Total number of e^+e^- events observed in Monte-Carlo prediction and the estimated number of e^+e^- events from data.	83
5.6	Tag and Probe selection criteria for measuring the Identification and Isolation efficiency.	92
6.1	Absolute cross section measurements in full phase space and fiducial region (within the detector acceptance) for the Z -peak region ($60 < m < 120$ GeV) with associated uncertainties.	104

A.1	Summary of the systematic uncertainties for the differential cross section $d\sigma/dm$ measurement. ‘Total’ refers to the quadratic sum of all sources of uncertainties except for the uncertainty from acceptance correction.	117
A.2	Summary of the results for $d\sigma/dm$ measurement in dielectron channel. “Stat. Unc.” is the statistical uncertainty and “Exp. Unc.” means the systematic uncertainty from experimental part including the luminosity uncertainty. “Theo. Unc.” means the systematic uncertainty from theoretical part (PDF and variation of coupling constant). “Total” is a quadratic sum of statistical, experimental and theoretical uncertainties.	119
A.3	Summary of the results for the fiducial (post-FSR) $d\sigma/dm$ measurement in dielectron channel. “Stat. Unc.” is the statistical uncertainty and ‘Exp. Unc.’ is the systematic uncertainty from experimental part including the luminosity uncertainty. “Total” is a quadratic sum of statistical and experimental uncertainties.	121
A.4	Summary of the results for $d\sigma/dm$ measurement in combined channel. The “Total Unc” is a quadratic sum of statistical, experimental and theoretical uncertainties without luminosity uncertainty.	123

Chapter 1

Introduction

The field of high energy physics aims at the ³² understanding of the fundamental constituents of matter and the interactions to explain their behaviour. The knowledge of these constituents is important to describe the physical laws that shape our universe. In past centuries, the particle physicists have discovered different theories which led to the study of the most remarkable description of the fundamental particles along with their dynamics, known as the ¹⁹ Standard Model (SM) of particle physics. This theory has been well tested throughout ²¹ the years by many high energy experiments. The model accurately describes how everything observed in this universe is made from fundamental particles called ‘the fermions’ which are divided into quarks and leptons. These matter particles are governed by the carriers of four fundamental forces: gravitation, electromagnetism, strong and weak interactions, called ‘the vector bosons’.

Despite being the most well-described and successful theory, the SM is inconsistent with the existing experimental observations and points to ¹ the possibilities of new physics searches ‘Beyond the Standard Model’ (BSM). In order to validate a new theory, accurate theoretical calculations performed using a well-defined theory of interactions between quarks and mediating gluons, known as the Quantum Chromodynamics (QCD), have to be compared to precise experimental measurements

which lead to the discovery of the Large Hadron Collider (LHC) with a designed center-of-mass-energy of 14 TeV. In order to establish the non-SM outcomes at the new collider experiment, it is essential to validate the predictions of the SM in this new energy regime by studying already known and well understood theoretical SM processes. The Drell-Yan (DY) is one of the most important SM processes which occurs in high energy hadron-hadron collisions. It takes place when a quark and an antiquark annihilate to produce a pair of oppositely charged leptons by s -channel exchange of virtual photon or Z . The precise prediction of the DY production rate can be used as a confirmation of the SM at high energies.

The study of production of lepton pairs offers many interesting and important features of SM at the hadron colliders. Theoretical calculations of the differential cross section of DY process are well established and a comparison with experimental measurements allows for the tests of perturbative QCD. The measurement also provides useful constraints on the parton distribution functions (PDFs) of the protons which help in the tuning of parameters in various theoretical tools like “Fully Exclusive W and Z production” (FEWZ). The observed asymmetry of the charged leptons can be potentially used as an input to the PDF fits. Also, the forward-backward asymmetry (A_{FB}) which arises in DY lepton pairs due to vector and axial-vector couplings will eventually lead to a precise determination of weak mixing angle ($\sin^2 \theta_{eff}$), than the current result [1]. In addition, the DY lepton-pair production is a major source of background for the measurements like $t\bar{t}$ and various diboson physics analysis as well as for BSM searches which includes the production of high-mass dilepton resonances, Z' , providing the indications of extra dimensions. Hence, a precise knowledge of the DY differential cross section is crucial to establish the predictions of the SM and for the new physics searches.

The reasonably large production cross sections for leptonic final states at the LHC, can be used for the commissioning of physics tools as well as for the tuning of Monte-Carlo methods. The DY process in muonic and electronic final states, can

be used for the momentum and energy scale calibrations through the Z boson mass measurement ($M_Z = 91.2$ GeV). Hence, the DY cross section measurements at LHC can be an important source of information.

² The measurement of differential cross section $d\sigma/dm$ was first performed with ⁴ 7 TeV [2,3] data at the LHC, in the mass range $15 < m < 1500$ GeV providing a ⁸⁸ precise measurement in the low mass and Z -peak region. Another measurement was performed at 8 TeV [4], which extended the mass range to 2000 GeV. Additionally, ⁴ the double-differential cross section measurement $d^2\sigma/dmd|y|$ was performed in the ⁹ mass range $20 < m < 1500$ GeV and absolute dilepton rapidity from 0 to 2.4 at ²¹ 7 and 8 TeV center-of-mass energies. The differential cross section measurements at ¹ 7 and 8 TeV were performed in muon and electron final states, except $d^2\sigma/dmd|y|$ measurement at 7 TeV which was performed only in the muon final state. The mass range was further extended from 2000 GeV to 3000 GeV for the differential cross section measurement performed in the muon final state with 13 TeV [5] data.

² In this thesis work, the measurement of the DY differential cross section $d\sigma/dm$ ² is presented in the electron final state within the mass range $15 < m < 3000$ GeV, using ⁷ the data collected by the Compact Muon Solenoid (CMS) experiment at center-of-mass energy $\sqrt{s} = 13$ TeV during the year 2015, at the LHC. The differential cross section measurement in the bins of invariant mass allows to estimate the absolute value as well as the shape of the DY spectrum and a high electron energy resolution (up to TeV scale) results in a precise measurement.

The present work is organized into seven chapters, with a brief introduction ⁷ of each as follows:

Chapter 2 describes the fundamental principles of the SM, theories which govern the interactions between elementary particles and other theoretical concepts which are relevant for the understanding of the DY cross section measurement.

²⁵ **Chapter 3** gives an overview of the experimental apparatus ‘the LHC and its

various parameters' used for the collection of data. In this chapter, the CMS detector along with its various sub-detectors and their construction have been discussed in detail. It also covers the central data acquisition system which is used to store data to be further analysed by the physicists.

Chapter 4 presents the importance of simulation process categorized into event generation and detector simulation. This chapter also describes the reconstruction of physics objects via dedicated reconstruction algorithms, selection and identification of objects which are used in this analysis.

Chapter 5 describes the workflow of the analysis performed for the measurement of the DY differential cross section in the bins of dielectron invariant mass ⁷⁴ using the data collected by CMS during the year 2015. This chapter discusses the event selection, background estimation using data-driven techniques and various corrections which are used to correct the experimental data.

Chapter 6 focuses on the results obtained from the measurement of the DY cross section. The comparison of the measured differential cross section with various SM theoretical predictions has been discussed in this chapter. ¹⁰⁷

Chapter 7 provides a summary of the experimental results and the analysis work presented in this thesis.

Chapter 2

Theory

1 The high energy processes provide crucial information about theoretical and phenomenological concepts in particle physics. The Standard Model is the powerful theoretical framework which well describes the observed phenomena. The Drell-Yan process is one of the most important processes at the hadron colliders and an essential part in studies to understand the Standard Model. This chapter describes the theoretical concepts of the particle physics and the Drell-Yan process.

2.1 The Standard Model

The Standard Model (SM) of Particle Physics [6–8] describes the fundamental constituents of matter and their interactions in terms of elementary particles. The first class of elementary particles are spin- $\frac{1}{2}$ fermions, known as matter particles and the second class are spin-1 bosons, also called gauge bosons which are the carriers of the fundamental interactions. Figure 2.1 gives an overview of the elementary particles of the SM.

124 Elementary fermions are divided into three generations of quarks and leptons, each made up of a quark doublet and a charged lepton with an associated neutrino. The particles belonging to three generations have similar properties, except the

		Generations of Fermions (spin = $\frac{1}{2}$)			Force Carrier Bosons (spin = 1)		
		I	II	III	weak force weak charge	electro- magnetic force (QED) electric charge	strong color force (QCD) color charge 0e; massless
Quarks	charge	2.5 MeV 	1.29 GeV 	172.9 GeV 	0 e 91.2 GeV 	0e; massless 	
	-1/3 e	5.0 MeV 	100 MeV 	4.19 GeV 	$\pm 1 e$ 80.4 GeV 		
Leptons	-1 e	0.511 MeV 	106 MeV 	1.78 GeV 			
	0 e	< 2 eV 	< 0.2 MeV 	< 18 MeV 			
Higgs Boson (spin = 0) 							

Figure 2.1: The elementary particles of the Standard Model¹. The mass of each particle is presented [9].

mass of the particles which increases from lower to higher generation. The quarks and leptons are classified according to their mass, electrical charge and quantum numbers such as flavors and lepton number. There are six different kinds of quarks called flavors arranged as – up and down (u, d); charm and strange (c, s); top and bottom (t, b). These carry fractional electrical charge of $+\frac{2}{3}$ or $-\frac{1}{3}$ times the charge of electron and have an associated anti-particle called anti-quarks which carry same mass and spin, but an opposite charge. The quarks can combine in doublets and triplets to form composite particles namely ‘mesons’ ($q\bar{q}$) and ‘baryons’ (qqq or $\bar{q}\bar{q}\bar{q}$) [10] respectively, together known as ‘hadrons’. Quarks carry an additional charge known as color charge which comes in three forms – red, green and blue. The hadrons which are the combinations of quarks or anti-quarks are color neutral and hence, colored states are not observed. Similarly, the three generations of leptons consists of electronic leptons (e, ν_e); muonic leptons (μ, ν_μ); tauonic leptons (τ, ν_τ) with six corresponding anti-particles called anti-leptons. The electron is the only

¹J. Hauptman, Particle physics experiments at high energy colliders.

stable lepton with a mass of 0.511 MeV [9], while the heavier leptons, muons and taus, eventually decay to electrons and neutrinos.

Each fundamental force is transmitted through force-carrying bosons, as shown in Table 2.1. The strong nuclear force which is responsible for holding the nuclei together, with quarks inside, is mediated by exchange of gluon (g), the electromagnetic force which acts between charged particles and is responsible for binding the electrons with the nuclei to form atoms is mediated by neutral photon (γ), the weak nuclear force which is responsible for radioactivity is mediated by massive W^\pm and Z^0 bosons and the gravitational force which acts between all types of particles that have mass is mediated by a hypothetical graviton, and is not included in the SM. Quarks are the only fundamental particles, which interact via all the three forces, while leptons interact via only electromagnetic and weak interactions. The electromagnetic and weak interactions can be described as one single force, the electroweak interactions, by unified theory called ‘Electroweak Theory’ while the strong interactions are described by a theory called ‘Quantum Chromodynamics’ (QCD) [11, 12].

Force	Range (in m)	Strength	Mediators (mass in GeV)	Participants
Strong	10^{-15}	$\alpha_s \approx 1$	8 gluon (0)	quarks and gluons
Weak	10^{-18}	$\approx 10^{-5}$	W^\pm, Z (80.94, 91.2)	quarks and gluons
Electrom.	∞	$\alpha \approx \frac{1}{137}$	photon (0)	electrically charged particles
Gravity	∞	$\approx 10^{-39}$	graviton (0)	all particles

Table 2.1: The four fundamental forces in physics and their properties.

The SM is mathematically expressed using the local gauge theory which represents a unified description of the three forces based on symmetries. The Lagrangian corresponding to each fundamental interaction is invariant under the gauge symmetry group $SU(3)_C \times SU(2)_L \times U(1)_Y$ ². $SU(n)$ is the collection of all $n \times n$ unitary matrices with determinant 1 ($U^\dagger U = I$, where U^\dagger is the transpose conjugate). $U(1)$

² C , L and Y represent color charge, left-handedness and weak hyper-charge respectively.

describes the theory of electromagnetic interactions, known as ‘Quantum Electrodynamics’ (QED) [13]. $SU(2)_L \times U(1)_Y$ and $SU(3)$ describe the electroweak interactions and the QCD respectively. The gauge symmetry is broken by the Spontaneous Symmetry Breaking of the electroweak group to the electromagnetic subgroup:

$$SU(3)_C \times SU(2)_L \times U(1)_Y \rightarrow SU(3)_C \times U(1)_{QED} \quad (2.1)$$

The Higgs Mechanism [14–16] explains the existence of massive vector bosons (W^\pm and Z) and the essential constituent of the SM, the ‘Higgs Boson’ which provides mass to the fundamental particles. The ‘4 July 2012’ marked the discovery [17, 18] of a new boson particle, compatible with the properties of Higgs boson.

2.1.1 Electroweak Theory

The Quantum Electrodynamics is the quantum field theory which describes the electromagnetic interactions by the abelian gauge group $U(1)$. The local invariance under $U(1)$ leads to a massless vector boson (γ).

The theory of electroweak (EW) interactions is the unified description of the electromagnetic and weak interactions of the SM. Mathematically, the electroweak theory is described by the Yang-Mills³ model based on the non-abelian gauge group $SU(2)_L \times U(1)_Y$ which was proposed by S. Glashow, S. Weinberg and A. Salam [19, 20]. Y^4 operator is the generator of $U(1)_Y$ symmetry. The $SU(2)_L$ group of weak isospin has three generators $T^{1,2,3}$ which satisfy the commutation relation,

$$[T^a, T^b] = if^{abc}T^c \quad (2.2)$$

where, f_{abc} are the structure constants. The gauge field associated with the weak hyper-charge is denoted by B_μ and couples via Y , while the gauge fields of the

³Yang-Mills theory is a gauge theory based on the $SU(n)$ group.

⁴ $Y = 2(Q - T^3)$, where Q is the electric charge quantum number conserved in QED.

$SU(2)_L$ are $W_\mu^{1,2,3}$ and only couple to left-handed fermions.

The Lagrangian of the electroweak theory is therefore given by,

$$\mathcal{L} = \bar{\psi} i\gamma_\mu D^\mu - \frac{1}{4} B_{\mu\nu} B^{\mu\nu} - \frac{1}{2} \text{Tr}(W_{\mu\nu} W^{\mu\nu}) \quad (2.3)$$

$\bar{\psi}$ represents the Dirac field of spin $\frac{1}{2}$ particle. The first term describes the kinematics of the fermion field ψ , where D_μ , the gauge covariant derivative,

$$D_\mu = \partial_\mu - igW_\mu^a T^a + ig' B_\mu Y^5 \quad (2.4)$$

ensures local invariance under $SU(2)_L \times U(1)_Y$ symmetry transformation. The gauge fields W_μ^a , where a runs over three generators of the group and B_μ are massless vector fields and invariant under Lorentz transformation. Hence, any mass term of the gauge fields if added to the Lagrangian would violate the local $SU(2)_L \times U(1)_Y$ gauge invariance.

The second term in eq. 2.3 describes the kinematics of the vector field B_μ . The field tensor $B_{\mu\nu}$ is gauge invariant, defined as:

$$B_{\mu\nu} = \partial_\mu B_\nu - \partial_\nu B_\mu \quad (2.5)$$

The field tensors of the $SU(2)$ group are defined similarly, but contain an additional term due to the self-interaction of the gauge fields in the non-abelian group

$$W_{\mu\nu}^a = \partial_\mu W_\nu^a - \partial_\nu W_\mu^a + g f_{abc} W_\mu^b W_\nu^c \quad (2.6)$$

The gauge fields represent the mediator particles W^\pm , Z and γ of the weak and electromagnetic interaction respectively. Thus, the Lagrangian of the electroweak theory describes the dynamics of the fermions and the gauge bosons, as well as their

⁵ g and g' are respectively the gauge coupling constants of the $SU(2)$ and $U(1)$ groups.

interactions. To preserve the local gauge symmetry, fermions and gauge bosons are predicted to be massless. However, the experimental evidence shows that W^\pm and Z are massive. The mass generation mechanism is therefore, connected with the symmetry violation and requires extension in the theory.

In order to generate masses for the weak gauge bosons, the Higgs mechanism is used which employs the concept of spontaneous symmetry breaking and introduces a massive scalar boson field corresponding to the Higgs particle.

The Lagrangian of the external scalar field ϕ is given by,

$$\mathcal{L}_\phi = |D_\mu \phi|^2 - V(\phi) - \frac{1}{4} F_{\mu\nu} F^{\mu\nu} \quad (2.7)$$

where, $F_{\mu\nu} = \partial_\mu A_\nu - \partial_\nu A_\mu$ is the electromagnetic field tensor describing the kinematics of free gauge field A_μ . The self-interaction of the Higgs field is given by the scalar potential $V(\phi)$,

$$V(\phi) = \mu^2 \phi^\dagger \phi + \lambda (\phi^\dagger \phi)^2 \quad (2.8)$$

where, μ is a mass parameter and λ is a positive self-coupling constant. If $\mu^2 > 0$, then the potential has minima at the origin. However for $\mu^2 < 0$, we obtain a continuous set of minima at $\phi_1^2 + \phi_2^2 \equiv v^2$ and the symmetry can be broken with any particular choice of minima defined by non-vanishing vacuum expectation value,

$$|\phi_0|^2 = \frac{\phi_1^2 + \phi_2^2}{2} = -\frac{\mu^2}{2\lambda} \equiv v \quad (2.9)$$

The scale field is quantized by expansion around the minima resulting in one massive and three massless bosons, the later being known as Goldstone bosons [21]. Inserting the above expressions in eq. 2.7 results in the mass eigenstates which correspond to the measurable gauge bosons of the theory, given as a orthogonal

superposition of B_μ and W_μ^3 ,

$$W_\mu^\pm = \frac{1}{\sqrt{2}}(W_\mu^1 \mp iW_\mu^2), \quad Z_\mu = \frac{1}{\sqrt{g^2 + g'^2}}(g'W_\mu^3 - gB_\mu), \quad A_\mu = \frac{1}{\sqrt{g^2 + g'^2}}(g'W_\mu^3 + gB_\mu) \quad (2.10)$$

⁸³ The masses of the gauge bosons are therefore given by,

$$m_W = g \frac{v}{2}, \quad m_Z = \sqrt{g^2 + g'^2} \frac{v}{2} \quad \text{and} \quad m_A = 0 \quad (2.11)$$

The mixing between the two neutral components of the gauge fields W_μ^3 and B_μ can be represented as:

$$A_\mu = B_\mu \cos\theta_W + W_\mu^3 \sin\theta_W \quad (2.12)$$

$$Z_\mu = -B_\mu \sin\theta_W + W_\mu^3 \cos\theta_W \quad (2.13)$$

¹⁶⁸ where, θ_W is the Weinberg or weak mixing angle. Using above expressions it can be shown that the mass of W and Z are connected as,

$$\cos\theta_W = \frac{m_W}{m_Z} \quad (2.14)$$

⁴³ 2.1.2 Quantum Chromodynamics

The Quantum Chromodynamics (QCD) is the quantum field theory which describes the strong interactions based on the non-abelian gauge group $SU(3)$. The theory describes the interaction between six quark flavors ($f = u, d, s, c, b, t$) governed by eight gluons. The particles effected by the strong coupling require an additional color charge, which occurs in red, green and blue, to preserve the Pauli principle.

The QCD Lagrangian can be described in analogy to eq. 2.3 as,

$$\mathcal{L} = \sum_{i=1}^{N_c} \sum_{f=1}^{N_f} \bar{q}_{fi} (i\gamma^\mu D_\mu - m_f) q_{fi} - \frac{1}{4} F_{\mu\nu}^a F^{a\mu\nu} \quad (2.15)$$

⁶⁴ where, the sum runs over quark flavors N_f and all color states N_c . q_{fi} represents the quark fermion field. The last term in eq. 2.15 describes the dynamics of the gluon field A_μ , which contains triple and quartic gluon self-interaction terms $\sim A^3, A^4$ due to the non-abelian structure of $SU(3)$ group. This term is also known as Yang-Mills term,

$$\mathcal{L} = -\frac{1}{2} \text{Tr}(F_{\mu\nu} F^{\mu\nu}) = -\frac{1}{4} F_{\mu\nu}^a F^{a\mu\nu} \quad (2.16)$$

The field tensors in QCD, $F_{\mu\nu}^a$ can be described in analogy to eq. 2.6.

¹ The strength of the strong force is defined by a coupling constant α_s which has a characteristic property of showing different behaviour in low and high energy regimes. At high energies i.e. shorter distances, the force between quarks decreases and they behave as free particles. As a result α_s decreases due to self-interaction of the gluons, which causes an anti-screening of the colour charge of the quarks. This phenomena is known as ‘asymptotic freedom’. On the other hand at low energies, the coupling is large due to stronger force between the quarks which confines them inside hadrons. This effect is called ‘confinement’.

The strong coupling constant is not a constant and acquires the name ‘running coupling’ due to its dependence on the energy scale Q^2 , and can be written at leading order (LO) as [11],

$$\alpha_s(Q^2) = \frac{12\pi}{(33 - 2N_f) \ln \frac{Q^2}{\Lambda_{QCD}^2}} \quad \text{for } Q^2 \gg \Lambda_{QCD}^2 \quad (2.17)$$

where, Λ_{QCD} ¹ is an experimentally determined parameter obtained to be $\Lambda_{QCD} \sim$ 200 MeV. In the limit of asymptotic freedom $\alpha_s(Q^2 \rightarrow \infty) \rightarrow 0$,¹ the cross section can be expanded perturbatively [22, 23] in powers of α_s . In the limit of confinement $\alpha_s(Q^2 \rightarrow \Lambda_{QCD}^2) \rightarrow \infty$, the strong interaction becomes so large, at a separation distance of the diameter of a hadron ($\sim 10^{-15}$), that⁴² new quark-antiquark pairs are produced.¹ These quarks and antiquarks form mesons and baryons, and the bunches of hadrons are measured as jets inside a particle detector.

2.2 Proton-Proton Collisions

¹⁶⁷ To study the properties of elementary particles and to discover BSM physics, large particle accelerators are utilized. The Drell-Yan lepton pair production is an important process which is used to perform the tests of perturbative QCD (pQCD). Prior to LHC, the Drell-Yan production cross section was measured by the D0 and CDF experiments at the Tevatron and compared to pQCD calculations [24, 25]. The LHC experiments, however, allow a precision measurement of the theory with increased center-of-mass energy than the previous collider experiments at Tevatron.

The physics of proton-proton collisions is complex and involves various fundamental processes. The parton model [26] is used to describe the structure of protons and their interactions inside colliding hadrons which defines the hard interaction. The factorization theorem [22, 23] of QCD, which will be discussed later in detail, allows to calculate the hard scattering cross section in hadron collisions and involves the information from parton model as an input. A final state parton further emits partons, which themselves radiate, a process termed as parton showering. Eventually, hadronization occurs in which partons combine to form colorless hadrons, and a bunch of particles constituting hadrons is referred to as a jet [27, 28].⁴³

This section describes the structure of protons and various processes which occur in proton-proton collisions.¹

2.2.1 Structure of Protons

The proton is composed of elementary particles called partons; three valence quarks (*uud*) embedded in an infinite sea of quark anti-quark pairs (sea quarks) and gluons. The probability density of a parton i in the proton is defined as $f_i(x, Q^2)$ which depends on the probing energy scale Q^2 , and parton momentum fraction x with respect to the momentum of the proton. These functions are called parton distribution functions (PDF) and can be extracted from fits to experimental data using the Dokshitzer-Gribov-Lipatov-Altarelli-Parisi (DGLAP) evolution equations [29–31].

Figure 2.2 represents the DGLAP equation for a quark and expresses that the momentum fraction of a quark, x in $q(x, Q^2)$, could have come from a parent quark or gluon with momentum fraction, y in $q(y, Q^2)$ or $g(y, Q^2)$ [32] respectively. The splitting function $P_{qq}(x/y)$ represents the probability of a quark emitting a gluon and becoming a quark with momentum reduced by a fraction x/y . Similarly, $P_{qg}(x/y)$ represents the probability of a gluon decaying to $q\bar{q}$ pair. In the DGLAP equation, the PDF, in terms of the probing energy scale, $q(x, Q^2)$ is obtained by the sum over all possible momentum fractions y ($> x$) of the parent multiplied by the split functions and the strong coupling constant.

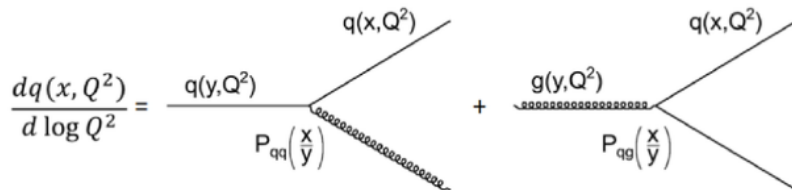


Figure 2.2: A symbolic representation of the DGLAP evolution equation for quark⁶.

The relevant PDF sets for LHC physics are CTEQ [33], MSTW [34], HERA-PDF [35] and NNPDF [36, 37]. Figure 2.3 shows the PDFs of the partons at two

⁶ISBN : 0471887412, 9780471887416.

different energy scales $Q^2 = 1.9 \text{ GeV}^2$ and $Q^2 = 10 \text{ GeV}^2$, calculated from fits to H1 and ZEUS data. It can be observed that, with increasing energy scale the PDFs become significantly larger at small x , which leads to probe more gluons and sea quarks in the proton.

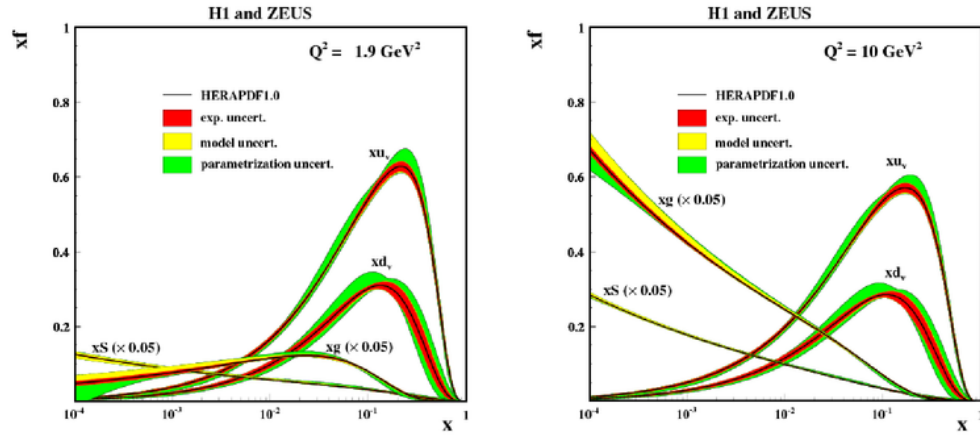


Figure 2.3: The parton distribution functions for quarks, anti-quarks and gluons for energy scale $Q^2 = 1.9 \text{ GeV}^2$ (left) and $Q^2 = 10 \text{ GeV}^2$ (right). The distributions are determined from the H1 and ZEUS Collaborations from global fits to data⁷.

2.2.2 Underlying Events and Pileup Contribution

The hadronic final states of hadron-hadron collisions are composed of an overlay of several contributions [38]. Thus, the final states can also be caused by contributions not associated to the hard scattering process. These effects are called Underlying Event (UE) which is a combination of soft parton radiation, other parton scatterings and additional scatters of the proton beam remnants which are the leftovers of hard collision. The UE activity increases with the center-of-mass energy.

Partons initiating the hard process can emit additional partons, the process is known as initial-state radiation (ISR). Similar radiation is possible for the final-state partons emerging from multiple soft scatters after the hard scattering has occurred

⁷Source : <https://arxiv.org/abs/0911.0884>

¹ called final-state radiation (FSR). In the case of Drell-Yan lepton pair production, the QCD effects enter only in the initial state which provides an opportunity to study parton shower effects due to ISR [39].

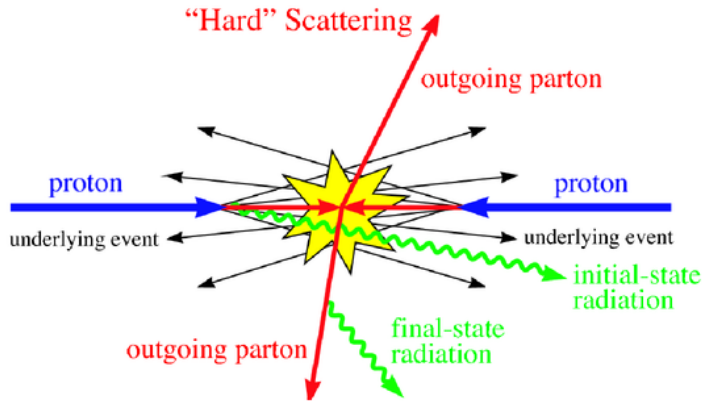


Figure 2.4: A schematic representation of $2 \rightarrow 2$ hard scattering event⁸.

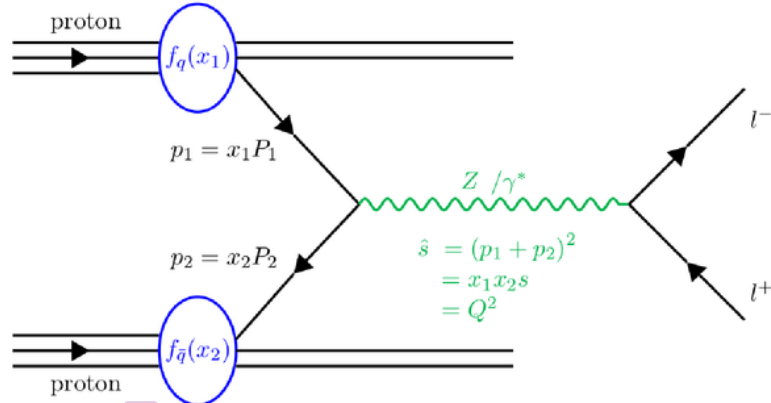
In addition to the hard $2 \rightarrow 2$ parton-parton scattering, multiple parton scatterings of softer partons can occur, ¹ called Multi Parton Interaction (MPI) [40], which do not interact with the hard process. This produces hadrons predominantly along the direction of the initial protons which have smaller transverse momentum, hence have a least effect on the physics observables. This phenomena is nonperturbative and leads to a substantial amount of soft particles which get added to the event content, requiring a proper modelling.

¹ Due to the fact that high density proton bunches are collided, the probability to have more than one proton-proton collision increases with increasing luminosity. The additional energy from proton-proton interactions other than the hard-scatter event is called pileup. While pileup itself cannot be directly measured, it can be correlated to various other directly measurable quantities for e.g., the number of primary vertices (N_{PV}) is directly correlated to the amount of pileup; the greater the N_{PV} , the more pileup energy is added to the event.

⁸Source : <https://arxiv.org/abs/hep-ph/0611148>

32 2.3 Drell-Yan Production

The production of a lepton pair l^+l^- with invariant mass $M^2 = (p_{l^+} + p_{l^-})^2 \gg 1 \text{ GeV}$
⁸ by the annihilation of a quark anti-quark pair is called Drell-Yan process. It was first
¹ presented in 1970 by Drell and Yan [41]. In hadron-hadron collisions, the quark and
¹ anti-quark are constituents of the two incoming hadrons and can create an off-mass-
¹ shell virtual boson (Z or γ^*) which directly decays into two leptons, immediately
¹ after its production. In the following section, the Drell-Yan production cross section
¹ is first calculated in the parton model and then including perturbative corrections,
¹ following the calculations in [11, 44].



33
 Figure 2.5: The Drell-Yan $q\bar{q} \rightarrow Z/\gamma^* \rightarrow l^+l^-$ production in a proton-proton collision [11]. $P_{1,2}$ are the four-momenta of the protons, $p_{1,2}$ are the four-momenta of the partons initiating the hard scattering, depending on the momentum fractions $x_{1,2}$.

2.3.1 Cross Section

1
 In a high energy proton-proton collision, the hard scattering process is initiated by
¹ two partons of the two protons. Figure 2.5 shows an illustration of the production of
¹ a Z/γ^* resonance. The square centre-of-mass energy of the proton-proton collision
¹ is defined as,

$$s = (P_1 + P_2)^2 \quad (2.18)$$

where, P_i is the four-momentum of proton i . In the collinear approximation, which means neglecting the transverse momentum of the partons, the four-momenta of the two partons can be written as [11],

$$p_1 = \frac{\sqrt{s}}{2} \overset{158}{(x_1, 0, 0, x_1)}, \quad (2.19)$$

$$p_2 = \frac{\sqrt{s}}{2} \overset{1}{(x_2, 0, 0, -x_2)} \quad (2.20)$$

with parton momentum fraction x_i of parton i . The square centre-of-mass energy of the parton scattering yields,

$$\hat{s} = (p_1 + p_2)^2 = x_1 x_2 s = M_{l^+ l^-}^2 = Q^2 \quad (2.21)$$

⁴⁷ The cross section of a QCD process can be calculated by using the collinear factorisation theorem [42]. This theorem separates the short-distance contributions which can be calculated perturbatively and include QCD radiations, and the long-distance contributions including hadronization, PDF and soft interactions, which cannot be calculated in pQCD and require phenomenological models [43] for precise determination. The ¹ cross section of a proton-proton collision can therefore be written as the convolution of hard cross section and PDFs of incoming parton.

¹⁶⁴ The Drell-Yan production cross section in proton-proton collisions is obtained ²⁹ by weighting the partonic cross section $\hat{\sigma}$ for the sub-process $q\bar{q} \rightarrow l^+ l^-$ with the PDFs $f_q(x_1)$ and $f_{\bar{q}}(x_2)$,

$$\sigma_{pp} = \sum_q \int dx_1 dx_2 f_q(x_1) f_{\bar{q}}(x_2) \hat{\sigma}_{q\bar{q} \rightarrow l^+ l^-} \quad (2.22)$$

where the sum runs over all quark anti-quark combinations and $\hat{\sigma}_{q\bar{q} \rightarrow l^+ l^-}$ is the sub-process cross section for $q\bar{q} \rightarrow l^+ l^-$.

At lowest-order in pQCD, the cross section of $q\bar{q} \rightarrow l^+l^-$ can be obtained as,

$$\hat{\sigma}_{q\bar{q} \rightarrow l^+l^-} = \frac{4\pi\alpha^2}{3\hat{s}} \frac{1}{N_c} Q_q^2 \quad (2.23)$$

where, $N_c (= 3)$ is the number of quark colors, $\alpha = \frac{e^2}{4\pi}$ is the electromagnetic coupling constant and Q_q is the electrical charge of the quark. The lepton pair can be produced with different invariant masses, corresponding to the production of a virtual photon or Z boson, $q\bar{q} \rightarrow Z/\gamma^* \rightarrow l^+l^-$, depending on the energy of the incoming quark anti-quark pair. Hence, the differential lepton pair invariant mass M distribution is considered,

$$\frac{d\hat{\sigma}}{dM^2} = \frac{4\pi\alpha^2}{3M^2} \frac{1}{N_c} Q_q^2 \delta(\hat{s} - M^2) \quad (2.24)$$

The differential cross section of the Drell-Yan process derived in the parton model gives,

$$\begin{aligned} \frac{d\sigma}{dM^2} &= \int_0^1 dx_1 dx_2 \sum_{q=1}^{N_f} \{f_q(x_1)f_{\bar{q}}(x_2) + f_{\bar{q}}(x_1)f_q(x_2)\} \frac{d\hat{\sigma}}{dM^2}(q\bar{q} \rightarrow l^+l^-), \\ &= \frac{4\pi\alpha^2}{3\hat{s}} \frac{1}{N_c} \int_0^1 dx_1 dx_2 \delta(x_1 x_2 s - M^2) \left[\sum_{q=1}^{N_f} \{f_q(x_1)f_{\bar{q}}(x_2) + f_{\bar{q}}(x_1)f_q(x_2)\} \right], \\ &= \frac{4\pi\alpha^2}{3\hat{s}} \frac{1}{N_c} \int_0^1 dx_1 dx_2 \delta(x_1 x_2 s - M^2) P_{q\bar{q}}(x_1, x_2) \end{aligned} \quad (2.25)$$

The sum runs over the N_f quark flavours and the term $f_{\bar{q}}(x_1)f_q(x_2)$ specifies the additional contribution from anti-quark quark pairs. The dependence on the PDFs is defined in the joint $q\bar{q}$ probability function $P_{q\bar{q}}(x_1, x_2)$ [44].

2.3.2 Perturbative QCD Corrections

In high energy hadron-hadron collisions, the Drell-Yan production cross section needs perturbative QCD corrections in order to account for the additional parton emissions. At the LO, only the quark anti-quark annihilation occurs $q\bar{q} \rightarrow Z \rightarrow l^+l^-$ which constitutes the dominant production of Z boson. However, at the NLO, due to the initial-state gluon radiation, (anti)quark-gluon scatterings are also considered.

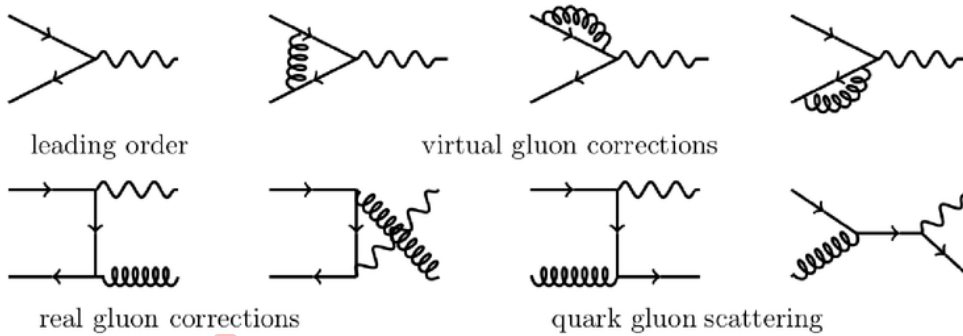


Figure 2.6: The LO and NLO Feynman diagrams for the Drell-Yan process. The solid lines represent quarks or anti-quarks, the spiral lines represent gluons and the wavy lines correspond to Z/γ^* .

The LO and NLO diagrams of the Drell-Yan process are shown in Fig. 2.6. In general, eq. 2.22 is expressed as a perturbative expansion in powers of the strong coupling, at the invariant lepton pair mass scale,

$$\sigma_{pp} = \sum_q \int dx_1 dx_2 f_q(x_1, M^2) f_{\bar{q}}(x_2, M^2) \times \left[\hat{\sigma}_{LO} + \frac{\alpha_s M^2}{2\pi} \hat{\sigma}_{NLO} + \left(\frac{\alpha_s M^2}{2\pi} \right)^2 \hat{\sigma}_{NNLO} + O(\alpha_s^3) \right]_{q\bar{q} \rightarrow l^+l^-} \quad (2.26)$$

The evaluation of higher-order QCD corrections gets complicated, when the momenta of the virtual particles in the loop are not constrained and the associated integrals become divergent, leading to infinite cross sections.

1 There are three types of divergences:

- 1 1. *Ultraviolet divergences* (UV) when the energy of the emitted parton tends to infinity.
2. *Infra-red divergences* (IR) due to soft-gluon emissions, when the energy of emitted gluon is low and tends to zero.
- 1 3. *Collinear divergences* which are induced by parton splittings of the initial-state partons, when the emitted gluon is very close to the parent quark.

The ultraviolet infinities are handled using the dimensional regularization procedure [45]. The technique defines the divergences in terms of a physical parameter, the dimensional renormalization scale μ_r , which gives a well-defined meaning to the perturbative expansion. This is the first step of renormalization and is known as regularization procedure. The reparameterization of the free parameter, α_s is performed such that the regularized divergences are absorbed in the definition of α_s , thus acquiring renormalization dependence. A measurable cross section, however, should be independent of μ_r , defined by the renormalization group equation (RGE),

$$\mu_r \frac{d\sigma}{d \ln \mu_r} = 0 \quad (2.27)$$

which can be obtained at some reference scale μ_0 . The reference value $\alpha_s(\mu)$ is determined by computing a cross section to certain order in pQCD and using the above equation to derive RGE for α_s in terms of a β -function. Hence, physical quantity, the cross section remains finite after renormalization to any order in the perturbative expansion.

1 However, the infrared collinear divergences are absorbed in the PDFs, when the partonic cross section is convoluted with parton densities, which redefines the PDFs as,

$$f_i(x, \mu_f) = f_i(x) c_i^{divergent}(x, \alpha_s, \mu_f) \quad (2.28)$$

1 The renormalised PDFs are the measurable quantities and depend on the factorisation scale μ_f . In order to verify these calculations, the divergent part of the cross section is included in the nonperturbative part which is done by the factorisation theorem.

Chapter 3

Experimental Details

3.1 The Large Hadron Collider

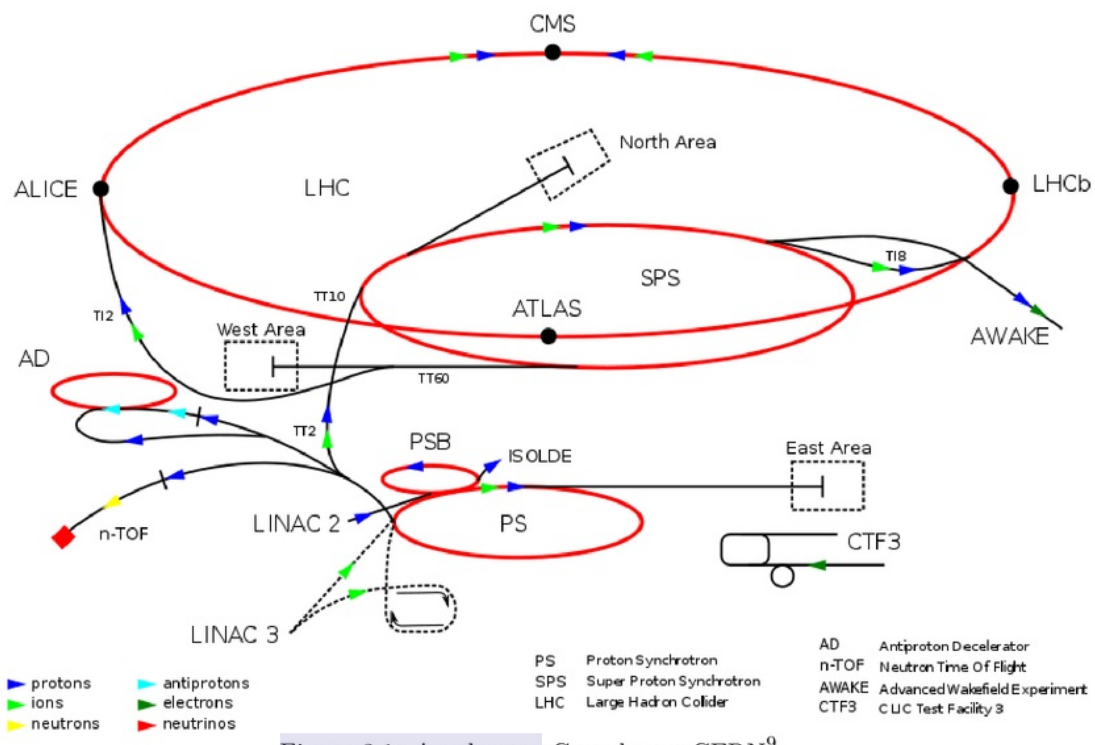
The Large Hadron Collider (LHC) [46] built by the European Organization for Nuclear Research (CERN), is the largest particle accelerator and collider. It is located at the Swiss-French border and installed in a tunnel of the former Large Electron Positron (LEP) collider having a circumference of 27 km. It has been designed to accelerate two proton beams up to an energy of 7 TeV per beam to produce proton-proton collisions at a center of mass energy of $\sqrt{s} = 14$ TeV as well as Pb ions upto an energy of 1.38 TeV per nucleon for studying Pb-Pb collisions and Pb-p collisions. The choice to have a proton-proton collider rather than electron-positron collider is mainly driven by the necessity to reach high energies without significant loss due to synchrotron radiation, which is inversely proportional to the fourth power of mass of the particles accelerated to relativistic speeds in a magnetic field.

3.1.1 LHC Design

The collider tunnel contains two adjacent parallel beamlines each containing a beam, travelling in the opposite direction. The particle collisions take place at the four intersecting points around the ring. However before reaching the collision point, the particles are accelerated by a series of accelerators that separately increase their energy. The LHC protons originate from a tank in which electrons are stripped from the hydrogen atoms and injected into LINAC2, the Linear Particle Accelerator. LINAC2 accelerates the protons to 50 MeV which are fed to the Proton Synchrotron Booster (PSB), further accelerating them to 1.4 GeV. In the next step, protons are injected into Proton Synchrotron (PS) and Super Proton Synchrotron (SPS) which accelerate the protons to 26 GeV and 450 GeV respectively.

The proton beams are finally introduced into the main ring, where they are accumulated and accelerated to their peak energy before the collisions take place. The schematic view of the accelerator chain is shown in Figure 3.1. The beams are guided by a strong magnetic field maintained by superconducting electromagnets throughout the accelerator ring. These includes a series of 1232 dipole magnets with magnetic fields up to 8.3 Tesla. The operating temperature of 1.9 K is maintained using 96 tonnes of superfluid helium, making LHC the largest cryogenic system in the world. In addition to the dipoles, there are about 392 quadrupole magnets which focus the proton beams while higher multipole orders are used to correct smaller imperfections in the field geometry. At full intensity, each beam will consist of 2808 bunches with $\sim 1.15 \times 10^{11}$ protons per bunch.

The layout of the LHC is composed of eight arcs and eight straight sections. Each straight section is equipped with an experimental apparatus. The two high luminosity experimental insertions are located at diametrically opposite straight sections: the ATLAS [47] experiment is located at Point 1 and the CMS [48] experiment at Point 5. These two general purpose experiments with complementary detector technologies share the interaction point (IP) with TOTEM [49] and LHCf [50], which

Figure 3.1: Accelerator Complex at CERN⁹.

¹⁸ are dedicated to cross section measurements and forward physics. The other two experiments ALICE [51] and LHC-b [52] are located at Point 2 and 8 respectively.

¹⁸ The heavy ion experiment ALICE is dedicated to the study of ¹⁶³ a fluid form of matter called quark-gluon plasma while the LHC-b collaboration performs precision measurements ¹⁸ on CP violation and rare decays in order to reveal possible indications for new physics.

3.1.2 Luminosity and Machine Parameters

The luminosity ¹ [53] in collider physics quantifies the performance and intensity of the collisions. The luminosity defines the possibility to produce a certain number ³⁸ of events of a process in a certain time interval. The ³⁸ number of events per second (N_{event}) generated in the LHC collision is given by:

$$N_{event} = \mathcal{L} \cdot \sigma_{event} \quad (3.1)$$

where σ_{event} is the cross-section for the event type under study and \mathcal{L} is the instantaneous luminosity which depends upon ⁵ the beam parameters and can be written for a Gaussian beam distribution as:

$$\mathcal{L} = \frac{N^2 n_b f_{rev} \gamma_r}{4\pi \epsilon_n \beta^*} F \quad (3.2)$$

where f_{rev} is the revolution frequency of the bunches, N is the number of protons per bunch, n_b is the number of colliding bunches, γ_r is the Lorentz factor, ϵ_n is the normalized transverse beam emittance, β^* is the beta function at the collision point and F is the geometric reduction factor arising from crossing angle. The luminosity is therefore, totally dependent on ¹ collider parameters and characterises the performance of the accelerator. The continuous increase of the luminosity delivered by

⁹Source : https://en.wikipedia.org/wiki/Large_Hadron_Collider

7

the LHC and recorded by the CMS during the year 2015 is shown in Fig. 3.2.

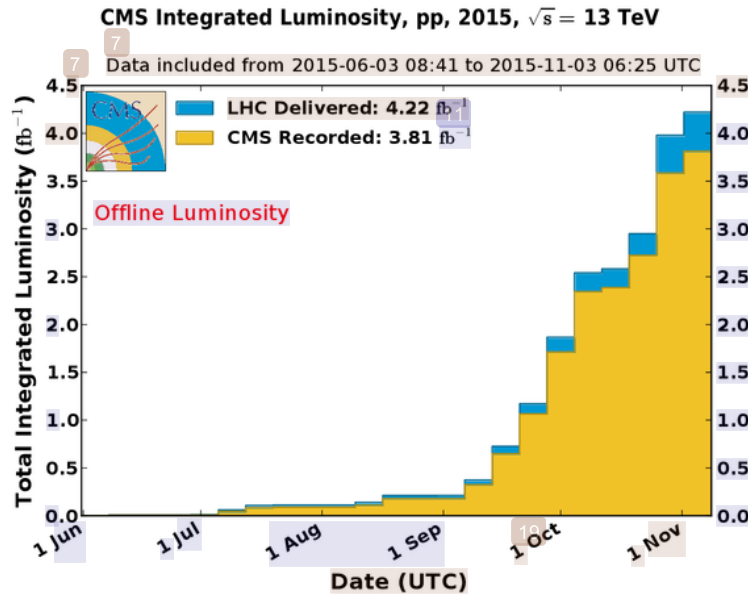


Figure 3.2: Total integrated luminosity in 2015¹⁰.

70

3.1.3 The Compact Muon Solenoid

CMS is a general purpose particle detector designed for the physics environment provided by the LHC. It is situated about 100 m underground near the French village Cessy. The generic detector has a composite structure consisting of several sub-detectors inserted into each other, starting from the IP. It consists of two main parts: a cylindrical part called the barrel and two circular parts called the endcaps which are located on both sides of the barrel along the beam axis to ensure a maximum detection coverage. Detector requirements for the CMS experiment to achieve these goals of LHC physics program can be summarized as:

- A highly efficient and high momentum resolution inner tracker to reconstruct and measure the charged-particle momentum. Efficient triggering and tagging

¹⁰Source : <https://twiki.cern.ch/twiki/bin/view/CMSPublic/LumiPublicResults>

⁵⁸ of τ leptons and b-quark jets, require pixel detectors close to the interaction region.

- Good electromagnetic energy resolution, di-photon and di-electron mass resolution ($\approx 1\%$ at 100 GeV), wide geometric coverage, ϕ_0 rejection and efficient photon and lepton isolation at high luminosities.
- Good missing transverse energy and dijet mass resolution, requiring hadron calorimeters with a large hermetic geometric coverage and with fine lateral segmentation.
- ³ Good muon identification and momentum resolution over a wide range of momenta and angles, di-muon mass resolution ($\approx 1\%$ at 100 GeV) and the ability to determine the charge of muons with momentum up to 1 TeV.

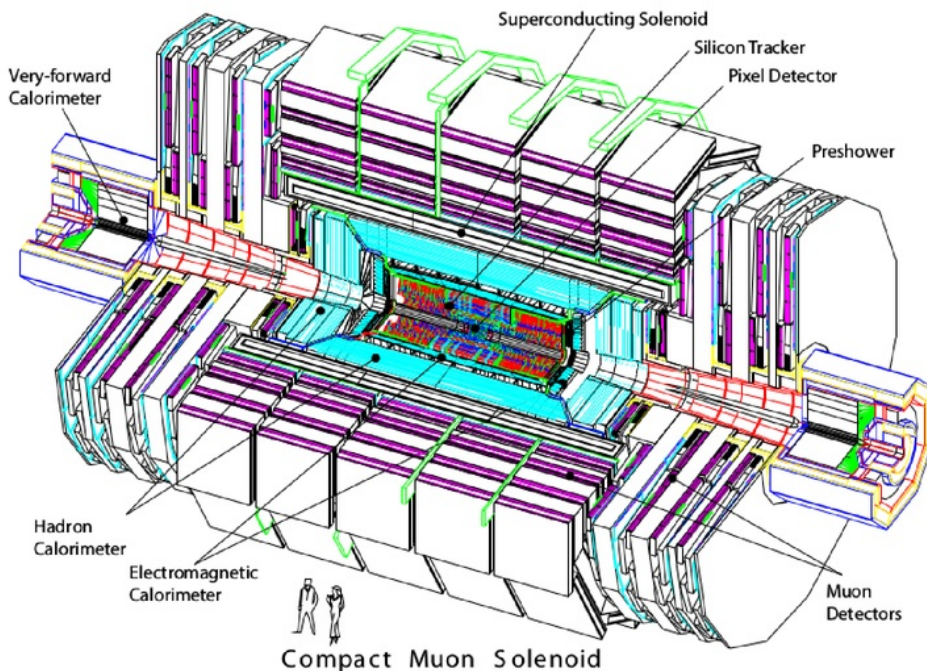


Figure 3.3: A schematic diagram of Compact Muon Solenoid¹¹.

⁵

¹¹Source : <https://cds.cern.ch/record/922757>

The design of the CMS detector is illustrated in Figure 3.3 and meets all the above requirements. At the core of the detector sits a large-bore superconducting solenoid with a 3.8 T magnetic field surrounding an all silicon pixel and strip inner tracker, a lead-tungstate scintillating crystal electromagnetic calorimeter and a brass-scintillator sampling hadron calorimeter. The iron yoke of the magnetic flux return is instrumented with four stations of muon detectors covering most of the 4π solid angle. Forward sampling calorimeters extend the pseudorapidity coverage from $|\eta| < 3$ to $|\eta| < 5$, assuring good hermeticity. The overall dimensions of the detector are a length of 21.6 m, a diameter of 14.6 m and a total weight of about 1.25×10^7 kg.

3.1.4 Coordinate Conventions

The adopted coordinate system has the origin located at the nominal collision point inside the detector. The x-axis points radially inward toward the center of the LHC, the y-axis points vertically upward and the z-axis points west along the counter-clockwise traveling beam direction (seen from above). The direction of the z-axis is referred to as longitudinal plane. The x-y plane, orthogonal to the beam line, is called transverse plane. Information about momentum and energy is often given by its transverse components p_T and E_T which are linked to the cartesian coordinates in the following way:

$$p_T = \sqrt{(p_x^2 + p_y^2)} \quad (3.3)$$

$$E_T = E \frac{p_T}{\sqrt{(p_T^2 + p_z^2)}} \quad (3.4)$$

A widely used coordinate variable is the rapidity y or pseudorapidity η . Rapidity has the property of being invariant under longitudinal boosts in the z-direction and

is defined as:

$$y = \frac{1}{2} \ln \frac{E + p_z}{E - p_z} \quad (3.5)$$

For high energy or massless particles, rapidity can be approximated by pseudorapidity η :

$$\eta = -\ln \left(\tan \frac{\theta}{2} \right) \quad (3.6)$$

which is correlated to the polar angle θ as shown in Fig. 3.4. The θ coordinate measures the angle with respect to the z-axis. $\eta = 0$ for the particles moving perpendicular to the z-axis and $\eta = \infty$ in $\pm z$ -direction. The ϕ coordinate measures the angle in the transverse plane, with respect to the x-axis and has the range $(-\pi, \pi)$. The angular distance between two particles is defined in the form of a Lorentz invariant ΔR variable:

$$\Delta R = \sqrt{\Delta\eta^2 + \Delta\phi^2} \quad (3.7)$$

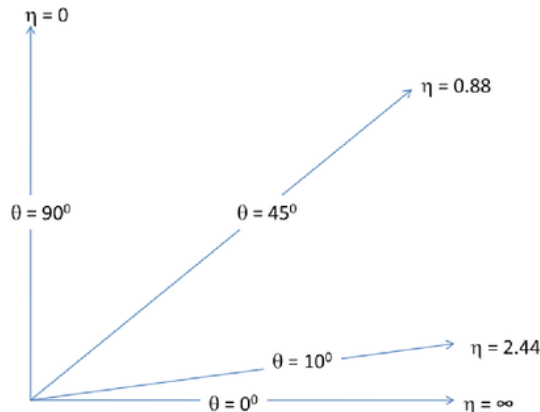


Figure 3.4: Relation between the polar angle and pseudorapidity¹².

¹²Source : <https://arxiv.org/abs/1604.02651>

3.1.5 Superconducting Magnet

The CMS detector requires a very strong magnetic field in order to induce enough bending of the charged particles so that the momentum of the charged particles can be measured up to the highest momentum particle expected at the LHC energy. The superconducting solenoid magnet [54] for CMS has been designed to reach a 4 T field in a cylindrical region of 6 m diameter and 12.5 m length with a stored energy of 2.6 GJ at full current. The flux is returned through a 10^7 kg yoke consisting of five wheels and two endcaps, composed of three disks. The superconducting high-purity aluminium-stabilized niobium-titanium (NbTi) coil is cooled to a temperature of 4 K using a complex liquid helium cooling system. The magnet coil is large enough to accommodate the inner tracker and the calorimetry inside which limits the energy loss interactions and thus improve the energy resolution of the calorimeter.

3.1.6 Inner Tracking System

The inner tracking system is designed to provide a precise and efficient measurement of the trajectories of charged particles emerging from the pp collisions, as well as a precise reconstruction of secondary vertices. It surrounds the interaction point and has a length (diameter) of 5.8 m (2.5 m). The solenoid provides a homogeneous field of 3.8 T over the full volume of the tracker. The main design challenge of the tracking system was to develop detector components able to operate in a harsh environment for an expected lifetime of 10 years which lead to a tracker design based entirely on silicon detectors. Figure 3.5 shows a schematic of the CMS tracking system [55, 56] consisting of a pixel detector and silicon strip tracker, covering a pseudorapidity range of $|\eta| < 2.5$.

Pixel Detector : The pixel detector contributes to precise tracking points in r , ϕ and z and hence responsible for a small impact parameter resolution. It consists of 53 cm long, three cylindrical layers of hybrid pixel detector modules placed at

radii of 4.4 cm, 7.3 cm and 10.2 cm from the interaction point in the barrel region.

These are complemented by two endcap disks on each side of the detector placed at $|z| = 34.5$ and 46.5 cm, extending from 6 to 15 cm in radius. The modules on the pixel disks are tilted by approximately 20° , resulting in a turbine-like geometry. The modules are made of 66 million square pixels, each with dimension of $100 \times 150 \mu\text{m}^2$, with an active area of around 1 m^2 , thus providing this subsystem a high granularity.

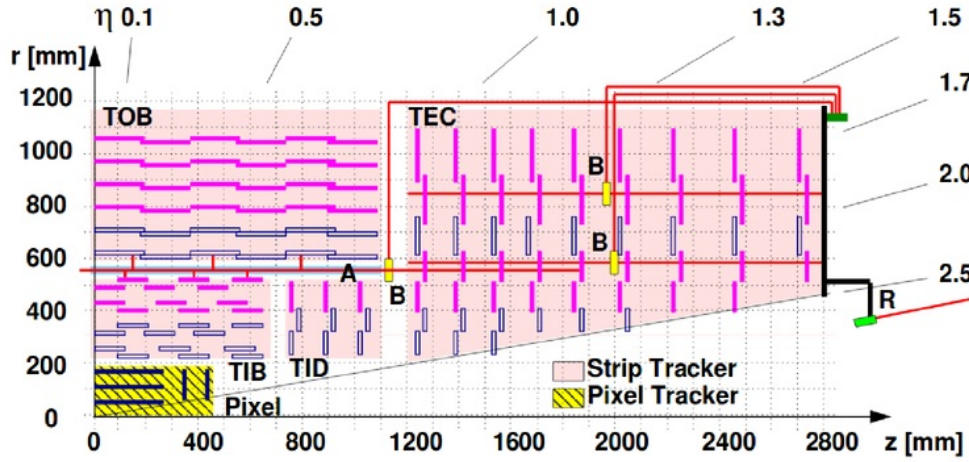


Figure 3.5: CMS tracking system¹³.

Silicon Strip Tracker : The silicon strip system is divided into four parts. The central region is covered by the Tracker Inner Barrel (TIB) and the Tracker Outer Barrel (TOB). The TIB is composed of four cylindrical layers of modules covering the region $25 \text{ cm} < r < 50 \text{ cm}$, while the TOB covers the region $50 \text{ cm} < r < 116 \text{ cm}$ and $|z| < 118 \text{ cm}$, with six cylindrical regions. The forward region is covered by the Tracker Inner Disks (TID), three disks on each side of TIB. The TIB/TID delivers up to 4 r - ϕ measurements for trajectory reconstruction. The TOB provides another set of 6 r - ϕ measurements. The Tracker Endcap (TEC) is composed of 9 circular wheels covering the region $130 \text{ cm} < |z| < 270 \text{ cm}$ and provides up to 9 ϕ

¹³Source : <https://arxiv.org/abs/0910.2505>

measurements for trajectory reconstruction.

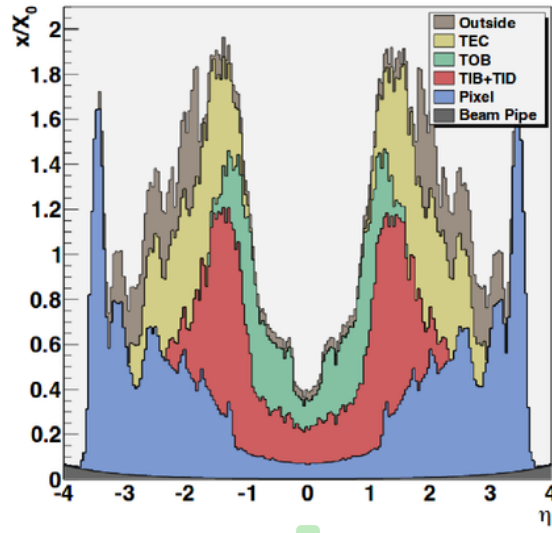


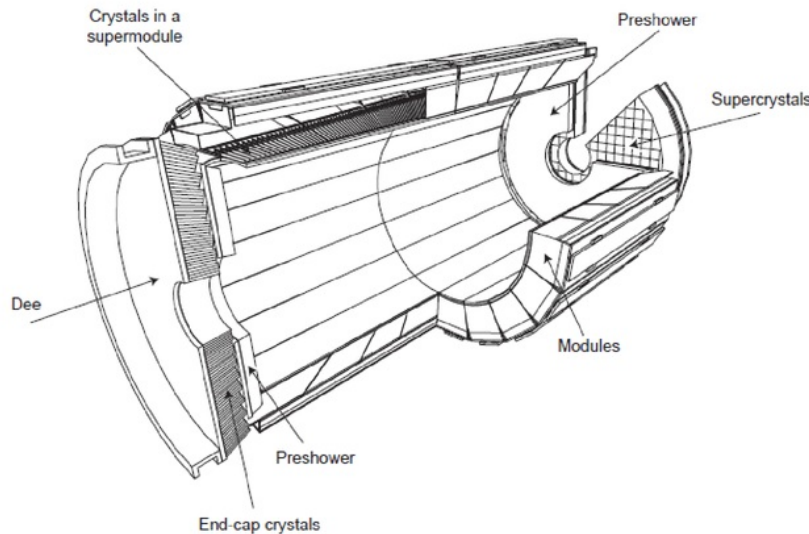
Figure 3.6: Tracker material thickness as a function of η , expressed in relative radiation length x/X_0 of the different components of the tracker¹⁴.

Particles crossing the tracker can interact with the material, especially electrons which can radiate photons through Bremsstrahlung process and thus lose significant part of their energy before having it measured in the electromagnetic calorimeter. Hence, it is important to have an estimate of the amount of tracker material. Figure 3.6 shows the thickness (x) of the CMS tracker expressed in units of radiation length as a function of pseudorapidity η . It increases from approximately 0.4 x/X_0 at $|\eta| \approx 0$ to about $1.8 x/X_0$ at $|\eta| \approx 1.4$, beyond which it falls to about 1 x/X_0 at $|\eta| \approx 2.5$. The tracking system provides a transverse momentum resolution of about 1-2% for high momentum (100 GeV) tracks upto $|\eta| \approx 1.6$ and becomes worse in the high η region.

¹⁴Source : <http://stacks.iop.org/1748-0221/4/i=05/a=P05003>

3.1.7 ⁷ Electromagnetic Calorimeter

The principle of the CMS electromagnetic calorimeter (ECAL) [57, 58] relies on the development of electromagnetic shower initiated by an electron or a photon interaction with a scintillating crystal via Bremsstrahlung process or pair production. Two quantities are used to quantify the development of an electromagnetic shower: the radiation length X_0 , which quantifies the longitudinal development, is the distance after which the electron has lost a fraction of its energy equal to $1/e$ and the Moliere radius which quantifies the lateral development.



³⁸ Figure 3.7: Layout of the CMS Electromagnetic Calorimeter showing the arrangement of crystal modules, supermodules and endcaps with the preshower detector in front of it¹⁵.

The choice of the design of electromagnetic calorimeter lead to a compact and homogeneous lead tungstate ($PbWO_4$) [59, 60] scintillating crystal calorimeter. The layout of ECAL is shown in Figure 3.7. The longitudinal view of ECAL is shown in Figure 3.8. This material has a very high density (8.3 gcm^{-3}), a small Moliere radius (21 mm) and radiation length ($X_0 = 0.89 \text{ cm}$), allowing for a compact detector design. It is reasonably resistant to high radiation and has a fast readout

¹⁵Source : <http://arxiv.org/abs/arXiv:1308.6064>

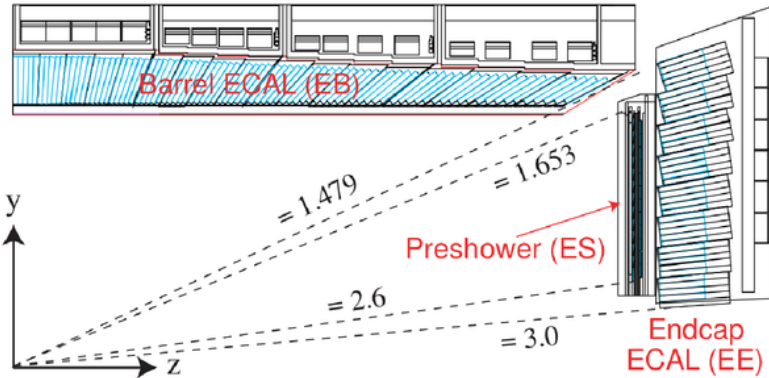


Figure 3.8: Longitudinal view of CMS Electromagnetic Calorimeter¹⁶.

response with 80% of the light getting emitted in one bunch crossing i.e 25 ns. The electromagnetic calorimeter consists of 61200 lead tungstate crystals in the central region ($|\eta| < 1.479$) and 7324 crystals in each of the two endcaps ($1.479 < |\eta| < 3$).

Barrel Electromagnetic Calorimeter

The barrel section (EB) has an inner radius of 129 cm. It is structured as 36 identical "supermodules", each covering half the barrel length. The crystals have trapezoidal shape with front and rear face dimensions of $22 \times 22 \text{ mm}^2$ and $26 \times 26 \text{ mm}^2$ respectively, equivalent to $\Delta\eta \times \Delta\phi = 0.0175 \times 0.0175$ and corresponding approximately to one Moliere radius. The crystals length is equal to 230 mm, corresponding to $25.8 X_0$. Scintillation light provided by the crystals is directed to the avalanche photodiodes (APD) [61] which convert light into analog signal, pre-amplify it and send it to outer electronics for further processing and trigger decision.

Endcap Electromagnetic Calorimeter

The endcaps (EE) are placed at a distance of 314 cm from the vertex. The endcap consists of identically shaped crystals grouped in mechanical units of 5 x 5 crystals (supercrystals). Each endcap is formed from two structures with a "D" shape called Dees. The crystal front and rear face dimensions are $28.6 \times 28.6 \text{ mm}^2$ and $30 \times$

¹⁶Source : <http://arxiv.org/abs/arXiv:1308.6064>

30 mm² respectively, slightly different compared to the barrel part and the length reduced to 220 mm, corresponding to 24.7 X₀. Due to the higher expected hadron fluency in the forward region, more radiation resistant device, the vacuum phototriode (VPT) [61] is used for light to analog signal conversion and preamplification.

In addition, a silicon/lead pre-shower detector (ES) is installed in front of the crystal calorimeter in the endcaps (1.65 < |η| < 2.6), in order to improve the γ/π₀ discrimination and vertex reconstruction of photons. The energy resolution of a calorimeter can be parametrised as:

$$\left(\frac{\sigma}{E}\right)^2 = \left(\frac{S}{\sqrt{E}}\right)^2 + \left(\frac{N}{E}\right)^2 + C^2 \quad (3.8)$$

where S is the stochastic term which represents the statistical error from electromagnetic shower evolution, N the noise term is the error in energy measurement due to noise from the electronics and pileup and C the constant term is related to the calibration of the calorimeter. The ECAL energy resolution in test beams using electrons of 20 to 250 GeV has been measured to be:

$$\left(\frac{\sigma}{E}\right)^2 = \left(\frac{2.8\%}{\sqrt{E}}\right)^2 + \left(\frac{12\%}{E}\right)^2 + (0.3\%)^2 \quad (3.9)$$

The contributions change at different pseudorapidities and with the luminosity of the machine. The constant term C is dominant at high energies and includes different contributions, like, the stability of the operating conditions (voltage and temperature), transparency loss of crystals and the inter-calibration errors.

3.1.8 Hadron Calorimeter

The hadron calorimeter (HCAL) [62] is a sampling calorimeter formed of layers of plastic scintillating tiles with embedded optical fibers interleaved with brass layers.

⁴⁵ The brass has been chosen as an absorber material for its high density 8.96 g.dm^{-3} .
⁴⁰ The hadronic calorimeter plays an essential role in the identification of quarks and gluons by measuring the energy and direction of jets. ¹⁰ Additionally, it provides an indirect measurement of non-interacting, uncharged particles such as neutrinos by ⁸ conservation of the momentum in transverse plane i.e. missing transverse energy (MET), which is important in the search of supersymmetric particles. An important requirement of the HCAL is to minimize the non-Gaussian tails in the energy resolution and to provide good containment of hadronic shower and hermeticity for the measurement of MET. Hence, the HCAL design maximizes the material inside the magnet coil in terms of interaction lengths.

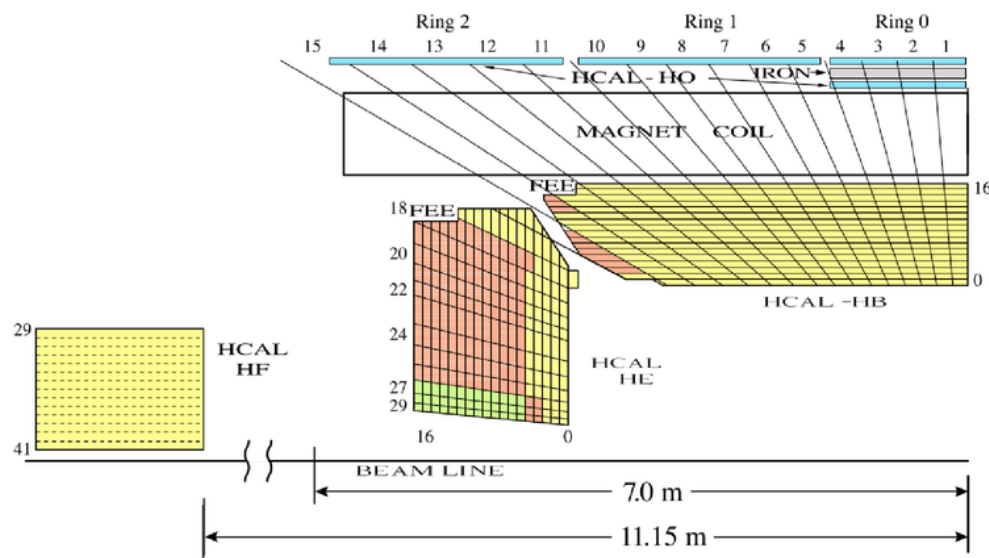


Figure 3.9: CMS Hadron calorimeter¹⁷.

¹⁴⁸ A schematic view of HCAL is shown in Figure 3.9. The HCAL layout is characterized by a cylindrical part called the barrel and two circular structures, the endcaps, located on each side of the barrel and joined hermetically to it. In addition, the hadron outer (HO), placed after the solenoid, complements the barrel calorimeter in the central region and the hadron forward (HF) extends the accep-

¹⁷Source : <https://cds.cern.ch/record/1481837>

¹¹⁰ tance coverage in the forward region up to $|\eta| = 5.2$.

Hadron Barrel

¹ The hadron barrel (HB) consists of 32 towers covering the pseudorapidity region $|\eta| = 1.3$, with a segmentation of $\Delta\eta \times \Delta\phi = 0.087 \times 0.087$. It is made of two halves on the positive and negative side of the z-axis, each half dividing into 18 identical wedges covering a ϕ region of 20^0 . A total of 17 plastic scintillators as active material interleaved with stainless steel and brass absorber plates, each with a thickness of 5 cm, constitute the HCAL barrel. The total absorber thickness at 90^0 is ²⁷ 5.82 interaction lengths (λ_I). The effective thickness of barrel increases with polar angle as $1/\sin\theta$, resulting in $10.6 \lambda_I$ at $|\eta| = 1.3$. All layers in one $\eta \times \phi$ cell are connected by wavelength shifting fibers (WLS) and read out as single channel, resulting in 2304 truncated pyramid shaped HCAL towers.

Hadron Endcap

Two circular structures (HE) complement the barrel in the forward pseudorapidity region (¹³⁷ $1.3 < |\eta| < 3.0$). The granularity of the crystals is $\Delta\eta \times \Delta\phi = 0.087 \times 0.087$ for $|\eta| \in (1.3, 1.6)$ and $\Delta\eta \times \Delta\phi = 0.17 \times 0.17$ for $|\eta| \in (1.6, 3)$. The brass plates are 79 mm thick with 9 mm gaps to house the plastic scintillators. The total length of the calorimeter is about $\lambda_I = 10$. The light is collected by WLS fibers and routed to hybrid photodiodes (HPDs).

Hadron Outer

³ To ensure adequate sampling depth for $|\eta| < 1.3$, the hadron calorimeter is extended outside the solenoid with a tail catcher called the outer calorimeter (HO). The HO utilizes the solenoid coil as an additional absorber equal to $1.4/\sin\theta$ interaction lengths. It is used to identify the late starting showers and measure the shower energy deposited after HB. The detector is situated as the first sensitive layer of each of the five rings (along the z-axis) composing the iron yoke that returns the magnetic field of the solenoid. Figure 3.10 shows the position of HO layers in the

rings of the magnetic field return.

It is divided into 5 sections along η , called rings. The central ring (ring 0) has two layers of HO scintillators on either side of a 19.5 cm thick piece of iron at a radial distance of 3.82 m and 4.07 m, respectively. The other four rings (rings ± 1 and ± 2) have a single layer of HO at a radial distance of 4.07 m. One of the major contributions has been by the Panjab University HEP group along with Tata Institute of fundamental research (TIFR), Mumbai in the fabrication of scintillation counters for HO.

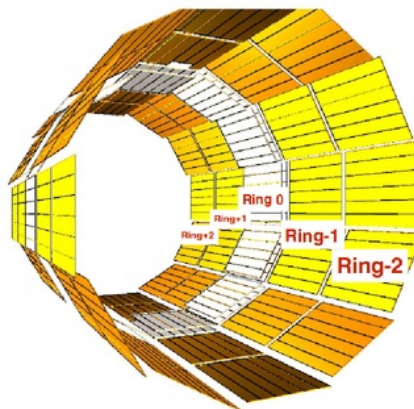


Figure 3.10: The layers of Hadrom Outer.¹⁸

Hadron Forward

The region between $3.0 < |\eta| < 5.0$ is covered with the help of Hadron Forward (HF) calorimeter. The two HF calorimeters (HF+ and HF-) are composed of quartz fibers encased in cylindrical steel matrices with outer radii of 130 cm. The signal is generated when charged shower particles propagate through the quartz fibers above the threshold and generate Cherenkov light. The light is converted to currents by photomultiplier tubes. There are 13 towers in η , with a size $\Delta\eta \approx 0.175$, except for the lowest η tower ($\Delta\eta \approx 0.1$) and the highest η tower ($\Delta\eta \approx 0.3$). The ϕ

¹⁸Source : <http://iopscience.iop.org/1742-6596/587/1/012005>

52

segmentation of all the towers is 10^0 , except for the highest η which has $\Delta\phi = 20^0$. This leads to 900 towers and 1800 channels in the 2 HF modules. The HF calorimeter improves the measurement of the MET and enables very forward jets to be identified and reconstructed. The energy resolutions for different parts of HCAL are given by:

$$\left(\frac{\sigma_E}{E}\right)^2 = \left(\frac{84.7\%\sqrt{\text{GeV}}}{\sqrt{E}}\right)^2 + (7.4\%)^2 \quad \text{for HB, HE and HO}, \quad (3.10)$$

$$\left(\frac{\sigma_E}{E}\right)^2 = \left(\frac{198\%\sqrt{\text{GeV}}}{\sqrt{E}}\right)^2 + (9.0\%)^2 \quad \text{for HF} \quad (3.11)$$

3.1.9 Muon System

Muon detection is a powerful tool for recognizing signatures of interesting processes over the very high background rate present at the LHC. The muons are less affected by radiative losses in the tracker material, hence emphasizing the discovery potential of muon final states and the necessity for muon detection with wide angular coverage.

The muon spectrometer [63] is placed outside the solenoid magnet and is embedded in the iron return yoke. It covers the pseudorapidity region $|\eta| < 2.4$ and performs three main functions: muon identification, measurement of momentum and charge, and triggering. Good muon momentum resolution and trigger capability are enabled by the high field solenoidal magnet and its flux-return yoke. The muon system is designed to reconstruct the momentum and charge of muons over the entire kinematic range of the LHC. A sketch of the muon system is shown in Figure 3.11. Three types of gaseous particle detectors are used for muon identification and measurement. In the barrel region ($|\eta| < 1.2$), the muon rate as well as the residual magnetic field in the chambers is low, drift tube (DT) chambers are used. In the 2 endcaps, where the muon rate and the magnetic field is high, cathode strip

chambers (CSC) are used to cover the region up to $|\eta| < 2.4$. In addition, resistive plate chambers (RPC) are used in both the barrel and endcap regions. ⁹ RPCs provide a fast response with good time resolution but with a coarser position resolution than the DTs/CSCs.

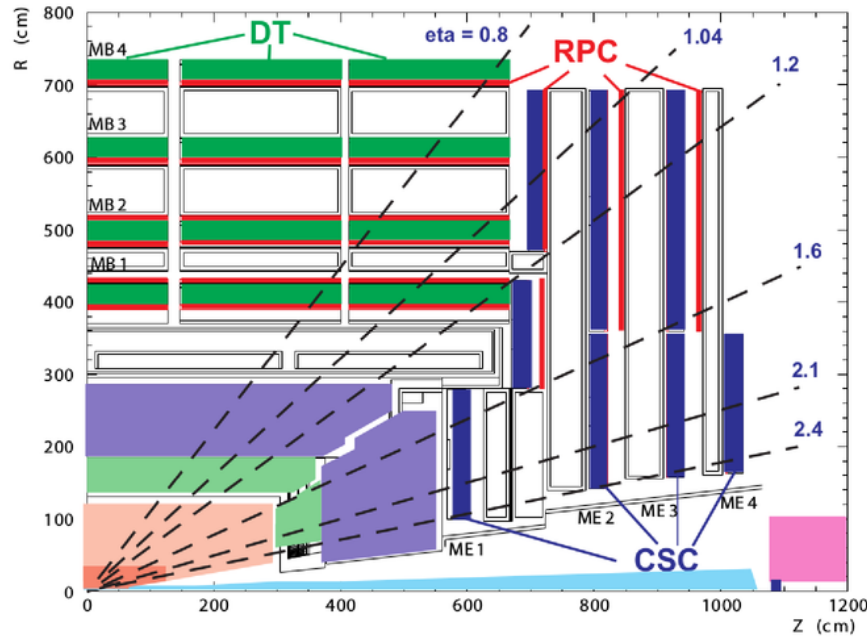


Figure 3.11: CMS Muon Chambers¹⁹.

Drift Tube Chambers

¹¹ In the Muon Barrel region, 4 stations of detectors are arranged in cylinders interleaved with the iron yoke. The segmentation along the beam direction follows the 5 wheels of the yoke (YB+2 to YB-2 along $\pm z$). Each chamber is made up of twelve layers of DTs, grouped in three independent subunits called superlayers (SL). The ³ SL is the smallest independent unit of the design. The anode wires in the two outer SLs are parallel to the beam line provide a track measurement in the magnetic-bending $r - \phi$ plane. In the inner SL, the wires are orthogonal to the beam line and measure the longitudinal coordinate z . ³ This third z -measuring SL is not present in

¹⁹Source : <https://arxiv.org/abs/1209.2646>

³ the fourth station, which therefore measures only the ϕ coordinate. The ⁷ internal volume is filled with a non-flammable gas mixture of Ar (85%) and CO₂ (15%) at atmospheric pressure.

Cathode Strip Chambers

The Muon Endcap (ME) system consists of 234 CSCs ⁷⁴ on each side of the CMS detector. The CSCs have multiwire proportional chambers ⁷ with one cathode plane segmented in strips running orthogonal to the wires. With a short drift path, the CSC chambers have a fast response time, reducing the sensitivity to the nonuniform magnetic field and provide a precision muon measurement. CSC chambers ¹⁶ are arranged in four discs (stations) placed between the iron discs of the yoke. Each chamber is formed by six trapezoidal layers, ⁷ with strips in the radial direction for a precise measurement of the azimuthal coordinate ϕ . The spatial resolution provided by each chamber is approximately 200 μm in r and z and approximately 10 mrad in ¹⁹ ϕ . A muon in the pseudorapidity range $|\eta| \in (1.2, 2.4)$ crosses at least three ³ CSCs. In the endcap-barrel overlap range of $|\eta| \in (0.9, 1.2)$, muons are detected by both ⁵⁶ the barrel DTs and CSCs.

Resistive Plate Chambers

⁸ Resistive plate chambers are installed both in the barrel and the endcap regions. The RPCs can be operated at high particle rates up to 10 kHz/cm² with a good time resolution and a response much faster than 25 ns. Hence, they enable unambiguous assignment of signals to the correct bunch crossing even in the presence of ³ high background present at the LHC. Signals from these devices also provide the ¹⁶ position of a muon hit with the required accuracy for triggering. They cover the pseudorapidity range $|\eta| < 1.6$ and are double-gap chambers filled with a C₂H₂F₄ and C₄H₁₀ gas mixture, operating ⁹ in avalanche mode. Their excellent time resolution is countered by their coarse position resolution, poorer ¹ than the DTs or CSCs. The RPCs are grouped in stations like the DTs and CSCs, with four stations in the barrel and three in the endcap. The innermost barrel stations have two RPC layers

along the outside of the DT chambers, with each layer divided into 2 or 3 partitions in η . The RPC endcaps stations are divided into three rings with increasing radial distance from the beam line, with 36 chambers in each ring covering the full azimuthal range.

⁸ 3.1.10 Trigger System

The LHC bunch-crossing rate of 40 MHz and the CMS event size of approximately 1 MB lead to a massive amount of delivered data which is too large to be stored and analyzed. In order to process this data, there is a need of reduction in the rate to make it equivalent to the offline storage limit, O(100Hz). Hence, one of the most important and difficult aspects of this experiment is the designing and implementing ¹⁵⁷ a Trigger and Data Acquisition (DAQ) system [64] to transfer the data to storage for further processing.

The CMS trigger system performs a fast online selection of potentially interesting events, lowering the rate of recorded events eventually to approximately 300 Hz. This reduction by a factor of more than 10^5 does not limit the discovery potential ¹²⁷ of CMS since the cross sections for processes of interest, such as the cross-section measurements of W/Z boson, t-quark or other diboson processes and Higgs Physics, SUSY production or other exotic Beyond Standard Model (BSM) studies, are even ²² smaller compared to the total proton-proton cross section. The design of CMS trigger and data acquisition system is illustrated in Figure 3.12. The selection of events ¹⁴⁷ is based on their physics content, such that the online algorithms have a level of sophistication comparable to that of the offline reconstruction keeping the efficiency ¹¹ for physics objects high. The CMS trigger has two levels: The Level-1 Trigger (L1) and the High Level Trigger (HLT).

3.1.10.1 Level 1 Trigger

The Level-1 trigger consists of custom designed, largely programmable hardware electronics. It uses coarsely segmented data from the calorimeters and the muon system, while holding the high-resolution data in pipelined memories in the front-end electronics with a design output rate limit of 100 kHz. The allowed latency between a given bunch crossing and the distribution of the trigger decision to the detector is $3.2 \mu\text{s}$. Events are selected based on the presence of physics objects such as electrons, photons, muons or jets above a p_T threshold as well as characteristics such as the amount of experimental MET. The L1 electronics are housed partly on the detectors and partly in the underground control room located at a distance of approximately 90 m from the experimental cavern.

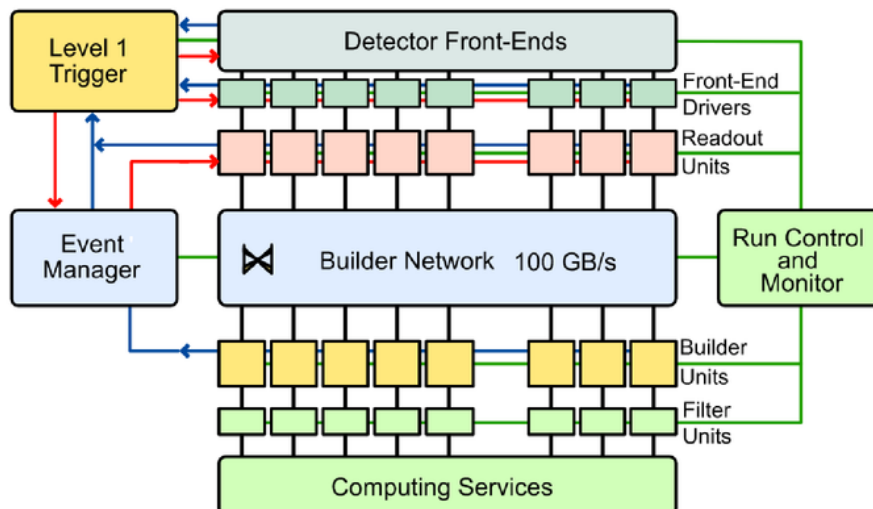


Figure 3.12: CMS Trigger and Data Acquisition System²⁰.

3.1.10.2 High Level Trigger

The HLT is a software system implemented in a filter farm of about 1000 commercial processors with a latency of approximately 30 ms. It has an access to the complete

²⁰Source : <http://inspirehep.net/record/1186236/files/diss.pdf>

³ read-out data and can therefore perform complex calculations similar to those made in offline analyses. The HLT works on the principle of regional reconstruction in order to avoid the complete event reconstruction and fast event rejection by rejecting the uninteresting events as fast as possible. If an event is accepted by the L1 trigger, the data is transferred further to the HLT which applies a predefined set of requirements, reducing the rate of events to 100 Hz. Upon acceptance, the data from the event is transferred for storage and further processing by the physicists. Since the HLT is software-based, reconstruction algorithms and selection requirements can be quickly adjusted during operation. The HLT algorithms depend strongly on the expected instantaneous luminosity and need a prescale factor in order to reduce the output rate for high luminosity runs.

3.1.10.3 Electron Trigger

The dedicated triggers are designed to select the events which have electrons in the final state. At the L1 level, the local trigger uses information from the energy ⁷ deposits in the ECAL and HCAL calorimeters. This information is transferred to the regional trigger which combines the information from each sub-detector's local trigger and passes the information further to global trigger. At this level, a decision is taken to accept or reject the event based on a set of algorithms for a physics object. These algorithms, known as 'Trigger Menu', gather a detailed information which includes not only the p_T or E_T but also the location of trigger object. The ¹ menu consists of different trigger paths, where each path corresponds to certain selection criteria.

The definition of L1 electron trigger '*L1_SingleIsoEG20*', in the current analysis, requires the presence of an energy deposit in the ECAL with a minimum transverse energy of 20 GeV. At the HLT level, the trigger path ⁵⁴ ⁷ '*HLT_Ele23_WPLoose_Gsf*' has been used, which requires the ECAL energy deposit of transverse energy greater than 23 GeV, along with a 'loose' criterion on the

identification of electron.

²⁶

Chapter 4

Event Simulation and Reconstruction

Event simulation is an essential component in the operation of any experiment. The simulation study of a detector is quite important before and even after the beginning of real data taking. All the reconstruction algorithms, analysis strategies and trigger paths for various processes as well as the operational details of an experiment are well optimized in the simulation process. This helps to analyse the performance of different components of the detector and to fine-tune the event generators which is important to check the modeling of detector in the simulation. The experimental output from real data analysis is compared to the simulation study obtained using the Monte-Carlo (MC) method [65], in order to interpret and validate the results.

The general structure of a simulation process consists of, the generation of a collision event starting from the proton-proton interactions until the production of final decay products and the simulation of detector which models the interactions between particles generated inside the detector material. Physics event generation and detector simulation are the earliest steps in the event processing chain that leads to MC samples suitable for an analysis. The event generation procedure and the modeling of physics processes is discussed briefly in the following sections.

¹⁰

4.1 Event Generators

The generation of high energy collision events is based on a procedure that uses random number generation and probability statistics. The event generation is performed starting with initial conditions, constructing the matrix elements according to the Feynman rules and subsequently calculating the cross section of the process under study at leading order or next-to-leading order. The hard scattering process often contains parton emissions emerging from initial and final states and are included in the event generation procedure. Hence, a general scheme of the event generator involves the simulation of a hard process, evolving through parton showering and hadronization step and the decay of the unstable particles. The event information contains the four-momenta of the final state particles.

The incoming as well as the outgoing partons of the hard interaction can radiate soft and hard gluons depending on how off-shell the partons are. Partons shower until energy scale of the shower reaches an infrared cutoff at which a non-perturbative transformation of colored partons into color-singlets takes place at the hadronization scale (Q_{had}). There are different MC event generators available in high energy physics which comprise different hadronisation phenomena. The most commonly used fragmentation models are the Lund String [66–68] and Cluster [69] model.

The accuracy of MC event generator depends on the choice of its free parameters which must be tuned to make the generator describe experimental data in the best possible way. This is referred to as generator tuning. Such parameters are available all the way from perturbative domain (hard interation) such as the value of α_s , to the non-perturbative domain (hadronization process). The majority of parameters however, are found in the non-perturbative physics models. A systematic approach to MC tuning is used, to constrain first the perturbative parameters and thereafter the non-perturbative ones. The MC generators that have been used in the present work are illustrated below.

MADGRAPH

MADGRAPH [70] is a tool for generating matrix elements for high energy $2 \rightarrow n$ collisions at ¹¹ leading order. The event information of the hard process is interfaced with parton shower programs which models the parton showering, hadronization and other steps of event generation. While the previous versions of MADGRAPH were written in FORTRAN77, MADGRAPH5 [71] is written in Python which implements a number of efficient algorithms with improved performance and functionality. It is capable of handling tree-level calculations for any user defined Lagrangian.

There is a method which can construct the Parton Shower Monte Carlo (SMC) generator matched to the NLO computations of a QCD process. The tool known as MC@NLO [72] has various features for generating fully exclusive events ³⁶ with hadronization according to the MC models and computing the total exclusive rates to NLO accuracy. With this method, a small fraction of negative weights is generated with an available unweighting technique. A unique framework which merges all the features of MADGRAPH5 and MC@NLO includes several possibilities that can perform NLO plus shower computations, with the MC@NLO formalism. In the current study, MADGRAPH5_AMC@NLO [73] event generator, referred as aMC@NLO, with tune CUETP8M1 [74] has been used and the samples are produced with NNPDF3.0 [36, 37] PDF. The FxFx technique [75] is used to merge jet multiplicities.

PYTHIA

¹ PYTHIA is a parton shower based MC event generator. The matrix elements are calculated at leading order and the higher order processes are modelled by parton showers. The showering is based on DGLAP evolution scheme [29–31] and the emissions ¹ are ordered in transverse momentum. The hadronization process is described by the Lund String model. PYTHIA was originally written in FORTRAN77 known as PYTHIA6 [76] and the C++ based version PYTHIA8 [77] was introduced later in 2007 with an improved model for multi-parton interactions. In this thesis, PYTHIA8

with tune CUETP8M1 has been used.

POWHEG

POWHEG [78–81] stands for POsitive Weight Hard Emission Generator. It can generate the hardest emission with a technique that yields positive weighted events using NLO matrix elements. The POWHEG output can be interfaced with any SMC program which allows the modelling of the parton shower and non-perturbative effects. The SMC generator should either be p_T ordered or able to apply a p_T veto in order to not double count the first hard emission when interfacing with the parton shower. In this thesis, POWHEG interfaced with PYTHIA8 has been used.

4.2 Detector Simulation

Simulation of high energy events is the first step in the MC event processing chain. The MC generators discussed in Sec 4.1 model the physics processes only on parton level. In order to compare the real collision events to prediction, MC simulation should be available on the detector level. Hence, the interaction of particles with the detector material has to be simulated separately. The primary goal of the simulation programme is to efficiently model the interactions involved, the detector performance and the event reconstruction such that simulated events are as close as possible to real data events. The CMS full simulation is based on GEANT4 [82, 83] software toolkit which is interfaced to a wide collection of MC event generators and includes a full event reconstruction.

GEANT4 provides tools for modeling full detector geometry and sensitive detector response, when a particle is generated in the detector volume by various physics processes including electromagnetic and hadronic interactions. It provides interface required for tuning and monitoring the information from particle tracking through the detector. GEANT4 uses the standard CMS software (CMSSW) framework and utilities. The simulation programme starts with an input provided by the

event generators in HEPMC format and then adds to itself the collection of simulated tracks and vertices, hits recorded in each subsystem, digitization data and reconstructed objects. The simulated hits can be overlaid with additional low p_T hadronic events ¹⁶² in order to simulate the effect of pileup. The digitization step involves the modeling of detector electronic response provided by custom code which describes the conversion of the energy deposit in the sensitive elements of the detector into digital signal. The output is the simulated data in a format identical to real collision events which is used to simulate Level1 and High Level Trigger decisions using the same algorithms implemented online in the CMS Trigger system. The data is then converted in a format which can be processed by the reconstruction algorithms.

In some cases, a parametric approach is used to simulate and reconstruct events with the CMS detector which uses the fast simulation package. The purpose of fast simulation is to reduce the CPU time overhead ⁸ in order to produce an accurate simulation of the detector effects. This step generates an output file in a format already comparable with the real data.

4.3 Event Reconstruction

¹ In order to perform an optimal measurement of particles recorded by the detector, ¹ an excellent reconstruction of final objects is needed. The reconstruction algorithms use information from one or more subdetectors of the CMS experiment to build different classes of particle candidates.

The process for the CMS event reconstruction is based on local reconstruction within the individual detector modules, global reconstruction inside the whole detector and combination of the two to produce physics objects. The input to the local reconstruction unit is the raw data collected by the detector and the corresponding output is reconstructed hits known as ‘RecHits’ which are basically position measurements in tracking detectors and calorimetric clusters in calorimeter systems. The RecHits are used as an input to the global reconstruction system in which the

information from different sub-detectors is combined within the sub-detector. In the final step, the output from individual subdetectors is grouped to produce reconstructed objects suitable for physics analysis, for eg. the electron candidates from calorimeter system are matched to tracks from the tracker system.

1 This section is devoted to the study of reconstruction algorithms and selection criteria of physics objects studied in this analysis along with the software and computing tools used in the CMS. Identification is a method to efficiently distinguish between real physics objects and fakes, which get misreconstructed or mismeasured. An example can be a jet depositing its energy in ECAL and hence getting reconstructed as an electron. Every physics object has a set of characteristics which can be used for its identification and selection of these variables is based on the efficiency of signal acceptance and background rejection.

4.3.1 Primary Vertex Reconstruction

26 With the increasing instantaneous luminosity at the LHC, there is a finite probability to have more than one hard interactions between partons in the same bunch crossing. Thus, it is necessary to measure precisely the position of these interactions. The offline primary vertex reconstruction is performed in two steps. 1 First, the tracks are selected and arranged in clusters based on the z coordinate closest to the beam line. The grouping of tracks is performed with the Deterministic Annealing (DA) clustering method [84]. 1 Second, a three dimensional vertex fit is performed for each track using the Adaptive Vertex Fitter which is an iterative re-weight fit method. In this fit, each track is assigned a weight w_i corresponding to the i -th track, defined between $0 \leq w_i \leq 1$. Based on these track weights, each vertex is assigned the number of degrees of freedom as $ndof = 2 \sum_{i=1}^{N_{tracks}} w_i - 3$. A minimum requirement on this number is $ndof > 4$ and corresponds to having at least four tracks associated with the vertex. The outcome of the vertex reconstruction allows multiple possibilities for the primary vertex to which further requirements are applied:

- 1 z position within 24 cm of the nominal detector centre
- radial position within 2 cm from the beam spot

All the reconstructed vertices are ordered by the sum of squares of the transverse momenta (p_T)² of the tracks associated with the vertex. From the set of these reconstructed primary vertices, the hard interaction vertex is selected as the vertex with the maximum sum.

In order to match the number of reconstructed primary vertices in data, a weight factor is applied to the simulation based on the instantaneous luminosity. The ‘official’ pileup reweighting procedure for 2015 MC datasets is explained below.

4.3.2 Pileup Reweighting

The MC samples are generated to match the observed instantaneous luminosity profile. However, due to the increasing luminosity at the LHC, multiple interactions, as discussed in Section 2.2.2, occur simultaneously which makes it difficult to reproduce the same number of reconstructed primary vertices in MC generation as observed in data. In order to correct and reproduce the observed distribution in simulation, a weight is assigned to the MC events.

The reweighting of MC samples is not performed as a function of the number of primary vertices, rather the MC events are reweighted by the number of pileup interactions from data (n_{PUI}^{data}) over the number of pileup interactions from the simulation (n_{PUI}^{mc}). This is done since the distribution of the reconstructed primary vertices is sensitive to the implementation of the primary vertex reconstruction.

$$w_{PUI} = \frac{n_{PUI}^{data}}{n_{PUI}^{mc}} \quad (4.1)$$

4.3.3 Electron Reconstruction

In the study of dielectron invariant mass spectrum, electron reconstruction is the key aspect of the analysis. The electron reconstruction [85,86] is based on the measurement of energy deposits in the electromagnetic calorimeter. The reconstruction process gets complicated due to the large amount of material budget in front of the calorimeter which results in high rates of bremsstrahlung emission. The procedure used for the reconstruction of electrons in the CMS is summarized in Fig. 4.1 and will be discussed in the following sections.

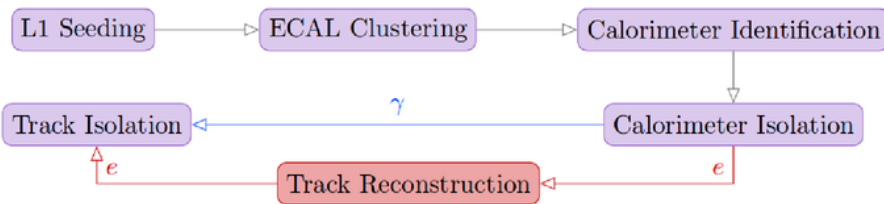


Figure 4.1: Flowchart of the electron reconstruction chain²¹.

4.3.3.1 Clustering

Electron and photon showers deposit their energy in several crystals in the ECAL. The electron reconstruction algorithm is based on the clustering of energy deposits in the crystals and the estimation of position and energy of electrons from this information. The spread in energy deposit depends on the material budget in front of the calorimeter which leads electrons to undergo bremsstrahlung. In order to measure the actual electron energy, energy of radiated photons should be collected which is spread mainly in ϕ direction, due to the magnetic field, with respect to the electron initial direction. A dedicated algorithm is used for this purpose which is different in barrel and endcap regions due to the difference in geometric arrangement of the crystals.

²¹Source : <http://dx.doi.org/10.1088/1742-6596/664/8/082001>

48
The ‘Hybrid’ algorithm in the barrel

The Hybrid algorithm is used in the barrel part with a simple $\eta - \phi$ geometry,
 45 collecting the energy in a small η window and an extended ϕ window. It looks for ‘seed’ crystals which are the local energy maxima with transverse energy above a given threshold $E_{Tseed} > E_{Tseed}^{threshold}$. Crystal dominoes aligned in η with the seed crystal are formed, the central crystal being at the same η_{seed} as of the seed crystal. This procedure is repeated $\pm N_{steps}$ in both ϕ directions around ϕ_{seed} . The domino size is 3 x 1 or 5 x 1 in $\eta \times \phi$ plane, depending on the seed crystal energy. The dominoes with energy not greater than $E^{threshold}$ are eliminated and the others are grouped in clusters. The clusters of dominoes are gathered to form superclusters.

The domino construction step is illustrated in Fig. 4.2.

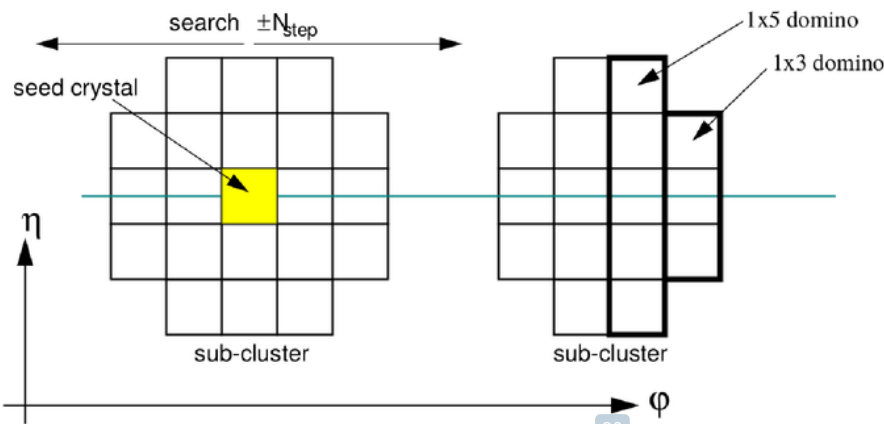


Figure 4.2: Domino construction step in the Hybrid algorithm used in the barrel region of Electromagnetic Calorimeter²².

The ‘Multi5x5’ algorithm in the endcap

The Multi5x5 algorithm is used in the endcaps which do not follow the $\eta - \phi$ geometry. The algorithm aims to build fixed size clusters of 5x5 crystal arrays around a seed crystal with a local maximal energy with respect to the surrounding four neighbouring crystals, which verifies $E_{Tseed} > E_{Tcluster}^{threshold}$. The 5x5 crystals are then

²²Source : <https://cds.cern.ch/record/687345>

grouped if their transverse energy is above a given threshold, $E_{T\text{cluster}} > E_{T\text{cluster}}^{\text{threshold}}$ aligned in η and ϕ with the seed cluster within $\Delta\eta$ - $\Delta\phi$ window. The preshower energies corresponding to the 5x5 clusters are added to the supercluster energy.

¹⁴⁶ The total energy of the supercluster is computed from the sum of energies of individual crystals which form the supercluster (sub-clusters). The position is calculated as the energy weighted mean of the sub-clusters. ²¹

4.3.3.2 Track Reconstruction

The electron track reconstruction should be able to collect hits in the tracker and access the parameters of the track associated with the energy deposit in the ECAL. ¹⁷² The tracking algorithm is designed and tuned to perform the reconstruction of a track compatible with the supercluster information. ¹⁶

⁸ The first step of the electron track reconstruction is the trajectory seeding. It consists of finding a pair of hits or triplet, called a seed, in the pixel detector, which is compatible with the energy and position of the supercluster. Two algorithms are used for this purpose: the ‘ECALDriven’ seeding starts from the supercluster and back-propagates the trajectory followed in the magnetic field, towards the inner layers of the pixel detector; the ‘TrackerDriver’ seeding starts from the trajectory seeds extrapolated towards the supercluster.

The TrackerDriven algorithm starts with the tracks reconstructed using a Kalman Filter (KF) method [87], which proceeds through each layer of the silicon tracker and adds measured hits in the subsequent layer, consistent with the propagated trajectory. The electron energy losses are modeled using a dedicated Bethe-Heitler function. To account for the high rate of bremsstrahlung emission and to improve the track finding efficiency, a very loose requirement on the track hit position compatibility with the prediction is used. Since the KF is unable to follow the change of curvature of the electron trajectory due to the photon radiations, a Gaussian Sum Filter (GSF) [88] fit to the KF track is performed for the estimation ⁷⁴

of track parameters.

The GSF is a nonlinear generalization of the KF, in which the distributions of all errors are Gaussian mixtures. This method approximates the energy loss in each layer with a mixture of Gaussian distributions rather than a single Gaussian. To each gaussian distribution a weight describing the associated probability is attributed. The hits are collected efficiently along the full trajectory, at both ends of the track which yields a good estimation of the electron track parameters at the ECAL entrance. The GSF filter is applied to all the track hit candidates in both directions, outside-in and inside-out, which helps in the evaluation of the fractional energy carried away by bremsstrahlung photons from the outermost and innermost track parameters.

4.3.4 Energy Scale Corrections

The measurement of electron energy provided by the supercluster algorithms is obtained by simply adding the deposits measured in the crystals. The ϕ spread of the energy depends on the amount of radiations emitted by the electron due to the interactions with tracker material before reaching ECAL. The reconstructed energy, $E_{\text{meas}}/E_{\text{true}}$ has a peak at a few percent less than unity due to the unrecovered energy from bremsstrahlung emission resulting in discrepancies between data and simulated energy. These discrepancies depend on the detector conditions and on the quality of electrons, they vary differently for different regions of the ECAL detector. Hence, the electron energy scale is corrected such that the mass of Z boson agrees well between data and simulation. These corrections are obtained using the standard CMS technique and the detailed description can be found in [89].

4.3.5 Electron Selection Strategy

In physics analysis with di-electron final states, it is crucial to identify isolated signal electrons and separate them from background sources, mainly electrons originating from photon conversion or jets faking electrons.²¹ The high magnetic field and a tracker with thick material have a great impact on the electron selection. The following section describes the strategies developed in CMS for the identification and isolation of electrons.

4.3.5.1 Identificaton

Electron identification is based on simple algorithms which use a set of discriminating variables to distinguish between real and background electrons. Three main categories of variables are used. The pure calorimetric observables which help in separating real electrons from objects like jets in the electromagnetic component.⁵ These variables are mainly based on the shower shape in the ECAL since the shape⁵ is different for hadrons involved in jets. The pure tracking observables which help to improve the separation between electrons and charged hadrons and make use of the tracking information provided by the Kalman Filter and the Gaussian Sum Filter. Lastly, the track-cluster matching observables which require consistent information between the ECAL and the tracker. The matching can either be geometrical or based on the comparison between the energy deposit in the ECAL (supercluster)²⁰ and the track momentum (GSF track).

The ‘cut based selection’ is applied on the following variables:³⁶

- H/E : The ratio between energy deposits in HCAL and ECAL.
- E/p_{in} , E_{seed}/p_{in} and E_{seed}/p_{out} : Energy-momentum matching variables between the total energy of the supercluster (E) or the supercluster seed (E_{seed})³⁶ and the track momentum measured at the vertex (p_{in}) or the calorimeter entrance (p_{out}).

- $\Delta\eta$ and $\Delta\phi$: Geometrical matching between the position of electron supercluster in the ECAL and the direction of track at the vertex extrapolated to the supercluster.
- $\sigma_{in\eta}$: Calorimeter shower shape variable, measures the spread in η for the energy deposited inside a 5x5 ECAL crystal matrix centered on the highest energy crystal of the supercluster.
- d_0 and d_z : Transverse and longitudinal impact parameter of the electron track with respect to the reconstructed primary vertex.

A criteria for the rejection of secondary electrons originating from the bremsstrahlung emission due to high photon conversion rates and the separation of converted photons from a prompt electron is also applied:

- *Missing Hits*: Number of crossed layers without compatible hits in the innermost tracker layers.
- *Conversion Veto*: A veto to reject the electrons from converted photons.

4.3.5.2 Isolation

A large fraction of real to background electrons is due to misidentified jets. The electron candidates have a significant energy flow around them and requiring the electrons to be isolated from nearby activity of charged particles or energy deposits can reduce the contamination from these background sources. The isolation is defined using the candidates reconstructed in a geometric cone which is obtained in the $\eta - \phi$ coordinate space around the direction of the electron. This procedure is referred to as Particle Flow (PF) isolation technique [90, 91]. The cone is required to have $\Delta R = \sqrt{(\Delta\eta)^2 + (\Delta\phi)^2} < R_0$, where R_0 is defined to be 0.3 or 0.4. Three isolation observables, known as ‘PF candidates’, based on the type of reconstructed

particles are used: charged particles, neutral photons and hadrons. The particle flow isolation is then defined as following:

$$\text{Iso} = \sum p_T^{\text{charged had}} + \max\left(\sum p_T^{\text{neutral had}} + \sum p_T^\gamma - A_{\text{eff}} \cdot \rho, 0\right) \quad (4.2)$$

where the sums run over the charged candidates originating from the primary vertex and on the neutral candidates, including hadrons and photons both.

The isolation variables are among the most sensitive observables to the extra energy in the event due to pileup, which can effect the isolation efficiency at high number of interactions per bunch crossing. The charged component of isolation is independent of the pileup effect, once only candidates compatible with the primary vertex are chosen. However, in order to remove this effect for the neutral PF candidates, a correction ($\rho \cdot A_{\text{eff}}$) is applied by using the average energy density (ρ) and effective area (A_{eff}) which normalizes the estimator in such a way that the neutral candidates become independent of the number of pileup interactions. The procedure uses the FASTJET technique [92–94] in which the jets are reconstructed using the anti- k_T jet clustering algorithm [95].

4.3.6 Software and Computing

The CMS software and computing system aims to cover a broad range of activities including the design, construction and calibration of the detector; the storage, reconstruction and analysis of data.

4.3.6.1 CMSSW

The collection of software, referred to as ‘CMSSW’ consists of a number of sub-packages which are created to provide an extensive toolkit to perform software-related tasks. The CMSSW software is built around a framework, an Event Data

Model (EDM), and services needed by simulation, calibration and reconstruction modules that process event data which can be used by physicists to perform data analysis. These modules can be plugged into the application framework at run time, with no dependence on the computing environment. The EDM is centered around the concept of an ‘Event’ which is based on C++ object-oriented methodology and passes information from one module to another, during data processing.

4.3.6.2 ¹²⁶ ROOT

ROOT is a software framework designed at CERN for performing statistical analysis and data processing. It is a ²⁰ object-oriented programming written in C++ and has been integrated with other languages like Python. ROOT is very flexible ¹⁰⁶ and provides both a programming interface to use in own applications and a graphical user interface for interactive data analysis. There are many pre-defined classes and methods available, which enable to quickly access large amounts of data using the C++ interpreter. It have a wide range of applications, including histogram making to view and analyze distributions and functions, curve fitting, storing data in the form of ROOT files, various mathematical and statistical tools for data operation.

4.3.6.3 ⁸² Computing Model

In order to store a huge amount of data, the LHC computing environment has been constructed as a ¹⁶ distributed computing and data storage infrastructure, known as the ‘Worldwide LHC Computing Grid’ (WLCG). The set of Grid services comprise the computing and connectivity resources which are used by the CMS to perform data processing, MC event generation and all types of computing-related activities. The CMS computing model with a primary ‘Tier-0’ centre at CERN is supplemented by ‘Tier-1’ and ‘Tier-2’ computing centres at national laboratories and universities worldwide.

Chapter 5

Measurement of Drell-Yan Differential Cross section

The Drell-Yan (DY) differential cross section measurement is performed in the bins of dielectron invariant mass ($d\sigma/dm$) within the mass range $15 < m < 3000$ GeV. The differential cross section is measured at a center-of-mass energy $\sqrt{s} = 13$ TeV using an integrated luminosity of 2.3 fb^{-1} of proton-proton collision data collected using the CMS detector at the LHC during the year 2015.

The cross section per each mass bin is calculated using the following formula:

$$\sigma = \frac{N_u}{A \cdot \epsilon \cdot \rho \cdot \mathcal{L}_{int}} \quad (5.1)$$

where N_u denotes the background subtracted yield corrected for the detector resolution and final-state QED radiation (FSR) effect, A and ϵ are the acceptance and efficiency for signal events, ρ is the efficiency scale factor and \mathcal{L}_{int} is the integrated luminosity of 2015 dataset. The DY cross section is calculated in each mass bin using these factors and will be discussed in the following sections.

5.1 Data and Monte Carlo Samples

The measurement of the differential cross section presented in this chapter is based on the understanding of signal and background processes. Monte Carlo (MC) samples are used for the determination of efficiencies, acceptances and various systematic errors and to validate the data-driven techniques which are used to estimate and perform the background study in this analysis. These samples are generated using a variety of generators and processed with full CMS detector simulation based on GEANT4, including the trigger simulation and a full chain of CMS event reconstruction.

5.1.1 Collision Data

The data sample used in this analysis is based on proton-proton collision data recorded in 2015 using the CMS detector at $\sqrt{s} = 13$ TeV. The data events collected with single electron triggers during 2015 runs are analyzed. The recorded data corresponds to an integrated luminosity of 2.3 fb^{-1} .

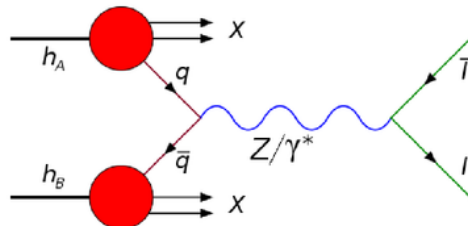


Figure 5.1: Leading order Feynman diagram of Drell-Yan process²³.

5.1.2 Drell-Yan Signal

The Drell-Yan (DY) signal is manifested by the presence of two isolated, well reconstructed and identified electrons as given in Fig. 5.1. The DY signal samples are

²³Source : https://en.wikipedia.org/wiki/Drell-Yan_process

¹⁷ simulated using the next-to-leading-order (NLO) aMC@NLO generator and are split ¹ into a sample of dielectrons with invariant mass $10 < m < 3000$ GeV. A list of signal samples used in this analysis is given in the Table 6.1. The M50 sample is truncated at 100 GeV by applying a cut on the mass constructed by two electrons with ‘isHardProcess’ generator flag in order to be combined with 100-200 sample. Fig. 6.1 shows the generator-level dielectron mass distribution obtained after combining the DY samples and normalized to the integrated luminosity.

Process	Sample	Cross section (pb)
$DY \rightarrow ll$	/DYJetsToLL_M-10to50_TuneCUETP8M1_13TeV-amcatnloFXFX-pythia8/RunIIFall15 MiniAODv2-PU25nsData2015v1_76X_mcRun2_asymptotic_v12_ext3-v1/MINIAODSIM	18610
	/DYJetsToLL_M-50_TuneCUETP8M1_13TeV-amcatnloFXFX-pythia8/RunIIFall15 MiniAODv2-PU25nsData2015v1_76X_mcRun2_asymptotic_v12-v1/MINIAODSIM	6025.2
	/DYJetsToLL_M-100to200_TuneCUETP8M1_13TeV-amcatnloFXFX-pythia8/RunIIFall15 MiniAODv2-PU25nsData2015v1_76X_mcRun2_asymptotic_v12_ext1-v1/MINIAODSIM	226
	/DYJetsToLL_M-200to400_TuneCUETP8M1_13TeV-amcatnloFXFX-pythia8/RunIIFall15 MiniAODv2-PU25nsData2015v1_76X_mcRun2_asymptotic_v12_ext1-v1/MINIAODSIM	7.67
	/DYJetsToLL_M-400to500_TuneCUETP8M1_13TeV-amcatnloFXFX-pythia8/RunIIFall15 MiniAODv2-PU25nsData2015v1_76X_mcRun2_asymptotic_v12_ext1-v1/MINIAODSIM	0.423
	/DYJetsToLL_M-500to700_TuneCUETP8M1_13TeV-amcatnloFXFX-pythia8/RunIIFall15 MiniAODv2-PU25nsData2015v1_76X_mcRun2_asymptotic_v12_ext1-v1/MINIAODSIM	0.24
	/DYJetsToLL_M-700to800_TuneCUETP8M1_13TeV-amcatnloFXFX-pythia8/RunIIFall15 MiniAODv2-PU25nsData2015v1_76X_mcRun2_asymptotic_v12_ext1-v1/MINIAODSIM	0.035
	/DYJetsToLL_M-800to1000_TuneCUETP8M1_13TeV-amcatnloFXFX-pythia8/RunIIFall15 MiniAODv2-PU25nsData2015v1_76X_mcRun2_asymptotic_v12_ext1-v1/MINIAODSIM	0.03
	/DYJetsToLL_M-1000to1500_TuneCUETP8M1_13TeV-amcatnloFXFX-pythia8/RunIIFall15 MiniAODv2-PU25nsData2015v1_76X_mcRun2_asymptotic_v12_ext1-v1/MINIAODSIM	0.016
	/DYJetsToLL_M-1500to2000_TuneCUETP8M1_13TeV-amcatnloFXFX-pythia8/RunIIFall15 MiniAODv2-PU25nsData2015v1_76X_mcRun2_asymptotic_v12_ext1-v1/MINIAODSIM	0.002
	/DYJetsToLL_M-200to3000_TuneCUETP8M1_13TeV-amcatnloFXFX-pythia8/RunIIFall15 MiniAODv2-PU25nsData2015v1_76X_mcRun2_asymptotic_v12_ext1-v1/MINIAODSIM	0.00054
$t\bar{t}$	/TT_TuneCUETP8M1_13TeV-powheg-pythia8/RunIIFall15 MiniAODv2-PU25nsData2015v1_76X_mcRun2_asymptotic_v12_ext3-v1/MINIAODSIM	831.76
tW	/ST_tW_top_5f_inclusiveDecays_13TeV-powheg-pythia8_TuneCUETP8M1/RunIIFall15 MiniAODv2-PU25nsData2015v1_76X_mcRun2_asymptotic_v12-v1/MINIAODSIM	38.09
$\bar{t}W$	/ST_tW_antitop_5f_inclusiveDecays_13TeV-powheg-pythia8_TuneCUETP8M1/RunIIFall15 MiniAODv2-PU25nsData2015v1_76X_mcRun2_asymptotic_v12-v1/MINIAODSIM	38.09
WW	/WW_TuneCUETP8M1_13TeV-pythia8/RunIIFall15 MiniAODv2-PU25nsData2015v1_76X_mcRun2_asymptotic_v12-v1/MINIAODSIM	118.7
WZ	/WZ_TuneCUETP8M1_13TeV-pythia8/RunIIFall15 MiniAODv2-PU25nsData2015v1_76X_mcRun2_asymptotic_v12-v1/MINIAODSIM	47.13
ZZ	/ZZ_TuneCUETP8M1_13TeV-pythia8/RunIIFall15 MiniAODv2-PU25nsData2015v1_76X_mcRun2_asymptotic_v12-v1/MINIAODSIM	16.523
$W + jets$	/WJetsToLNu_TuneCUETP8M1_13TeV-amcatnloFXFX-pythia8/RunIIFall15 MiniAODv2-PU25nsData2015v1_76X_mcRun2_asymptotic_v12-v1/MINIAODSIM	61526

Table 5.1: Names of the datasets and corresponding cross section values for the Monte-Carlo signal and background samples used.

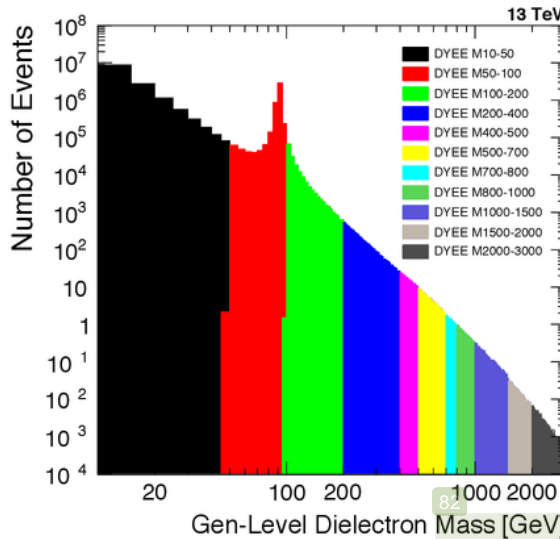


Figure 5.2: Generator-level mass distribution of the Drell-Yan signal sample (using aMC@NLO generator). Dielectron mass is constructed by two electrons with “isHardProcess” Gen-Flag.

5.1.3 Background Processes

Various physical processes that have same signature in the final state can be misidentified as DY electron pairs and are considered as background processes. With well chosen selection requirements, a large contamination from these processes can be reduced. However, the remaining background contribution needs to be modelled precisely in order to accurately differentiate it from the signal. Various background processes which play an important part in this analysis, can be classified as:

- The true dielectron backgrounds which have two real electrons in the final state. This background category contains the electroweak processes namely $DY \rightarrow \tau\tau$, top production ($t\bar{t}$, single-top) and dibosons (WW, WZ, ZZ).
13
- The fake electron backgrounds which have at least one jet faking a real electron.
130
This background category contains the QCD multijet and $W + jets$.
- The photon-initiated (PI) background process where both initial-state protons radiate a photon, which are misreconstructed as electrons.
2

DY $\rightarrow \tau\tau$

The leptonic decay $\tau \rightarrow \nu_\tau e \bar{\nu}_e$ has a branching ratio of 17%. The real electrons coming from $DY \rightarrow \tau\tau$ have an invariant mass lower than M_Z as opposed to the direct decay of Z boson into two electrons ($Z \rightarrow ee$). Hence, this background is a dominant source in the low and intermediate mass region $\sim 15 < M_{ee} < 70$ GeV.
The leading order Feynman diagram of this process is shown in Fig. 5.3.

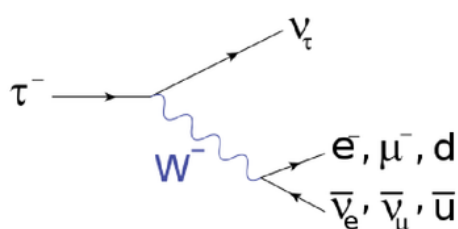


Figure 5.3: Leading order Feynman diagram for τ decay²⁴.

t-bar t decay

The dominant top quark production channel at LHC is the pair-production of top-antitop quark pair ($t\bar{t}$) as can be seen in Fig. 5.4 which represents the leading order Feynman diagram of $t\bar{t}$ production process. The top quark decays into a W boson in association with (a) bottom (b) quark. The final state of $t\bar{t}$ decay consists of missing transverse energy and two well identified real electrons from the decay of W bosons.
This is a dominant background process in the high mass region of the DY mass spectrum.

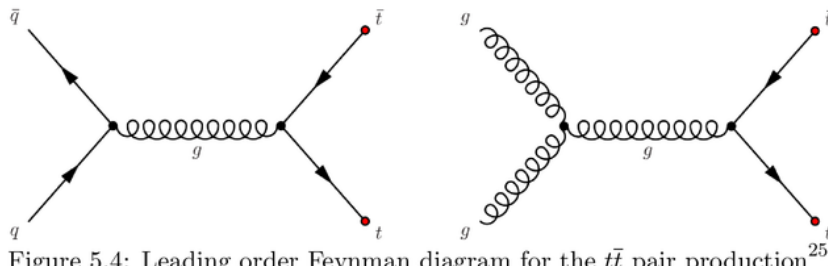


Figure 5.4: Leading order Feynman diagram for the $t\bar{t}$ pair production²⁵.

²⁴Source : [https://en.wikipedia.org/wiki/Tau_\(particle\)](https://en.wikipedia.org/wiki/Tau_(particle))

²⁵Source : https://en.wikipedia.org/wiki/Top_quark

Single-top decay

The production diagrams of single-top quark via weak interaction are shown in Fig. 5.5 which includes the s-channel, t-channel and tW-channel production. The maximum contribution comes from the tW ($\bar{t}W$) processes which lead to the production of two electrons via the leptonic decay of W boson. However, this background is minimal with a small contribution to the mass spectrum.

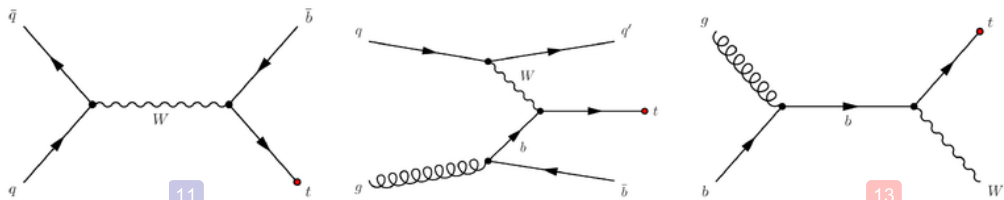


Figure 5.5: Leading order Feynman diagrams of the single top processes. From left to right: s-channel, t-channel and tW-channel²⁶.

Dibosons

The diboson processes WW , WZ and ZZ constitute the irreducible background to this analysis. These processes decay with two real electrons in the final state with $Z \rightarrow ee$ and $W \rightarrow e\nu$. However, since the cross section of these processes is not large, the fraction of background contribution is relatively small. The diboson production from $q\bar{q}$ is shown in figure Fig. 5.6.

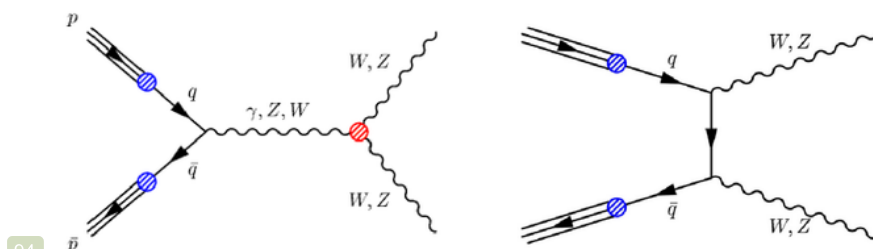


Figure 5.6: Leading order Feynman diagram for diboson production contributions from s-channel (left) and t-channel (right)²⁷.

²⁶Source : https://en.wikipedia.org/wiki/Top_quark

²⁷Source : <https://www-cdf.fnal.gov/physics/ewk/2008/WZatgc/>

W + jets

This is a sub-dominant background process which can be reduced by the electron selection requirement. The production of $W + jets$ process is described in the Fig. 5.7. The W boson decaying leptonically to an electron along with missing transvers energy can be a background source when the associated jet fakes an electron.

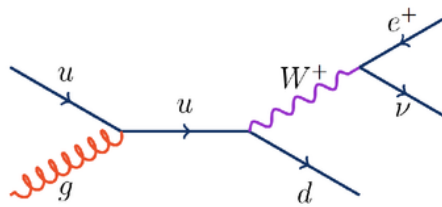


Figure 5.7: Leading order Feynman diagram for $W + jets$ production²⁸.

QCD hadronic decay

With a large production rate at the LHC energy, the QCD process becomes an important background to this analysis. The QCD events with multiple jets contribute maximally at the low DY invariant mass region. However, since these events do not survive the dielectron selection thresholds, they get highly suppressed at the event selection stage.

A list of background samples relevant to this analysis are listed in Table 6.1. All samples are processed using PYTHIA8 or POWHEG, except the $W + jets$ background sample which is generated with aMC@NLO.

5.2 Reweighting

There exist several corrections which improve the agreement between data and simulation and lead to a precise measurement of the cross section. All such corrections and reweight techniques are discussed in this section.

²⁸Source : <http://cds.cern.ch/record/1376067>

5.2.1 Pileup Reweighting

The simulation does not reproduce the number of reconstructed primary vertices as observed in data. As discussed in Section 4.3.2, a weight factor is applied to the simulated events in order to correct the MC distribution. These corrections are applied as an event weight to the MC and are calculated from the distribution of number of pileup interactions in data and simulation, assuming a Minimum Bias (MB) cross-section of 71.0 mb at $\sqrt{s} = 13$ TeV.

Figure 5.8 compares the number of primary vertices in data and MC samples used in this analysis. The pileup reweighting considerably improves the data-MC agreement.

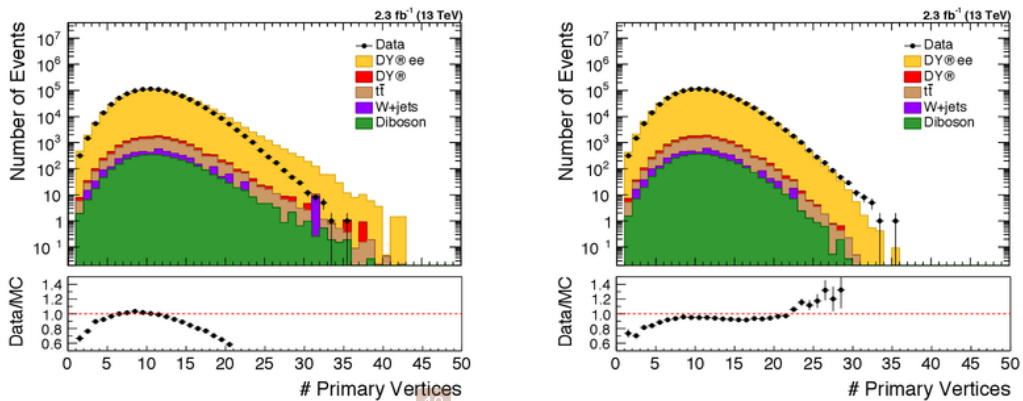


Figure 5.8: The distribution for number of reconstructed primary vertices in data (black circles) and Monte-Carlo prediction (histograms) before (left) and after (right) applying the pileup reweighting.

5.2.2 Scale Corrections

The electron energy is derived primarily from the measurements of the energy deposited by electrons in the ECAL. The electron energy measurement depends on the alignment, synchronization and other aspects of detector operation which can effect the reconstruction of dielectron invariant mass. In order to recover the bias in data and MC simulation, the electron energy scale is corrected as discussed in detail in

the Section 4.3.4.

The effect of these corrections is visible in the Z -peak region and can be seen in Fig. 6.2. A better agreement between data and simulation is observed after the application of energy scale and smearing corrections.⁹

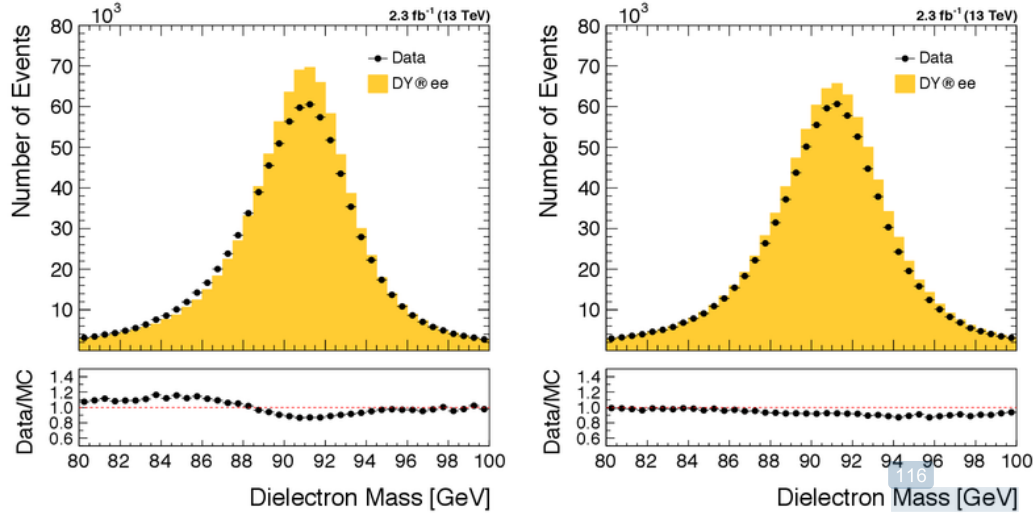


Figure 5.9: The left and right plots show the mass distribution for the Z -peak region, before and after applying the energy scale and smearing corrections respectively, for data (black circles) and Monte-Carlo prediction (yellow histogram). The Drell-Yan signal is normalized to the number of data events.

5.3 Drell-Yan Event Selection

¹²⁹ The selection of events for the DY cross section measurement in the electron final state begins with a requirement to pass the unprescaled trigger having a minimum threshold on the transverse momentum of electron candidate ensuring high signal yield. The single electron trigger `HLT_Ele23_WP Loose_Gsf`, with a p_T requirement of 23 GeV is used to select the dielectron events.⁵

In order to reduce the backgrounds at the event selection stage, various kinematical and identification requirements are imposed on the electron candidates as explained below.

Kinematics

⁴ The leading electron in the event is required to have $p_T > 30$ GeV and the trailing electron $p_T > 10$ GeV, which allows to operate on the plateau region of the trigger efficiency. The ECAL fiducial region is obtained from the pseudo-rapidity of the supercluster (η_{sc}) with $|\eta_{sc}| < 1.4442$ (barrel) and $1.566 < |\eta_{sc}| < 2.5$ (endcap). The barrel-endcap transition region ($1.4442 < |\eta_{sc}| < 1.566$) is partially shadowed by cables and therefore have degraded resolution and efficiency. The transition region is hence, excluded in this analysis.

Identification

¹⁷ The electrons are identified using a set of cuts applied on the variables which determine the characteristics of calorimeter and tracker and are based on the distribution of electromagnetic shower in the ECAL, a matching trajectory of an electron track with the clusters in the ECAL and consistency with origin of the track from the primary vertex in order to reduce the misidentification rate. The cut values are defined separately for the barrel and endcap regions of the calorimeter and are summarized in the Table 5.2. This analysis uses the Medium Working Point (WP) [96] for the identification of electrons with a requirement to pass the particle flow isolation

¹⁰⁹ defined within a cone of $\Delta R = \sqrt{(\Delta\eta)^2 + (\Delta\phi)^2} < 0.3$ around the electron direction, as described in the Section 4.3.5.2. The distribution for various identification variables is presented in Fig. 5.10.

In Fig. 5.11 and 5.12 the kinematic variables p_T , η (rapidity) and ϕ of the electrons (dielectrons) are presented. The electron yields from data and MC events ² in the bins of dielectron invariant mass can be seen in Fig. 5.13. The plots show the number of events at the detector level, as well as Data/MC ratio, after correcting ¹ for electron energy scale and pileup effects as discussed in the Section 5.2. A good ¹⁴⁵ agreement is observed between data and MC prediction.

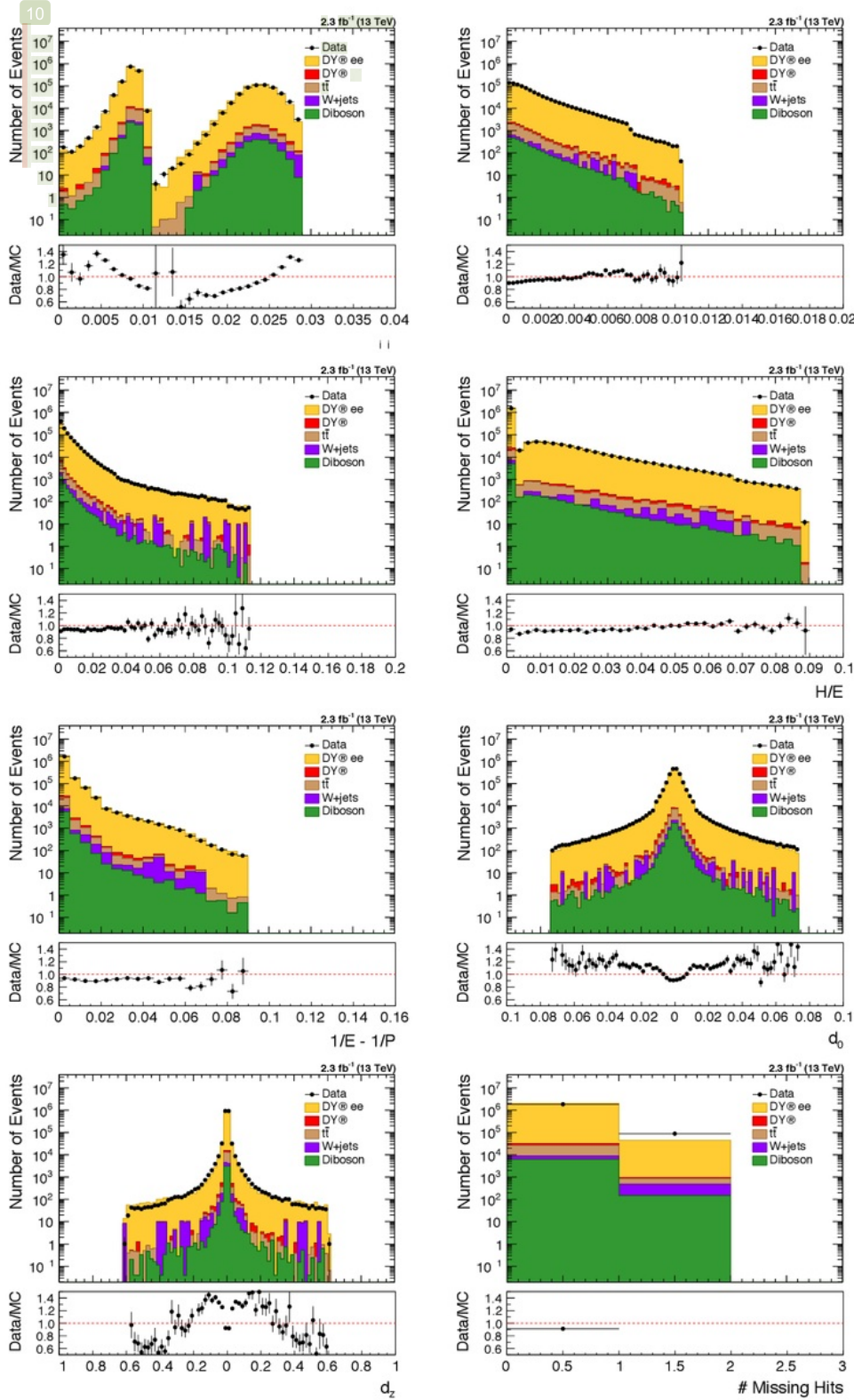


Figure 5.10: Electron identification variables for data (black circles) and Monte-Carlo prediction (histograms) listed in Table 5.2

Variable	Barrel	Endcap
$\sigma_{in} <$	0.0101	0.0283
$\Delta\eta_{ln} <$	0.0103	0.00733
$\Delta\phi_{ln} <$	0.0336	0.114
$H/E <$	0.0876	0.0678
PF Isolation <	0.0766	0.0678
$1/E - 1/P <$	0.0174	0.0898
$ d_0 <$	0.0118	0.0739
$ d_z <$	0.373	0.602
Missing Inner Hits \leq	2	1
Pass Conversion Veto	yes	yes

25

Table 5.2: Summary of Medium Working Point for the identification of electrons using cut-based approach in the barrel and endcap regions [96].

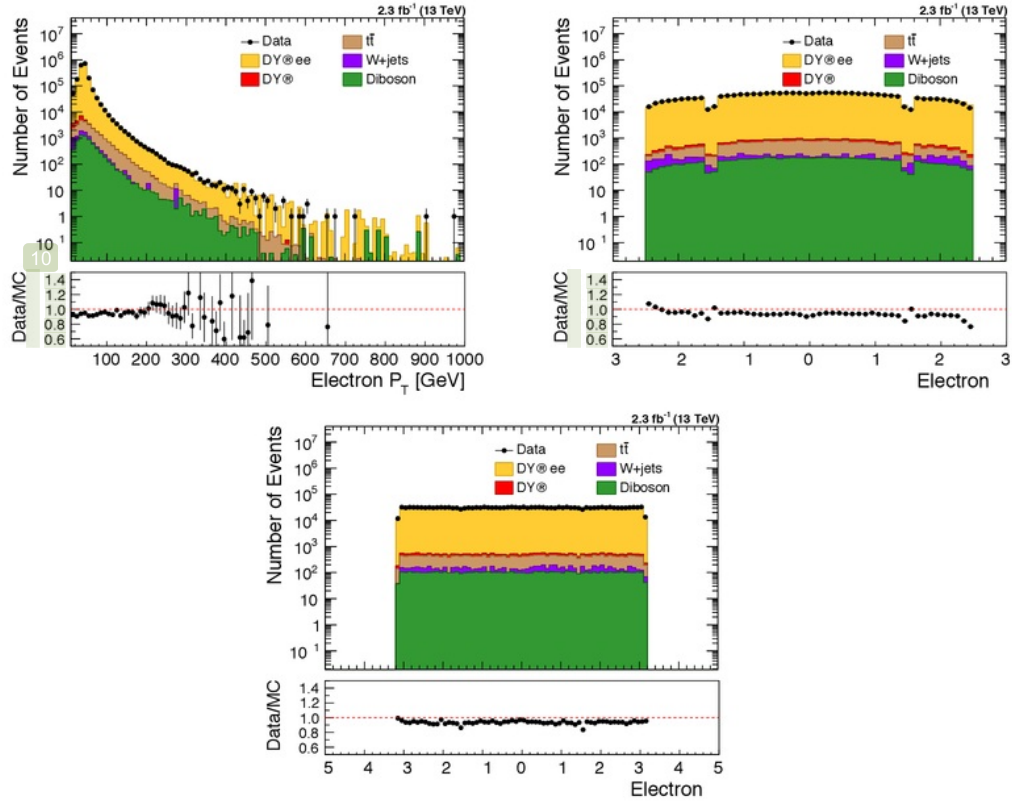


Figure 5.11: Electron kinematic variables p_T , η and ϕ after pre-selection (kinematic and identification cuts) in data (black circles) and Monte-Carlo prediction (histograms).

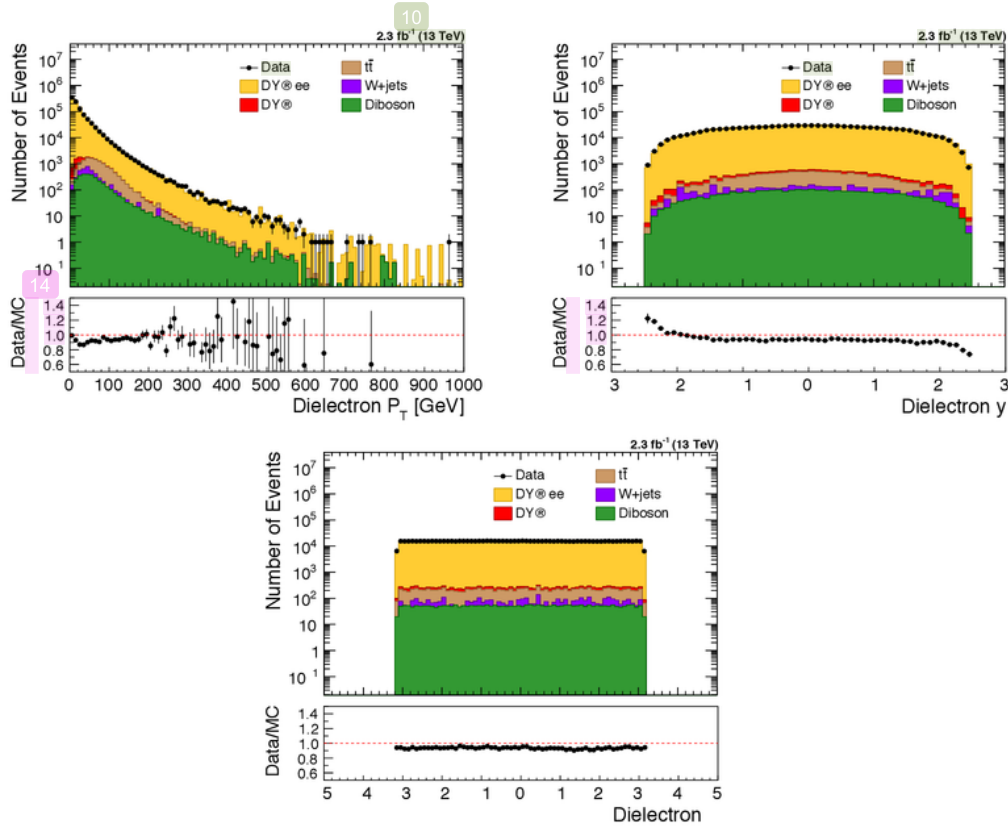


Figure 5.12: Dielectron kinematic variables p_T , η and ϕ after pre-selection (kinematic and identification cuts) in data (black circles) and Monte-Carlo prediction (histograms).

5.4 Background Estimation

The potential sources of background in the Drell-Yan (DY) analysis can be seen in Fig. 5.13. The composition of these backgrounds depends on the dielectron invariant mass region. From the MC prediction, dominant contribution over the entire mass range comes from $t\bar{t}$ whereas DY production of $\tau\tau$ pairs contributes maximal in the low mass region upto ~ 70 GeV. Other backgrounds with comparatively smaller contributions include dibosons (WW , WZ and ZZ), single-top (tW and $\bar{t}W$), QCD and $W + jets$ as already discussed in the Section 5.1.3. The prediction for these backgrounds is fairly reliable and we can consider using the MC prediction for back-

25

108

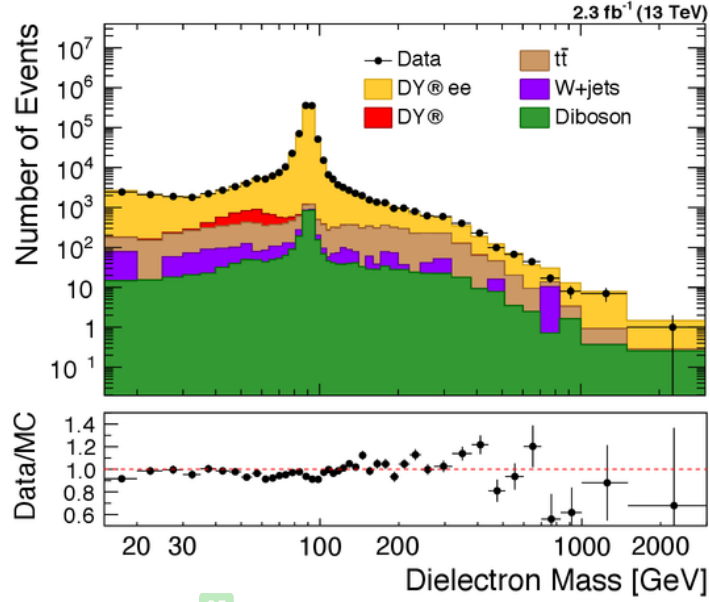


Figure 5.13: Drell-Yan mass distribution in data (black circles) and Monte-Carlo prediction (histograms for signal and backgrounds) from 15 to 3000 GeV. 65

ground subtraction in order to obtain the signal yield. However, the data-driven techniques are used to cross-check the level of background from the MC-based analysis and to assess the systematic errors described later. 19

5.4.1 Measurement of Dielectron Background using $e\mu$ Method

The data-driven technique which is based on the reconstruction of $e\mu$ pairs is used to estimate the true electron background sources namely top quark production (single or in pairs), WW and $DY \rightarrow \tau\tau$. These background processes being flavour symmetric, decay to $e\mu$ pair at twice the rate of dielectron events and hence the contribution of dielectron backgrounds can be scaled properly by the $e\mu$ events after accounting for detector acceptance and efficiency. The $W + jets$ background which contains only one real electron can mimic $e\mu$ final state and thus treated as a background to the $e\mu$ events.

The relationship between the number of e^+e^- and $e\mu$ events can be expressed as:

$$N_{e^+e^-}^{Est} = \frac{A}{2} \cdot \frac{1}{1+R} \cdot N_{e\mu}^{Obs} \quad (5.2)$$

where,

- $A = 2N_{ee}/N_{e\mu}$, N_{ee} and $N_{e\mu}$ are the numbers of e^+e^- and $e\mu$ events reconstructed in MC. Therefore, A is a ratio of detector acceptance times efficiency for e^+e^- relative to $e\mu$ selection.
- R is the ratio of $W + jets$ background to $e\mu$ events and becomes $(N_{W+jets})/(N_{DY \rightarrow \tau\tau} + N_{t\bar{t}} + N_{tW} + N_{\bar{t}W} + N_{WW})$. $R = 0$ when there is no $e\mu$ background.
- $N_{e\mu}^{Obs}$ ¹⁵ is the number of $e\mu$ events observed in data and $N_{e^+e^-}^{Est}$ is the expected number of e^+e^- background.

$N_{e^+e^-}^{Est}$ ⁷¹ is calculated on a bin by bin basis since A and R vary as a function of invariant mass.⁸⁹

The electron candidate is required to satisfy the offline selection as described in the Section 5.3. The muon candidate which lies in the detector acceptance region $|\eta| < 2.4$, passes Tight identification criteria and the particle flow isolation [97] defined within a cone of $\Delta R = 0.3$ is selected. The selection requirement applied on the muon candidate is explained in the Table 5.3. The $e\mu$ events in data and MC are selected using an electron-muon trigger *HLT_Mu8_TrkIsoVVL_Ele17_CaloIdL_TrackIdL_IsoVL*, with a p_T requirement of 17 GeV and 8 GeV on electron and muon candidates respectively. In order to select the $e\mu$ pair, an opposite charge requirement is applied. The electron and muon are required to have $p_T > 25$ GeV and $p_T > 15$ GeV respectively. The kinematic variables p_T , η ⁷¹ and ϕ ⁸⁰ for the electron and muon candidates are shown in Fig. 5.14.

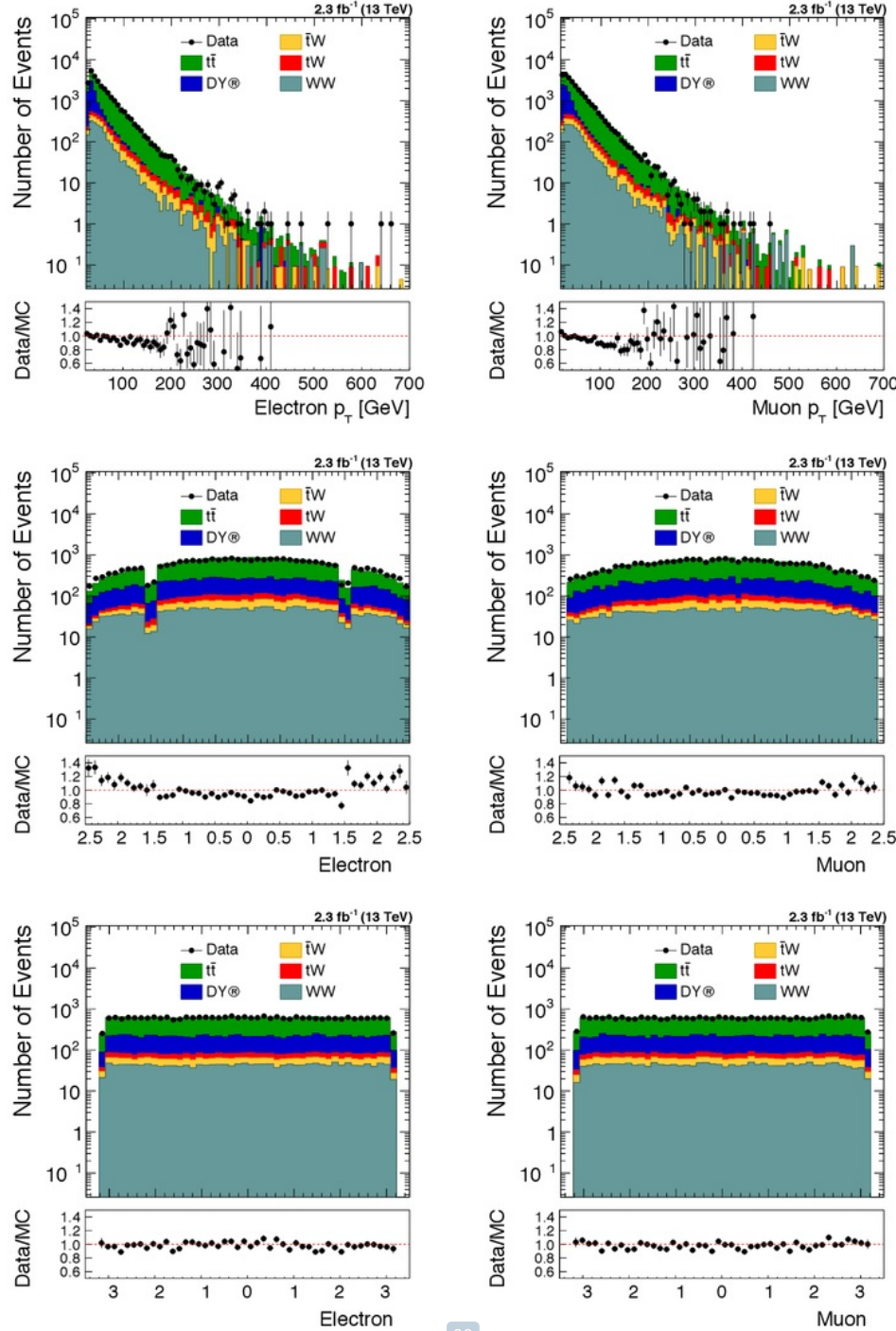


Figure 5.14: Kinematic variables p_T , η and ϕ for electron (left) and muon (right) candidates after pre-selection (kinematic and identification cuts for $e\mu$ selection) in data (black circles) and Monte-Carlo prediction (stack histograms).

Selection	Cut threshold
Muon identification	Each muon should be Global Muon $N_{pixel} > 0$ $N_{muon} > 0$ $N_{matchedstations} > 1$ $N_{trk.layers} > 5$ $ d_{xy}(PV) < 2 \text{ mm}$ $ d_z(PV) < 5 \text{ mm}$
PF Isolation	$\sum_{\Delta R < 0.3} (p_T)/p_T(\mu) < 0.15$
Vertex fit	$\chi^2 < 10$

Table 5.3: Summary of Tight Identification and Particle Flow Isolation for the selection of muon [97] for $e\mu$ method.

The $e\mu$ method is validated by performing a Closure test using the MC samples. In this test, the $e\mu$ events are counted directly from MC and e^+e^- events are predicted from the same MC samples using the technique described above. Fig. 5.15 (left plot) shows the comparison between the number of e^+e^- events from background MC samples and the number of e^+e^- events estimated from $e\mu$ MC. Since, the factor A is calculated on bin by bin basis, we expect an exact agreement between observed and estimated e^+e^- events obtained from MC. The results of the validation test are reported in the Table 5.4.

In order to estimate the e^+e^- background events from $e\mu$ data, the sample of $e\mu$ events in data and simulation is compared both for the number of events and the shape of invariant mass spectrum. The mass spectra of $e\mu$ events obtained is shown in Fig. 5.15 (right plot) and it can be observed that the simulation describes the data quite well. The number of $e\mu$ events 26629 ± 163 (stat) in data compared to 27605 ± 166 (stat) events in MC accounts to a difference 4% between data and MC.

To calculate the e^+e^- background, the $e\mu$ method is applied to $e\mu$ data events. Fig. 5.16 shows the comparison of the number of observed e^+e^- events from MC simulation (stacked histograms) and the number of estimated e^+e^- events obtained

#Events	Obs. $e\mu$	Obs. e^+e^-	Est. e^+e^-
data	26629 ± 163	–	11899 ± 109
mc	27605 ± 166	13066 ± 114	13066

Table 5.4: Total number of $e\mu$ and e^+e^- events observed in data and Monte-Carlo prediction and the estimated number of e^+e^- events from data and Monte-Carlo simulation, where all errors are statistical.

from $e\mu$ data (black circles). The estimation procedure yields 11899 ± 109 (stat) e^+e^- events. The average difference per bin between the estimated e^+e^- background and MC prediction is 10%, which is taken as the systematic error on the $e\mu$ method.
126

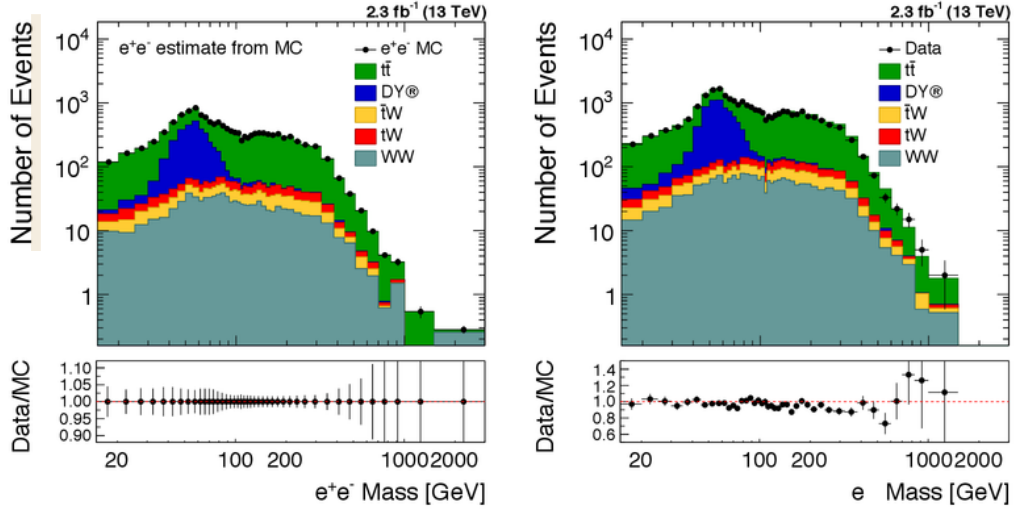


Figure 5.15: Left: The number of observed e^+e^- events from Monte-Carlo prediction (stacked histograms) and the number of estimated e^+e^- events obtained from $e\mu$ MC (black circles). Right: The number of observed $e\mu$ events in data (black circles) and Monte-Carlo prediction (stacked histograms).

5.4.2 Measurement of Dielectron Background using Fake Rate Method

In addition to real dielectron events from electroweak processes, there are QCD multijet and $W + jet$ events which contain atleast one misidentified electron. These backgrounds with fake e^+e^- events can be estimated using the misidentification rate

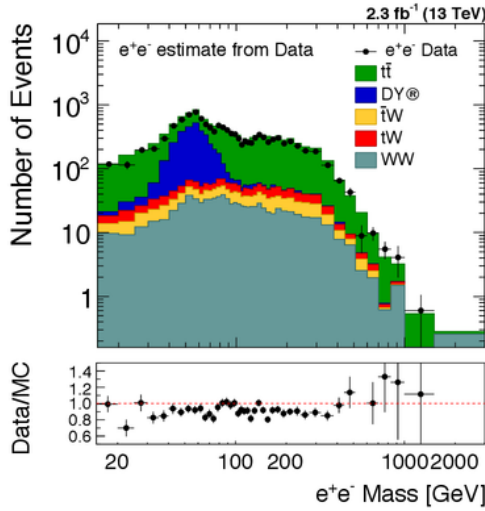


Figure 5.16: The number of observed e^+e^- events from Monte-Carlo prediction (stacked histograms) and the number of estimated e^+e^- events obtained from $e\mu$ data (black circles) using the $e\mu$ method.

technique called the “fake rate method”. In this method, the fake rate is calculated from single photon data sample by measuring the probability for a jet, which gets reconstructed as an electron, to pass the $DY \rightarrow e^+e^-$ selection as described in the [Section 5.3](#). The events used to measure the fake rate are selected using single photon trigger $HLT_PhotonX$, where $X = 22, 30, 36, 50, 75, 90, 120, 175$ and corresponds to different E_T thresholds, where $E_T = 175$ is the only unprescaled trigger available in this study. An ‘OR’ combination of these triggers is used in order to correctly calculate a single trigger decision and prescale at the HLT level. Fig. 5.17 shows the E_T distribution of the HLT photon object obtained from data, before and after applying the trigger prescale.

In order to calculate ‘jet to electron’ faking ratio, in addition to the trigger requirement, a set of cuts are applied on data and MC to ensure that the sample used to measure the fake rate is dominated by jets. The remaining sample is then referred to as ‘jet sample’.

The cuts applied to select the jet sample are listed below:

- No. of electrons passing DY selection ≤ 1
- Particle Flow MET < 20 GeV
- No. of missing hits = 0
- $dR \left(= \sqrt{d\eta^2 + d\phi^2} \right) < 0.5$

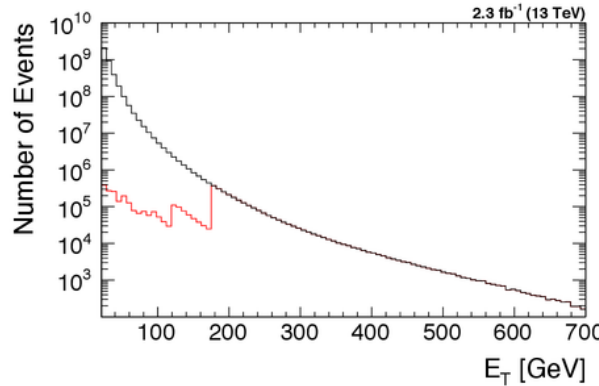


Figure 5.17: E_T distribution of the HLT photon object before (red) and after (black) applying the trigger prescale. The distribution is common after $E_T = 175$ GeV, which is the maximum threshold of single photon trigger.

The ‘atmost one’ condition on the number of electrons which pass the DY selection rejects the real dielectron events. A cut on the MET (missing transverse energy) removes the contamination from $W+jets$ events. The missing hits condition and dR (between the fakeable electron and HLT photon object) cut, ensures that the contamination from photons is removed, which can otherwise lead to a higher fake rate. The remaining contribution from photons is removed by subtracting the photon events in data from $\gamma + jets$ MC simulation. Similarly, the contamination from electroweak processes ($DY \rightarrow ee$, $DY \rightarrow \tau\tau$, $t\bar{t}$, single-top and dibosons) is removed from data by subtracting same events selected from MC.

The fake rate obtained after electroweak subtraction is shown in Fig. 5.18 as a function of electron p_T and is defined as the fraction of electrons that can be selected

from jet sample using the DY selection. In order to account for η dependence, the fake rate is calculated separately in barrel ($|\eta| < 1.4442$) and endcap ($1.566 < |\eta| < 2.5$) region and agree within the statistical uncertainties.

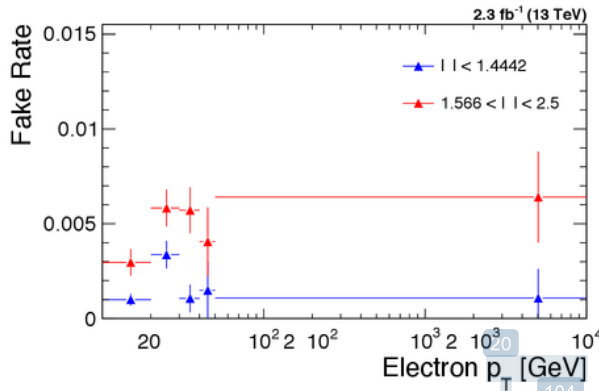


Figure 5.18: Electron fake rate obtained as a function of p_T in barrel and endcap regions separately, after performing the electroweak subtraction from Monte-Carlo prediction.

In order to estimate the QCD and $W + jets$ backgrounds, a sample of events is obtained from the single electron data sample. For QCD, since both electrons are fake, the sample contains two electrons which fail the DY selection, while for $W+jets$ the dielectron events constitute an electron which fails and another which passes the selection, each multiplied by a factor $\frac{f}{1-f} \times \frac{f'}{1-f'}$ and $\frac{f}{1-f}$ respectively, where f and f' corresponds to the fake rate of electrons failing the selection as a function of p_T and η . The contribution from electroweak processes which contaminate the above selection is subtracted from data using the MC simulation. The formula used for the estimation procedure is presented in eq. 5.3 and 5.4 for QCD and $W + jets$ backgrounds respectively. Fig. 5.19 shows the estimated dielectron mass spectrum obtained from the fake rate method. The estimated number of fake events are assigned a 50% systematic error, attributed to the feature that even with a generous error on the fake backgrounds, this error will not be a dominant systematic since the level of fake backgrounds is relatively low. Additionally, a study to compare the number of e^+e^- events obtained from MC prediction and data-driven estimate is

found to match within 50% and is reported in Table 5.5.

$$(N_{2F}^{data} - N_{2F}^{MC}) \cdot \frac{f}{1-f} \cdot \frac{f'}{1-f'} \quad (5.3)$$

$$(N_{1P+1F}^{data} - N_{1P+1F}^{MC}) \cdot \frac{f}{1-f} - 2 \cdot (N_{2F}^{data} - N_{2F}^{MC}) \cdot \frac{f}{1-f} \cdot \frac{f'}{1-f'} \quad (5.4)$$

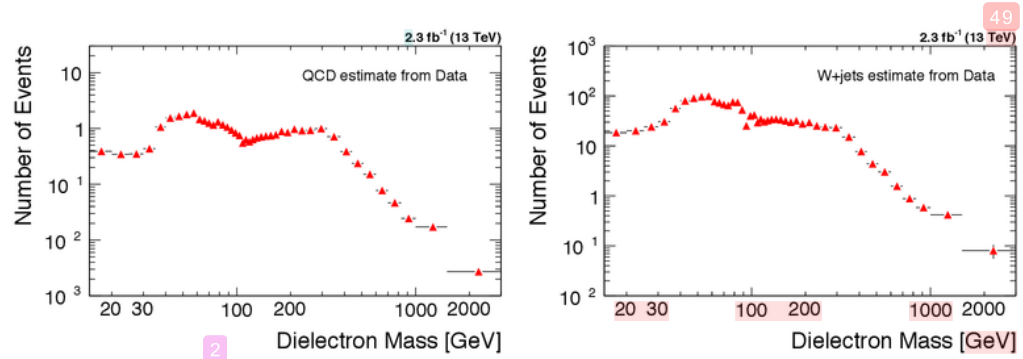


Figure 5.19: The number of e^+e^- events for QCD (left) and $W + jets$ (right) backgrounds estimated from data using the fake rate method.

e^+e^- events	QCD	$W+jets$
data	33	1532
mc	—	1500

Table 5.5: Total number of e^+e^- events observed in Monte-Carlo prediction and the estimated number of e^+e^- events from data.

While, all the backgrounds are estimated using data-driven techniques ‘ $e\mu$ method’ and ‘fake rate method’, WZ and ZZ diboson backgrounds are estimated from MC prediction since their contribution to the DY mass spectrum is not large. In order to take into account the difference between data and MC, a correction factor, which will be discussed later, is applied to the WZ and ZZ mass distributions.

The $\gamma\gamma$ -initiated production of same-flavour lepton pairs is estimated with the FEWZ 3.1 program [98, 99], using the MRST2004qed photon PDF set. The effects

are negligibly small for most of the mass range except for high mass region [100], which is smaller in comparison to the size of uncertainties from other sources in that region. Hence, the PI contribution is not considered in this analysis.

² The expected shapes and relative dielectron yields in bins of invariant mass, from data and MC (signal and backgrounds) events after performing background estimation from data-driven methods is shown in Fig. 5.20.

The contribution of each background process to the DY mass spectrum is obtained in Fig. 5.21. From the plot, it can be seen that the major contribution comes from $DY \rightarrow \tau\tau$ ³⁵ in the low mass region while in the high mass region, the backgrounds $t\bar{t}$, tW , $\bar{t}W$ and WW are dominant.

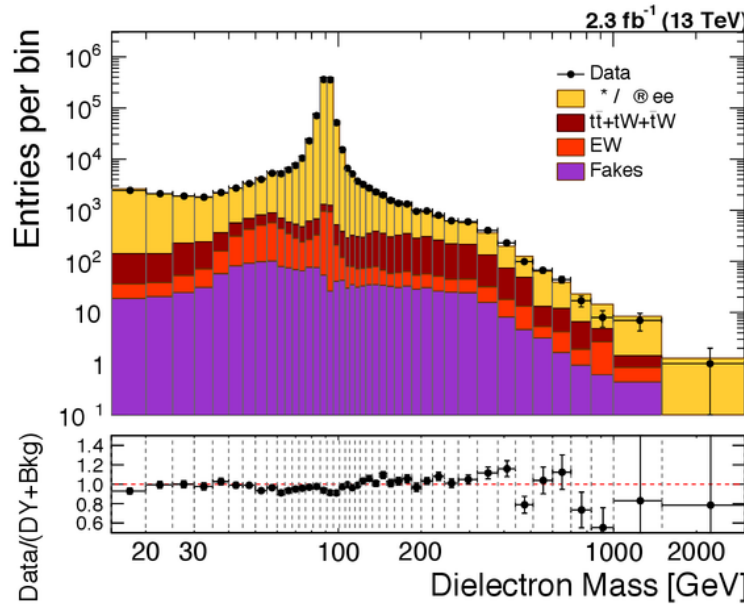


Figure 5.20: The observed dielectron invariant mass spectra for data (black circles) and Monte-Carlo (stacked histograms) events and the corresponding ratio of observed to expected yields. EW means the contribution from WW, WZ, ZZ and $DY \rightarrow \tau\tau$, Fakes corresponds to the contribution from QCD and $W + jets$.

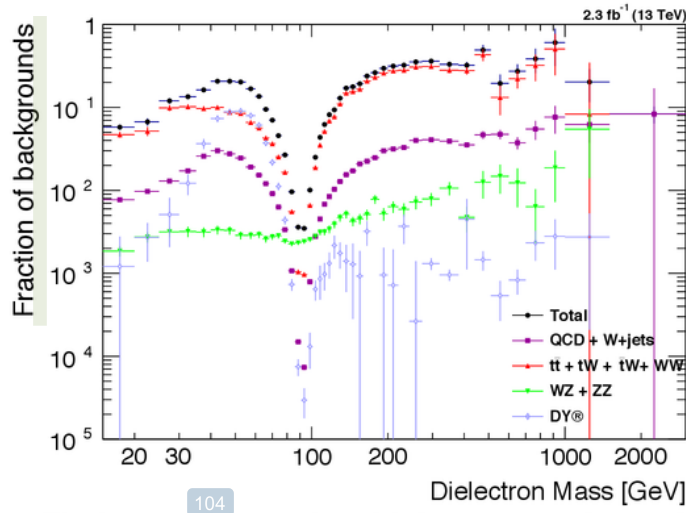


Figure 5.21: The fraction of the number of dielectron events from each background process with respect to the total observed number of data events. ‘Total’ corresponds to the combined fraction for all the backgrounds estimated from data-driven methods and Monte-Carlo simulation.

5.5 Corrections

The reconstructed dielectron mass distribution obtained by background subtraction, does not take into account the loss of events due to detector resolution, detector acceptance, reconstruction and selection inefficiencies and FSR, a process not included in the MC calculations. In the following text, we refer ‘post-FSR’ and ‘pre-FSR’ to anything defined before and after the FSR effects. As a result of these limitations, the measured yield cannot be directly compared with the Standard Model theoretical expectations. Therefore, the measurement of differential cross section ($d\sigma/dm$) requires a four-step correction procedure. The measured distribution is first corrected for the detector resolution effects by an unfolding technique. The unfolded distribution is then corrected for detector acceptance (A) and efficiency (ϵ). After the acceptance correction, the mass spectra is corrected by a scale factor (ρ), to account for difference in the efficiency between data and simulation. As a last step, the pre-FSR dielectron mass distribution is obtained by correcting for the radiation effects and can be compared to various theoretical predictions.

5.5.1 Unfolding

The experimental results are often distorted and migrated to adjacent bins due to limited detector resolution. These migration effects can bias the cross section measurement and hence, corrected through an unfolding procedure [101] which uses the invariant mass distribution from simulation. This technique maps the true dielectron distribution onto the measured one, taking into account the migration of events and has been implemented using the RooUnfold software package [102].

¹ The detector effects are parametrized by using a response matrix which is determined from the electrons that pass the kinematic cuts and detector acceptance. For 1-dimensional measurement, the response matrix element T_{ik} gives the fraction of events from bin k of the true distribution N_k^{true} that ends up reconstructed in bin i of the observed distribution N_i^{obs} (in the limit of no background), which are related to each other as shown in eq. 5.5. The true invariant mass spectrum is then obtained by inverting the response matrix using eq. 5.6.

$$N_i^{\text{obs}} = \sum T_{ik} N_k^{\text{true}} \quad (5.5)$$

$$N_k^{\text{true}} = \sum (T_{ik})^{-1} N_i^{\text{obs}} \quad (5.6)$$

⁶⁹ The true mass is defined as the ‘generator-level’ dielectron invariant mass and is obtained from the electrons after FSR has taken place (post-FSR electrons). The observed mass is calculated by electrons which pass the full DY selection at the ‘reconstruction-level’. RooUnfold package provides several algorithms among which iterative D’Agostini method has been used to unfold the experimental results in this analysis. This method can be used until convergence for which the number of iterations is determined by selecting the first iteration number ‘i’ when the relative ²⁵ difference of the number of events in unfolded distribution with the $(i+1)^{\text{th}}$ iteration

47

result is smaller than 0.1% for all mass bins as specified in eq. 5.7, where n^i is the number of events in a mass bin after unfolding with ‘i’ iteration.

Using this technique the number of iterations obtained is 21.

$$\frac{|n^i - n^{(i+1)}|}{n^i} < 0.1\% \quad (5.7)$$

Fig. 5.22 shows the correlation plot between the generator-level and reconstructed-level dielectron mass which is used to unfold the background subtracted yield. The horizontal band extending towards left can be traced to the events which experience radiation effects ⁴ in the Z -peak region due to which the generated mass has a lesser value compared to reconstructed mass. The reconstruction of electrons uses an algorithm, as discussed in Section 4.3, which along with the electrons, picks up radiated photons and hence, in some cases, the reconstructed dielectron mass is closer to the mass prior to FSR effect (pre-FSR mass) and can be different from the post-FSR generator-level dielectron mass.

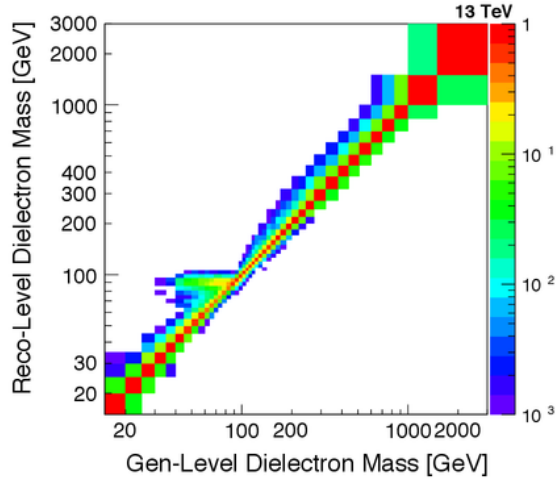


Figure 5.22: The response matrix computed within the detector acceptance from aMC@NLO simulation to unfold the background subtracted yield.

The validity of the unfolding method is first tested on signal MC sample. A ‘closure test’ is performed in which reconstruction-level mass distribution from the simulation is unfolded using the technique discussed above. Fig. 5.23 shows that the resulting unfolded yield from simulation is in perfect agreement with the generator-level mass distribution which confirms the D’Agostini’s iteration procedure used in this analysis.

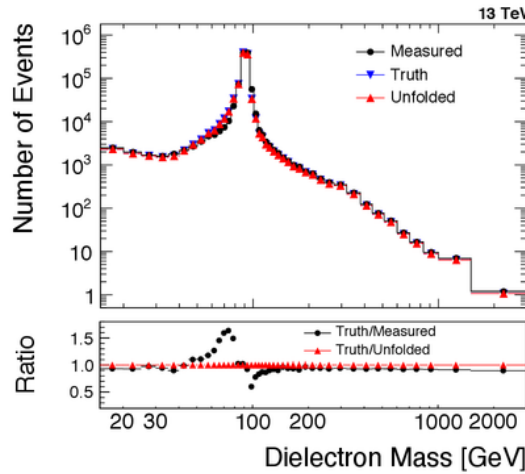


Figure 5.23: Closure test: The comparison of measured (reco-level) distribution and unfolded yield from Monte-Carlo simulation to the true (gen-level) distribution in bins of dielectron invariant mass using D’Agostini’s iteration method with 21 iterations.

After validating the unfolding procedure, the background subtracted yield i.e $(N_{obs} - N_{bkg})$ is corrected for the detector effects using the above obtained response matrix. The largest effect of unfolding can be seen in the 4 Z -peak region $\sim 20\text{-}40\%$ and at high invariant masses.

5.5.2 Acceptance and Efficiency

Due to the detector geometry, some of the particles produced in proton-proton collisions, might remain undetected. There might be few particles which lie within the 114 detector acceptance but do not pass the efficiency 88 selection. In order to compensate for the loss of such particles, 88 acceptance and efficiency corrections are applied.

The detector acceptance ⁴ is defined as the fraction of simulated signal events with both electrons passing the kinematic: $p_T > 30$ (10) GeV for leading (subleading) electrons and geometric: $|\eta| < 2.5$ (excluding the ECAL gap region) requirements.

It is calculated with respect to the full phase space. The efficiency ⁸⁸ is defined as the ⁴ fraction of events in the DY MC sample that are inside the detector acceptance and pass the ¹³³ full event selection of the analysis. Fig. 5.24 shows A , ϵ and $A \times \epsilon$ as a function of dielectron invariant mass. The following equation provides the definition of acceptance and event efficiency discussed above:

$$A \times \epsilon = \frac{N^A}{N^{\text{gen}}} \cdot \frac{N^\epsilon}{N^A} \quad (5.8)$$

⁴ where,

- N^{gen} is the total number of generated signal events in a given invariant mass bin, without any acceptance requirement
- N^A ² is the number of events inside the acceptance
- N^ϵ is the number of events passing the analysis selection

5.5.3 Selection Efficiency

There is a probability that a poorly reconstructed electron gets misidentified at the ³⁵ selection stage. In order to correct for this effect, the reconstruction, identification and trigger selection efficiencies have been computed using a data-driven approach called the tag and probe method [103]. This technique selects those events in which a good electron (tag) passing tight selection criteria and a loosely identified electron (probe) are reconstructed with an invariant mass compatible with a well measured

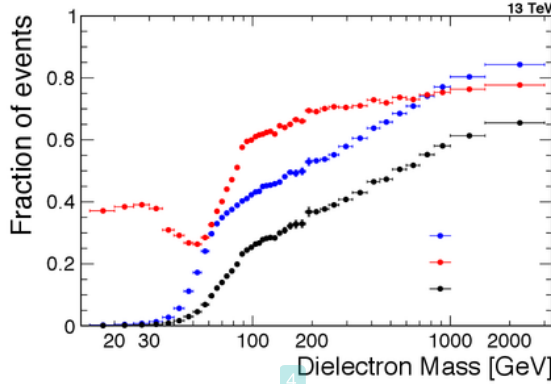


Figure 5.24: Detector acceptance, event efficiency and their product as a function of post-FSR dielectron invariant mass.

¹⁹ Z mass resonance. The efficiency is measured as a function of p_T and η , by counting the number of ‘probe’ as follows:

$$\epsilon(p_T, \eta) = \frac{N_{Pass}^{Probes}}{N_{Pass}^{Probes} + N_{Fail}^{Probes}} \quad (5.9)$$

² where, N_{Pass}^{Probes} is the number probes passing the selection requirement and $N_{Pass}^{Probes} + N_{Fail}^{Probes}$ is the total number of probes. For this analysis, the tag and probe pairs with $60 < M_Z < 120$ GeV mass window are selected to measure the electron efficiency factors in data and simulation. If there exist ³⁴ more than one pair, the one whose invariant mass is closer to Z mass is selected.

In order to determine the number of passing and failing probes, counting or fitting methods can be used. Counting method is applicable when the background is very less, but since the efficiencies here are being computed using a loose Z mass window, there is a possibility of background contamination under the Z -peak and hence proper handling of background becomes important. Therefore, ¹⁵⁵ in order to take into account the effect of background, Fitting method has been used to estimate the efficiency. The details of the functions used to fit the signal and background can be found in [104].

In a Z -peak event, a well reconstructed electron candidate, the tag, passes the trigger and identification requirements while the other candidate, the probe,
154
is required to pass a specific condition, for which the efficiency is being measured
86
in each step. The efficiency is then calculated as the fraction of probe electrons
1
which pass the specified selection criteria to the total number of probe electrons as
described in eq. 5.9. The efficiencies determined from data and MC are divided to
compute the scale factors: $\rho = \epsilon_{data}/\epsilon_{MC}$ which are used to correct the efficiency
difference between data and MC.

21 5.5.3.1 Reconstruction Efficiency

For measuring the reconstruction efficiency, the probe is defined as a supercluster.
66
The invariant mass of the pair is calculated by constructing the four-momentum
of the supercluster by assigning it the mass of an electron. The ‘pass’ condition
is the existence of matched electron in the electron collection without any further
19
requirement on that electron. The efficiency and scale factors as a function of
electron p_T and supercluster η_{sc} can be seen in Fig. 5.25.

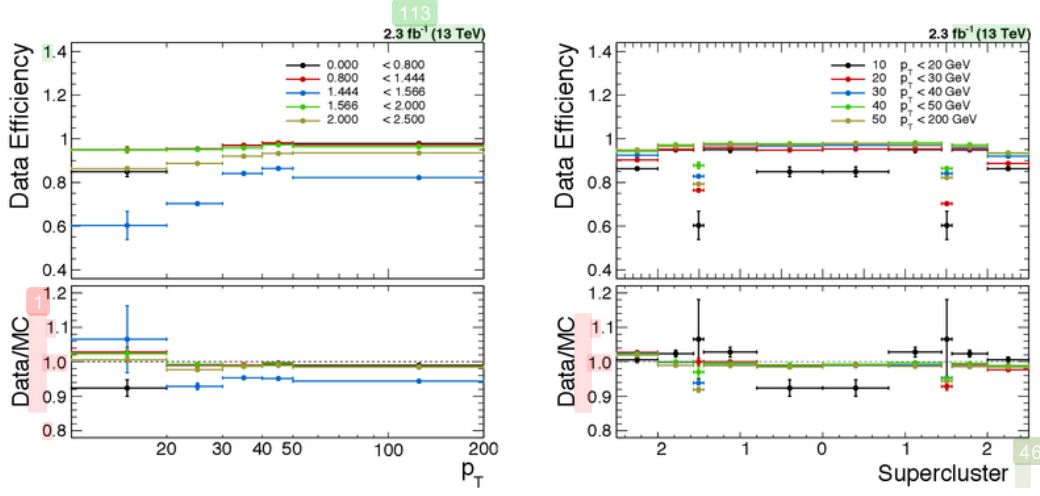


Figure 5.25: Reconstruction Efficiency in data and the corresponding scale factor obtained after dividing the efficiencies for data and Monte-Carlo simulation as a function of p_T (left) and supercluster η_{sc} (right).

86 5.5.3.2 Identification and Isolation Efficiency

The probe is defined as an electron which is present in the default collection of reconstructed electrons after passing the reconstruction algorithm, with no further selection applied. The ‘pass’ sample contains only those electrons which survive the full identification and isolation requirements. Table 5.6 summarizes the selection applied on the tag and probe electron candidates. The ID+Isolation efficiency and the corresponding scale factors obtained from the tag and probe method are shown in Fig. 5.26.

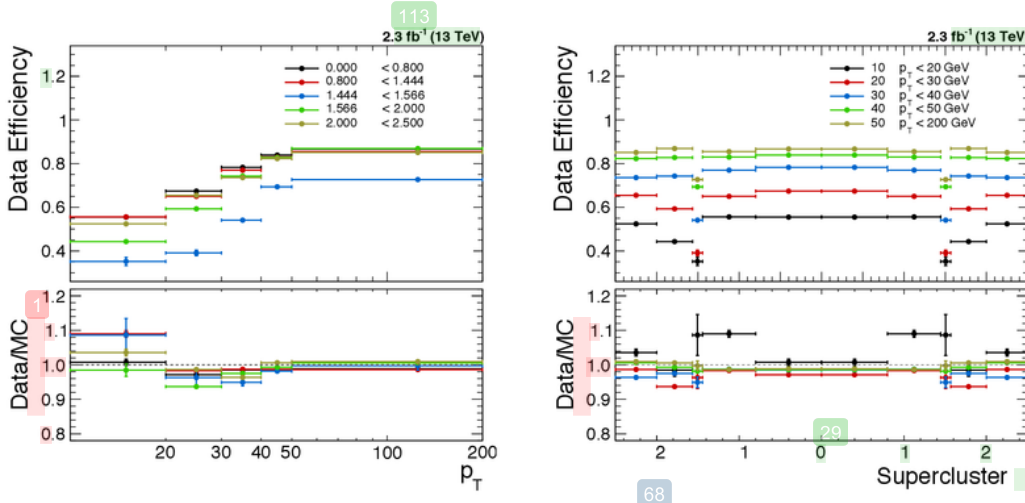


Figure 5.26: Electron Identification and Isolation Efficiency in data and the corresponding scale factor obtained after dividing the efficiencies for data and Monte-Carlo simulation as a function of p_T (left) and supercluster η_{sc} (right).

Selection	Tag	Probe
p_T	> 30 GeV	> 10 GeV
$ \eta_{sc} $	< 2.5	< 2.5
Identification	Tight	Medium
Trigger	<i>HLT_Ele23_WP Loose_Gsf</i>	No trigger applied

Table 5.6: Tag and Probe selection criteria for measuring the Identification and Isolation efficiency.

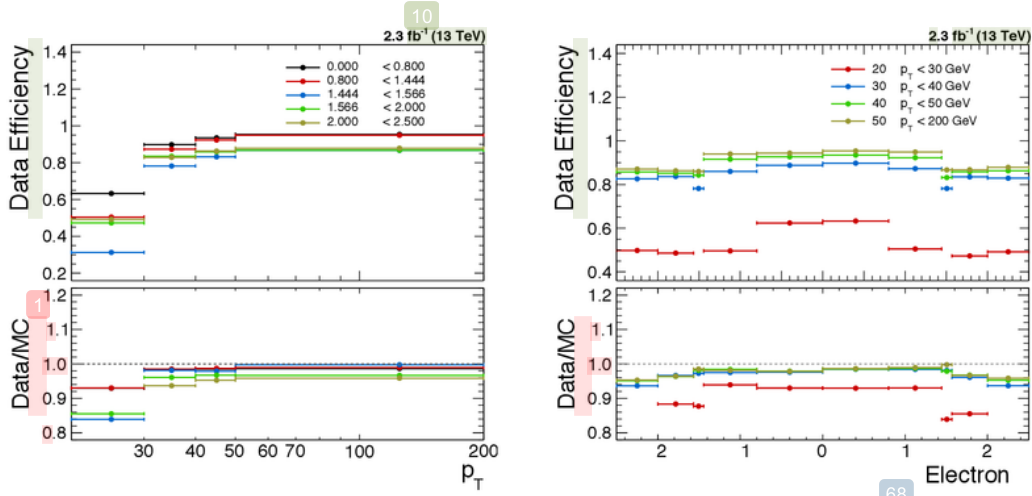


Figure 5.27: HLT Efficiency for the trigger `HLT_Ele23_WPLoose_Gsf` in data and the corresponding scale factor obtained after dividing the efficiencies for data and Monte-Carlo simulation as a function of p_T (left) and electron η (right).

5.5.3.3 Trigger Efficiency

In order to determine HLT efficiency, the probe candidate is required to pass the full electron selection except the condition on ΔR matching between online and offline electron candidates. The probe which then matches the HLT trigger object, is considered to be the ‘passing’ probe. Figure 5.27 shows the trigger efficiency and data/MC scale factors as a function of electron p_T and η .

The total event selection efficiency is factorised into individual efficiencies for each electron in an event which passes a particular selection criteria:

$$\epsilon_{event} = \epsilon_{e1} \cdot \epsilon_{e2} \cdot \epsilon_{event,trig} \quad (5.10)$$

where, ϵ_e is the single electron efficiency defined as:

$$\epsilon_e = \epsilon_{reco} \cdot \epsilon_{id+iso} \quad (5.11)$$

and $\epsilon_{event,trig}$ is the trigger efficiency of the event defined as following:

$$\epsilon_{trig} = 1 - ((1 - \epsilon_{1,trig}) \cdot (1 - \epsilon_{2,trig})) \quad (5.12)$$

5.5.4 Final State Radiation Effects

Electrons can radiate photons in a process referred to as final state electromagnetic radiation (FSR). FSR effect changes the observed invariant mass computed from the four-momenta of the two electrons. If final state photons with sizable energy are emitted, the observed mass can be substantially lower compared to the propagator mass in the hard interaction. This effect is most pronounced just below the Z -peak, where the radiative events in the Z -peak are shifted lower in mass and become significant.

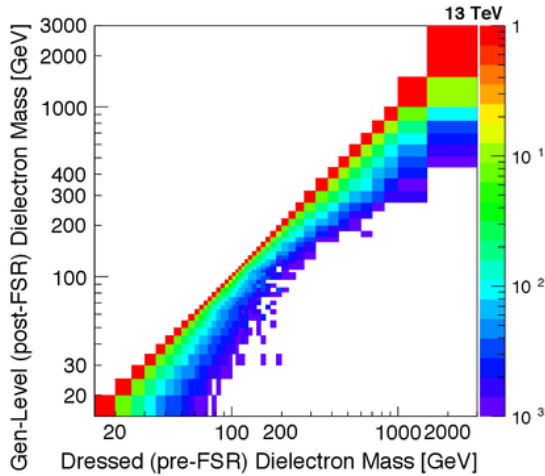


Figure 5.28: The response matrix computed in full phase space from aMC@NLO simulation to correct for the Final State Radiation (FSR) effects using the iterative D'Agostini unfolding method.

The correction for FSR effects is performed by following the unfolding technique as discussed in Section 5.5.1. However, unlikely for detector resolution effect, the unfolding procedure is applied in full phase space using the response matrix derived from pre-FSR and post-FSR yields in signal simulation. In order to obtain the pre-FSR invariant mass without any generator dependent information, a correction procedure known as ‘dressed lepton’ which uses only the post-FSR electrons is

considered. In this procedure, the dressed electron four-momentum is recalculated taking into account the hard photon radiation candidates as described below:

$$p_e^{dressed} = p_e^{post-FSR} + \sum p_\gamma^{FSR} \quad (5.13)$$

where the photon candidates must be inside a cone of radius $\Delta R < 0.1$ around the post-FSR electron candidate. No additional acceptance cuts or requirement on generator information inside the cone is needed.

Unfolding for FSR uses the D'Agostini's iteration method with 21 iteration number as obtained from eq. 5.7. The response matrix and closure test for the unfolding method are shown in Fig. 5.28 and 5.29 respectively. Closure test confirms the validity of the above procedure applied to correct for the radiation effects, showing a perfect agreement between the post-FSR and pre-FSR (dressed) distribution. The level of correction from the post-FSR to dressed definition is found to be between 0.79-1.77 and is dominant below the Z -peak region.

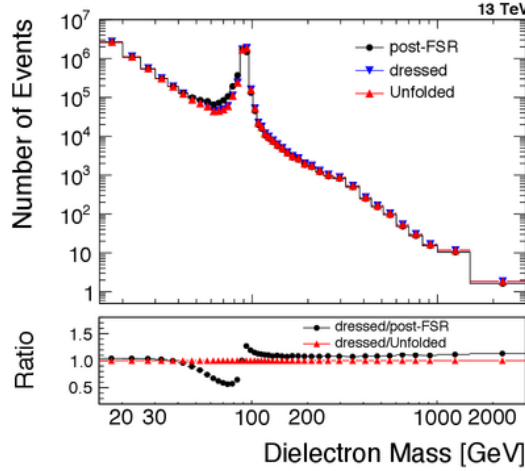


Figure 5.29: Closure test: The comparison of gen-level (post-FSR) invariant mass distribution and FSR corrected unfolded yield from Monte-Carlo simulation to the dressed mass (pre-FSR) distribution in bins of dielectron invariant mass using D'Agostini's iteration method with 21 iterations.

5.6 ²⁸ Systematic Uncertainties

Systematic uncertainties have been evaluated for each step in the determination of dielectron invariant mass spectrum. The various sources of uncertainties are discussed in this section.

5.6.1 Luminosity Uncertainty

⁵ The uncertainty on the luminosity measurement is estimated to be 2.3% [105] for the whole data-taking period in 2015.

5.6.2 ⁶⁴ Statistical Uncertainty

The statistical uncertainty is estimated by randomizing the observed yield distribution (N_{obs}). In order to randomize N_{obs} within its statistical uncertainty, 1000 yield distributions are produced by randomly varying the ⁹⁸ number of events in each mass bin according to Poisson law and calculating the differential cross section corresponding to each randomized yield. Relative difference with the central cross section is calculated and a ‘Gaussian fitting’ is performed for each mass bin. The sigma of ³² the fitted distribution is assigned as the statistical uncertainty corresponding to a mass bin.

⁷ This method takes into account the correlation between bins, which mostly comes from the unfolding procedure used for correcting detector resolution and ³¹ FSR effects. Statistical uncertainty for the differential cross section calculated in ²⁸ full phase space is estimated separately with respect to the uncertainty from dressed-level (pre-FSR) distribution, since the FSR unfolding is not applied in this case and hence the correlation between bins is different.

5.6.3 Scale Correction

The systematic uncertainty from these corrections is determined by scaling the energy and momentum of the electron 100 times within its uncertainty using three different values of sigma, which has two independent components: rho (ρ) and phi (ϕ). Variation in energy and momentum is calculated for $\sigma \pm \rho$ and $\sigma - \phi$ to obtain the measured dielectron distributions. Each distribution ¹ is used to recalculate the response matrix for correcting the detector effects and finally, multiple cross sections are obtained corresponding to each unfolded yield. The maximum standard deviation from the ‘Gaussian fitting’ applied on the relative difference distribution with the central cross section, is assigned as systematic uncertainty for each mass bin.

5.6.4 Background Estimation

The uncertainty for the background estimation is obtained from the Poissonian statistical uncertainty of predicted backgrounds (which is treated as systematic). ²

For the backgrounds estimated from MC and data-driven techniques respectively, the additional source of uncertainty considered is (1) the uncertainty of cross section ²⁵ and (2) the difference between prediction from data and simulation. For the fake electron backgrounds, QCD and $W + jets$, estimated using the fake rate method, the statistical uncertainty on the fake rate ³⁷ is propagated by varying the fake rate within its uncertainty and performing the estimation procedure. The difference with respect to the nominal estimation ³ result is assigned as the systematic uncertainty on each fake background.

After the uncertainties on the background events are obtained, the uncertainty on the differential cross section is estimated. For each background process, 1000 background distributions are obtained by randomizing within the uncertainty of each mass bin. When the uncertainty from statistical component is measured, each

mass bin is randomized independently, while for the uncertainty from systematic component (denoted as (1) and (2) respectively), the mass bins are randomized using same random number for each process. Based on each randomized background distribution, 1000 cross sections are calculated and the variance of cross section with respect to the central value is assigned as the uncertainty from corresponding background process. Finally, the total uncertainty from background estimation is obtained as the quadrature sum of uncertainty from each background process.⁶⁴

5.6.5 Detector Resolution

The uncertainty associated with the unfolding procedure comes primarily from the uncertainty in the unfolding matrix elements due to imperfect simulation of detector resolution.² Instead of calculating the systematic uncertainty specifically on detector resolution unfolding, the cumulative result of resolution effects on all the analysis steps is measured. For this analysis, two kinds of sources are considered (1) Statistical uncertainty on the response matrix due to the finite size of MC sample and (2) Systematic uncertainty on the response matrix from deficiencies in the model. Uncertainty from the first source is estimated by using the diagonal term of a matrix namely ‘covariance matrix’ produced by randomizing the response matrix within the statistical uncertainty of the signal MC sample. Second source of uncertainty is estimated by calculating the unfolding correction using a reweight technique in which the gen-level MC mass spectrum is scaled by the ratio of FEWZ and DY signal mass distributions, to obtain an alternate gen-level distribution and a weighted response matrix which is used to unfold the data distribution. The difference between unfolded yield obtained using the weighted response matrix and the nominal yield¹²² is assigned as the systematic uncertainty associated with the response matrix.

5.6.6 Acceptance Correction

The uncertainty from the acceptance correction contributes to the theoretical uncertainty and is estimated from three kinds of sources:

- The theoretical uncertainty from imperfect knowledge of the non-perturbative PDFs participating in the hard scattering is estimated by FEWZ calculation with NNLO using a reweight technique with LHAGLUE interface to the PDF library LHAPDF as described in [106–108]. The estimation also includes NLO Electroweak (EW) correction and this is compared to LO EW effect to take into account the higher order EW correction
- The factorization and renormalization scales for which theoretical cross section is first calculated using the reference value of the coupling constant (0.118) and then with 0.117 and 0.119. The deviation of the cross section with the reference value is assigned as the theoretical uncertainty. Effect of the scale variation on the cross section is very small, which is about 1-2% level
- The difference between aMC@NLO and Next-to-next-to-leading order (NNLO) which is taken into account by assigning the acceptance difference between aMC@NLO and NNLO prediction (calculated by FEWZ).

5.6.7 Efficiency Correction

The uncertainty from efficiency scale factor correction is an important source and reflects systematic deviations that vary up to 12% between data and simulation. As discussed in Section 5.5.3, single electron efficiencies of several types are measured with the tag and probe technique and are combined into event efficiency scale factors. This procedure determines the efficiency and an associated statistical uncertainty. A variety of possible systematic biases from the tag and probe procedure which can effect the electron efficiencies, such as dependence on the assumed shape of signal and

background in the fit model, variation in tag selection, and others are studied and an appropriate systematic uncertainty to the single electron efficiency scale factors is assigned. The effect of the combined statistical and systematic uncertainties from the event scale factors on the cross section constitutes the final systematic uncertainty from this source. The different sources of efficiency correction systematic uncertainty are discussed below.

- *Uncertainty in line shape modeling:* This uncertainty is estimated by performing the signal and background fitting using alternate fit functions. We compare the efficiencies extracted with two signal hypotheses: (1) Monte-Carlo templates smeared with Gaussian and (2) Crystal Ball fit function. For the background, (1) CMSShape and (2) Exponential fit functions are compared.
- *Uncertainty from Monte-Carlo simulation:* This uncertainty is estimated by comparing the efficiencies calculated from two different signal samples. We use (1) Next-to-leading order (NLO) and (2) Leading-order (LO) MC samples to determine the different efficiencies of each type in order to evaluate the systematic uncertainty. The effect of this uncertainty is minimal and is covered by the larger statistical uncertainty.
- *Uncertainty from other sources in tag and probe method:* In the efficiency measurement using tag and probe method, a selection criteria for the kinematic and identification requirements is applied on the ‘tag’. To estimate the systematic uncertainty from the variation in selection parameters, the efficiencies are recalculated after changing the value of each parameter. Difference of the efficiency value for each $p_T - \eta$ bin with the central value is assigned as the systematic uncertainty. The contribution to the total uncertainty from this source is found to be small.

These uncertainties are evaluated by recomputing the cross section multiple times using an ensemble of the single electron efficiency maps where the entries are

² modified randomly within ± 1 standard deviation of uncertainties in $p_T\text{-}\eta$ bins. When the uncertainty from statistical efficiency is considered, each $p_T\text{-}\eta$ bin is randomized independently. However, when the uncertainty from systematic uncertainty of tag and probe efficiency is estimated, all $p_T\text{-}\eta$ bins are randomized in the same direction and magnitude for each efficiency map in order to move them coherently. We consider 500 efficiency correction maps obtained with the map variation technique to calculate the efficiency corrections, which are applied as weights per electron, to determine multiple final differential cross sections. The sigma of the spread of these cross sections is obtained by Gaussian fitting per mass bin which ¹ is used as an estimate of systematic uncertainty in each mass bin. The uncertainty from efficiency correction factors is evaluated to be up to 12% with respect to the dielectron invariant mass.

5.6.8 FSR Correction

Uncertainty from the unfolding procedure for FSR correction is considered from two sources: (1) Statistical uncertainty on the response matrix due to the finite size of MC sample and (2) Uncertainty from model dependence of FSR correction. The uncertainty from first source is estimated by following the same procedure as described for ‘detector resolution’ and the second source of uncertainty is obtained by comparison with different FSR simulation using PHOTOS [109, 110] generator and assinging the variation of the FSR corrected results as the uncertainty.

5.6.9 Total Uncertainty

After the estimation of uncertainties from all possible sources, the systematic uncertainties from the background estimation, detector resolution and FSR corrections are smoothed to reduce bin by bin fluctuations. The total systematic uncertainty is obtained by taking the quadrature sum of individual uncertainties described in Section 5.6.2 - 5.6.8. The systematic uncertainties from scale corrections and detector

resolution are combined since both of these effect the unfolded yield distribution.

¹²⁷
The effect of uncertainties on the differential cross section measurement is shown in Fig. 5.30 and exact values of different systematic uncertainties are summarized in Appendix A.1.

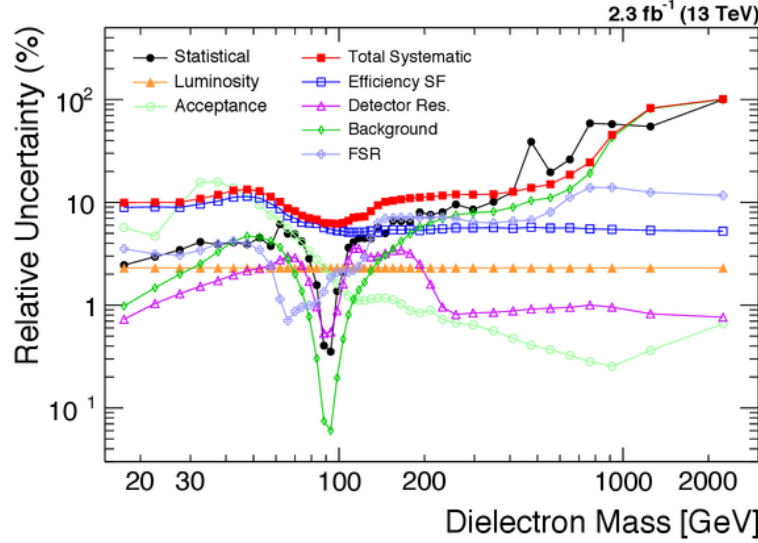


Figure 5.30: The statistical, luminosity, acceptance and the total systematic (quadrature sum of efficiency scale factor (SF), detector resolution, background and FSR correction) uncertainties obtained in the bins of dielectron invariant mass.

Chapter 6

Results

1 The Drell-Yan cross section measurement is performed after correcting for various effects discussed in the previous chapter. The cross section is measured 4 in the Z -peak region ($60 < m < 120$ GeV) as well as 51 in the bins of dilepton invariant mass, within the range $15 < m < 3000$ GeV. The measurement results are discussed in the following sections.

6.1 Z -peak Cross section Measurement

4 The Z boson production cross section in the Z -peak region ($60 < m < 120$ GeV) is calculated as following:

$$\sigma_Z = \frac{1}{\mathcal{L}} \left\{ \frac{N_u^{\text{norm}}}{A^{\text{norm}} \cdot \epsilon^{\text{norm}} \cdot \rho} \right\} \quad (6.1)$$

2 where, N_u^{norm} is the number of events after performing background subtraction and unfolding procedure for the detector resolution and FSR correction, A^{norm} and ϵ^{norm} are the acceptance and efficiency correction factors 2 in the Z -peak region, ρ is efficiency scale factor and \mathcal{L} is the total integrated luminosity.

The absolute cross section measurement in the electron final state for full

¹⁰⁸ phase space and within the detector acceptance is summarized in Table 6.1. The measured cross section is ² in good agreement with NNLO predictions for the full phase space (a typical NNLO prediction is 1870^{+50}_{-40} pb) and also with the previous CMS measurement [111].

Measurement	Cross section in Z -peak region
Full Phase Space	$1949 \pm 2(\text{stat.}) \pm 96(\text{exp. syst.}) \pm 47(\text{th. syst.}) \pm 45(\text{lum.})$ pb
Fiducial	$760 \pm 1(\text{stat.}) \pm 38(\text{exp. syst.}) \pm 17(\text{lum.})$ pb

Table 6.1: Absolute cross section measurements ¹ in full phase space and fiducial region (within the detector acceptance) for the Z -peak region ($60 < m < 120$ GeV) with associated uncertainties.

⁹⁷ 6.2 Differential Cross section Measurement

The cross scetion measurement in the bins of dielectron invariant mass is an important measurement performed in this analysis:

$$\sigma^i = \frac{N_u^i}{A^i \cdot \epsilon^i \cdot \rho^i \cdot \mathcal{L}} \quad (6.2)$$

where, each quantity is calculated in a given invariant mass bin i . The result ⁴ in each bin is divided by the corresponding invariant mass bin width, Δm^i , defining the shape $\sigma^i/\Delta m^i$.

³ The DY differential cross section is measured in the full phase space after applying ⁸ a set of corrections discussed in the previous chapter. The cross section measurement is performed in the bins of dielectron invariant mass ¹⁵³ and presented in Fig. 6.1. The results are compared to the NNLO theoretical prediction which is calculated using FEWZ 3.1 including the NLO EW correction and the NLO MADGRAPH_AMC@NLO. These predictions are calculated with NNPDF3.0 PDF set. The ratio between experimental data and theory can be seen in the middle and

bottom plots in which the colored bands represent theoretical uncertainty while the shaded band represent the total uncertainty which is the combination of statistical, systematic and luminosity uncertainties added in quadrature. The detailed numbers for the central value of the cross section and uncertainties are available in Table A.2. The results are found to be in good agreement with both theoretical predictions within the uncertainties.

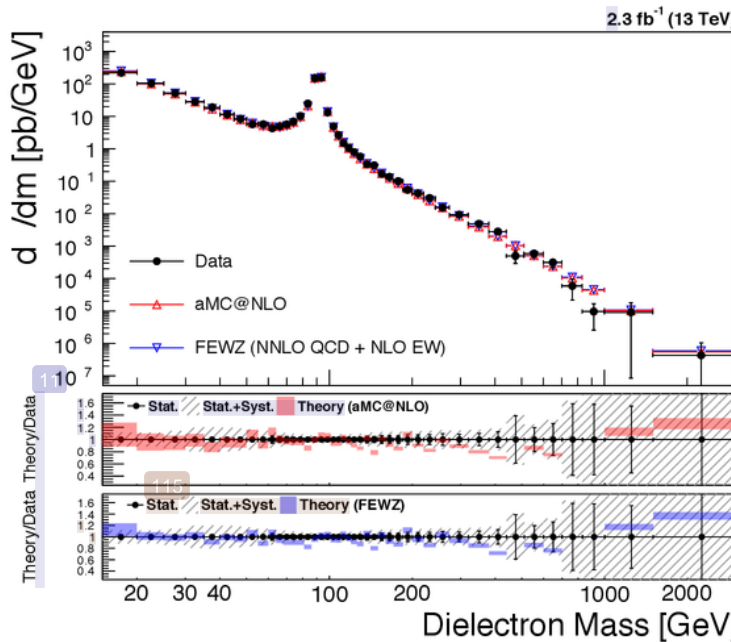


Figure 6.1: The Drell-Yan differential cross section measurement corrected for radiation effects in full phase space as a function of dielectron invariant mass compared to the NNLO theoretical prediction from FEWZ (blue) and the NLO prediction MADGRAPH_aMC@NLO (red). The coloured band in the middle and bottom plots denotes theoretical uncertainty and the shaded band denotes the total uncertainty which is the combination of statistical, systematic and luminosity uncertainties. The error bar on the data points denote the statistical uncertainty only.

The differential cross section in the fiducial region, defined by the p_T and η requirements for the electrons after the radiation effects have taken place, is also calculated in addition to the fully corrected DY cross section measurement. The fiducial cross section measurement is performed within the detector acceptance which minimizes the effect of acceptance as well as the FSR correction. The fiducial results

are presented in Fig. 6.2 which shows the comparison of experimental data with the NLO theoretical prediction from MADGRAPH_AMC@NLO. The results are in good agreement with the prediction. The detailed numbers for the central value of the fiducial cross section and uncertainties are shown in Table A.3.

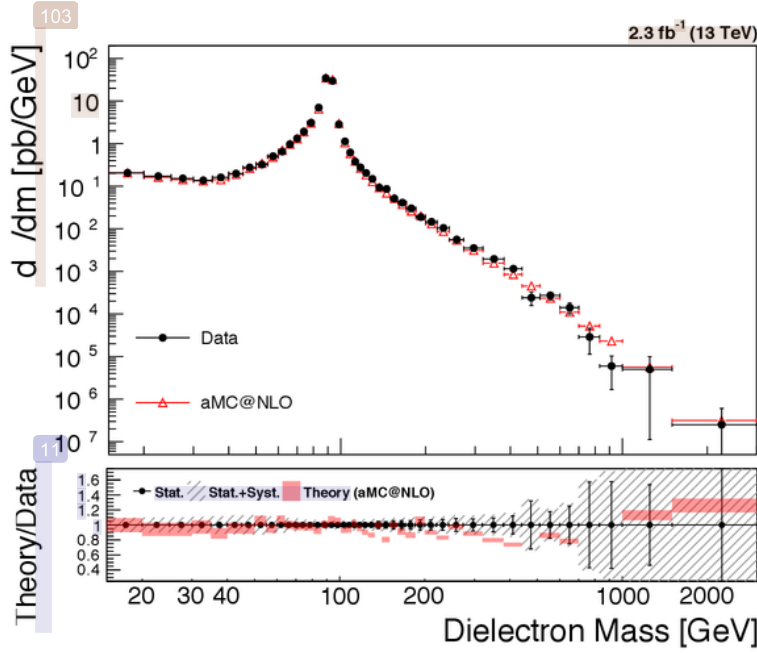
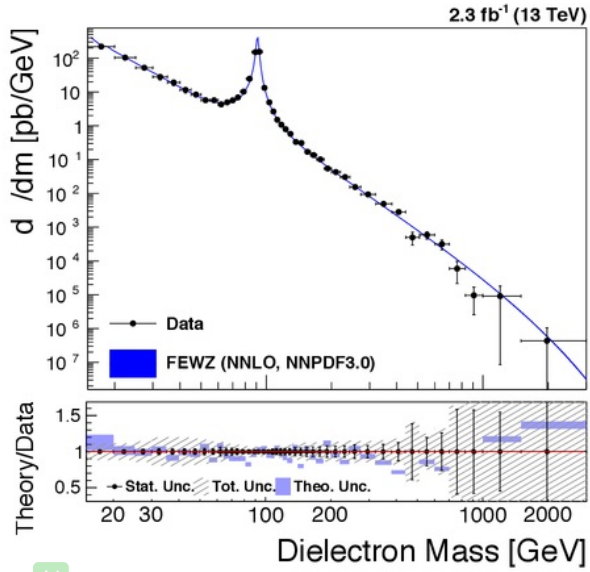
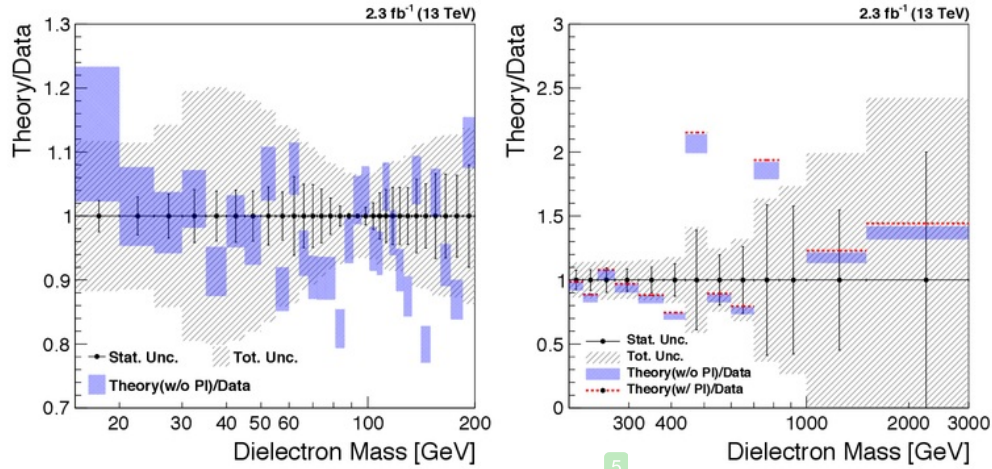


Figure 6.2: The Drell-Yan differential cross section measurement performed in the fiducial region without FSR correction as a function of dielectron invariant mass compared to the NLO theoretical prediction from MADGRAPH_AMC@NLO. The red band in the bottom plot denotes theoretical uncertainty and the shaded band denotes the total uncertainty which is the combination of statistical, systematic and luminosity uncertainties. The error bar on the data points denote the statistical uncertainty only.

The experimental result is compared to the NNLO theoretical prediction calculated from FEWZ in which the data x-coordinate is computed as explained in [112].
 The ratio between data and theoretical prediction in the mass range $m < 200$ GeV and $200 < m < 3000$ GeV is presented in the left and right plots, respectively in the Fig. 6.4. The blue band in these plots represent the theoretical uncertainty. The right plot additionally includes the contribution from Photon Induced (PI) backgrounds which is estimated by FEWZ 3.1 with MRST2004qed PDF set.



41
Figure 6.3: The Drell-Yan differential cross section measurement performed as a function of dielectron invariant mass compared to the NNLO theoretical prediction from FEWZ for the full phase space. The data point abscissas are obtained according to eq. (6) in [112]. The bottom plot shows the ratio between data and theoretical prediction where the coloured box denotes theoretical uncertainty.



5
Figure 6.4: Ratio of theory to experimental data for the differential cross section as a function of dielectron invariant mass in the range $m < 200$ GeV (left) and $m > 200$ GeV (right). The blue band denotes the theoretical uncertainty on the ratio. In the right plot, the contribution from Photon Induced backgrounds is shown in red colour and has a visible effect in the high mass region.

In order to check the dependence of PDFs in the high mass region ($m > 200$ GeV), FEWZ calculation is obtained using various PDF sets. Figure 6.5 shows the ratio of theoretical prediction from various PDFs and the experimental data above 200 GeV. It can be seen that, all the theoretical predictions are consistent amongst themselves as well as in agreement with the measured result within the uncertainties.

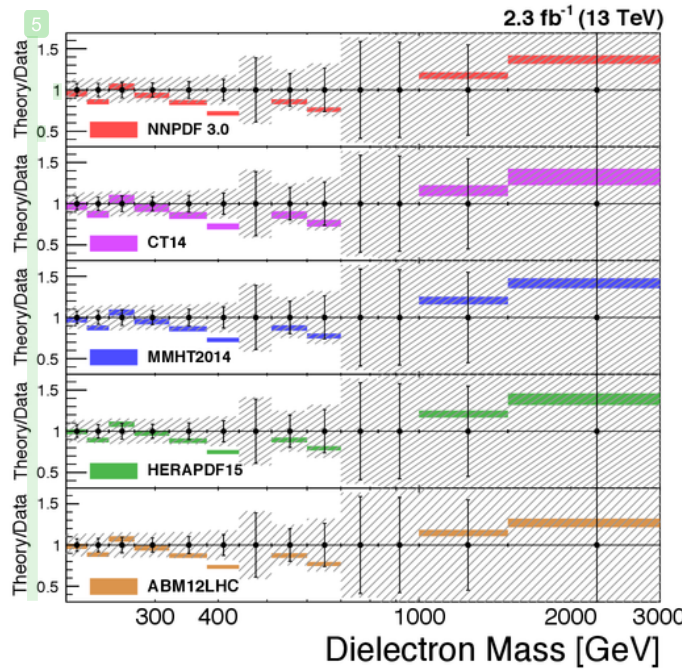


Figure 6.5: Ratio between experimental result and theoretical prediction from various PDFs for $m > 200$ GeV. The coloured band in the plot denotes the theoretical uncertainty and the shaded band denotes the total experimental uncertainty excluding the luminosity uncertainty. The error bar on the data points denote the statistical uncertainty only.

The measurement of the Drell-Yan differential cross section has already been performed in the muon final state [5] using the collision data collected by the CMS experiment at a center-of-mass energy $\sqrt{s} = 13$ TeV, corresponding to an integrated luminosity of 2.8 fb^{-1} . The differential cross section measurement obtained in the dielectron and dimuon channels are found to be in good agreement with each other and therefore, the results in the electron and muon final states are combined for a greater precision, using the technique known as ‘Best Linear Unbiased Estimate’

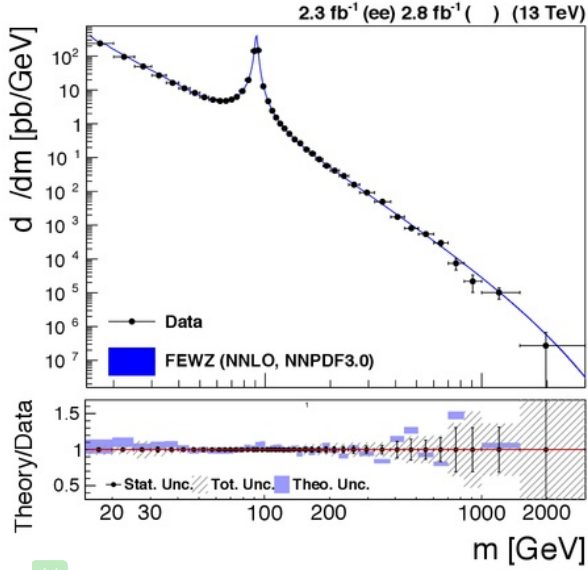
(BLUE) method [113]. The combined estimate of the measured quantities obtained using the BLUE method takes into account all the correlations by considering the covariance matrix of the input data, which may arise due to the use of same data from the same experiment or even the same theoretical models.

In the current analysis, all the uncertainties are considered to be uncorrelated between the two channels, with an exception to the luminosity uncertainty and the systematic uncertainty from acceptance correction. The acceptance uncertainty is treated as correlated, since in each channel this uncertainty is based on theoretical calculations which use same PDF (NNPDF 3.0) set.

The correlation between the mass bins is however, treated differently for each type of uncertainty discussed in Sec 5.6, while constructing the covariance matrix. The statistical uncertainty on the measured yield is considered as correlated between the mass bins. The systematic uncertainty, arising from the limitation of data or MC statistics is regarded as the uncertainty from statistical source and hence, considered to be correlated. The systematic uncertainties which are estimated by comparing different MC models, are assumed to be uncorrelated between the mass bins.

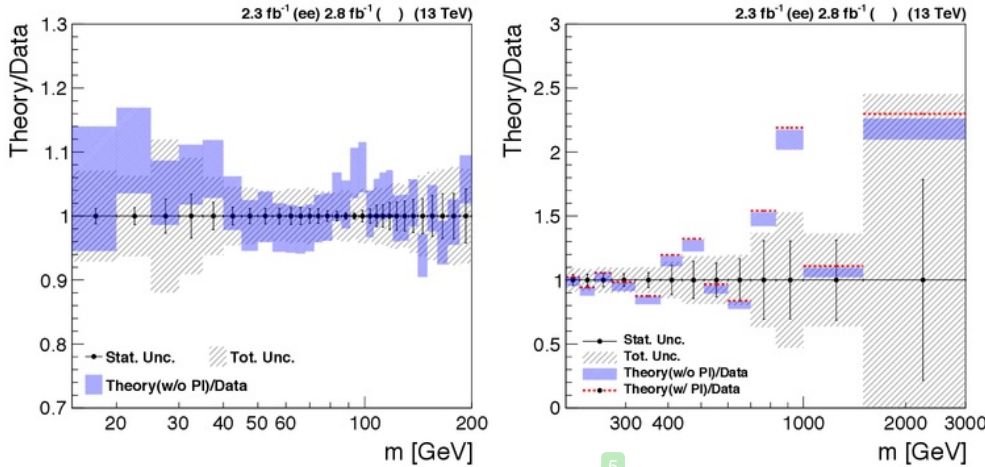
The result of the Drell-Yan cross section measurement in the combined channel is presented in Fig. 6.6 and compared to the theoretical prediction which uses the fixed-order NNLO QCD calculation and NLO EW correction to the Drell-Yan production. The detailed numbers for the differential cross section in the combined channel are available in Table A.4. Figure 6.7 shows the ratio between data and theoretical prediction in the mass range $m < 200$ GeV and $200 < m < 3000$ GeV. The result in the combined channel is found to be in agreement with the NNLO theoretical predictions.

In order to check the dependence of PDFs in the high mass region ($m > 200$ GeV), FEWZ calculation is obtained using various PDF sets. Figure 6.8 shows the ratio of theoretical prediction from various PDFs and the experimental data above 200 GeV. It can be seen that, all the theoretical predictions are consistent amongst



41

Figure 6.6: The Drell-Yan differential cross section measurement performed as a function of dielectron invariant mass compared to the NNLO theoretical prediction from FEWZ for the full phase space. The data point abscissas are obtained according to eq. (6) in [112]. The bottom plot shows the ratio between data and theoretical prediction where the coloured box denotes theoretical uncertainty.



5

Figure 6.7: Ratio of theory to experimental data for the differential cross section as a function of dielectron invariant mass in the range $m < 200$ GeV (left) and $m > 200$ GeV (right). The blue band denotes the theoretical uncertainty on the ratio. In the right plot, the contribution from Photon Induced backgrounds is shown in red colour and has a visible effect in the high mass region.

51
themselves as well as in agreement with the measured result within the uncertainties.

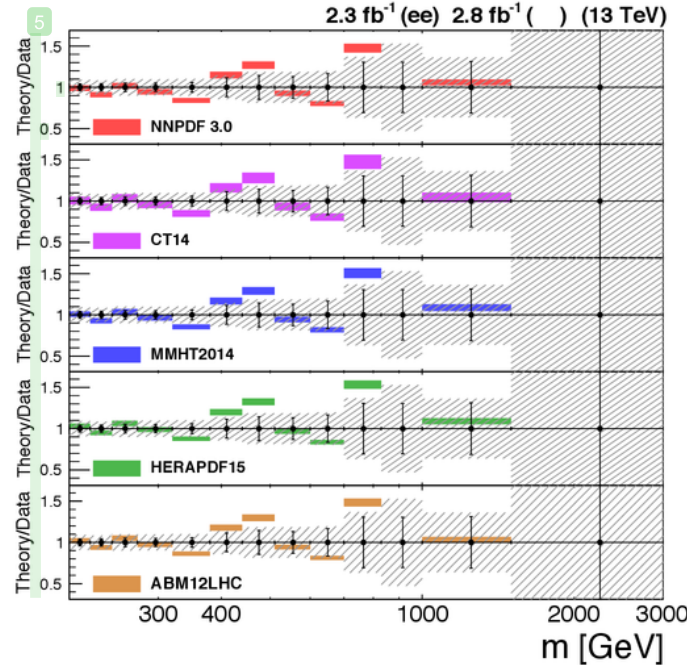


Figure 6.8: Ratio between experimental result and theoretical prediction from various PDFs for $m > 200$ GeV. The coloured band in the plot denotes the theoretical uncertainty and the shaded band denotes the total experimental uncertainty excluding the luminosity uncertainty. The error bar on the data points denote the statistical uncertainty only.

Chapter 7

Summary

In this thesis work, the Drell-Yan differential cross section $d\sigma/dm$ measurement is performed using the proton-proton collision data collected with the CMS experiment during the year 2015 corresponding to an integrated luminosity of 2.3 fb^{-1} . The cross section is measured in the electron final state over a wide range of dielectron invariant mass ($15 < m < 3000 \text{ GeV}$). Signal events are characterized by the presence of two electrons consistent with the Z boson decay. There are various background processes which can mimic the signal and contribute to the final state depending on the dielectron mass region. The dominant background processes in the entire mass range are $t\bar{t}$ along with single-top, while $DY \rightarrow \tau\tau$ contributes in the low mass, below the Z -peak region. Other sub-dominant background processes include WW , WZ , ZZ and $W + jets$ and the QCD hadronic decay which contributes mainly in the high mass region. To reduce the contamination from these background processes, events triggered with a single electron trigger having a minimum threshold on the transverse momentum (p_T) are selected and a kinematical requirement based on the p_T of leading and sub-leading electrons is applied. The electrons which get misreconstructed and misidentified (jet faking as an electron) in the detector acceptance are rejected by applying an efficient and effective identification criteria and a requirement to pass the particle flow isolation, with a rejection efficiency of

85%. The efficiencies for the trigger selection, reconstruction and identification of electrons is computed using a data-driven approach the ‘tag and probe method’. The measured efficiencies obtained from data are in good agreement with the Monte-carlo simulations.

Although, the background contribution obtained from Monte-Carlo prediction is found to be reliable, the main backgrounds are estimated using data-driven control samples. The electroweak processes namely $t\bar{t}$, single-top (tW and $\bar{t}W$), DY production of $\tau\tau$ pairs and diboson (WW) are estimated from the $e\mu$ control sample, based on the reconstruction of $e\mu$ pair normalized to e^+e^- final state. The e^+e^- background events estimated from data corresponds to a total of 26629 ± 163 and is in good agreement with 27605 ± 166 events predicted by Monte-carlo simulation. The QCD and $W + jets$, with at least one misidentified electron are estimated by measuring the probability of a jet to fake an electron using a sample dominated by jets. The fake rate which is found to vary up to 0.5%, is applied two different control samples prepared from electrons, passing or failing the selection criteria used in the analysis. The other remaining backgrounds WZ and ZZ with only a small contribution to the dielectron mass spectrum, are estimated from Monte-Carlo predictions.

The Z boson production cross section in the peak region ($60 < m < 120$ GeV) and the differential cross section ($d\sigma/dm$) in the bins of dielectron invariant mass ($15 < m < 3000$ GeV) is obtained from the experimental data in the full phase space and the fiducial region, which is calculated within the detector acceptance. The measurement is corrected for limited detector resolution causing migration of events between mass bins, acceptance to take into account the coverage of CMS detector, difference in reconstruction, identification and trigger efficiencies between data and Monte-Carlo simulation and the final state radiation effects where the radiating photons can lead to smaller observed mass compared to pre-FSR mass, mainly below the Z -peak region. The absolute Z -peak cross section in full phase space is

found to be 1949 ± 2 (stat.) ± 96 (exp. syst.) ± 47 (th. syst.) ± 45 (lum.) and
is consistent with the theory predictions. The differential cross section measurement
is compared bin-by-bin with the Standard Model theoretical predictions at
(1) the next-to-next-to-leading order (NNLO) prediction calculated with FEWZ 3.1
using NNLO NNPDF3.0 parton distribution function and (2) the next-to-leading
order (NLO) prediction calculated with MADGRAPH5_AMC@NLO. The corrected
experimental results are found to be in good agreement with the theoretical predictions.

The measurement of the differential cross section from the experimental data,
can allow for a more precise determination of parton distribution functions and a
better understanding of their uncertainties, which is essential to make predictions
for physical cross sections.

The study performed in this analysis leads to a confirmation of the predictions
associated with the Standard Model. It is of utmost importance for building new
models related to the physics of dark matter particles, incorporate the full theory
of gravitation, unification of strong and electroweak forces and other studies which
go beyond the Standard Model predictions.

Appendix A

³¹
**A.1 Summary of the systematic uncertainties for
 $d\sigma/dm$ measurement**

m (GeV)	Scale (%)	Eff. SF (ρ) (%)	Det. Res. (%)	Bkg. Est. (%)	FSR (%)	Total (%)	Acc. (%)
15-20	0.72	8.92	0.12	0.98	3.54	9.67	5.69
20-25	1.01	9.03	0.22	1.47	3.14	9.73	4.71
25-30	1.25	8.93	0.31	1.99	3.07	9.74	9.52
30-35	1.47	9.62	0.42	2.52	3.42	10.63	15.65
35-40	1.64	10.27	0.56	3.31	3.95	11.61	15.78
40-45	1.86	11.22	0.64	4.19	4.20	12.84	13.81
45-50	2.10	11.43	0.51	4.67	3.99	13.16	11.51
50-55	2.25	11.05	0.27	4.59	3.47	12.64	9.39
55-60	2.45	9.69	0.19	4.21	2.41	11.11	7.57
60-64	2.73	8.66	0.41	3.66	1.15	9.87	6.68
64-68	2.87	7.39	0.77	2.80	0.71	8.48	5.59
68-72	2.72	7.01	0.98	1.99	0.87	7.89	4.74
72-76	2.28	6.40	0.89	1.37	0.96	7.05	4.04
76-81	1.59	6.31	0.61	0.77	0.99	6.65	3.39
81-86	0.88	6.23	0.39	0.30	1.05	6.39	2.79
86-91	0.43	5.68	0.31	0.07	1.35	5.87	2.31
91-96	0.41	5.47	0.36	0.06	1.85	5.81	1.93
96-101	0.73	5.30	0.49	0.19	2.09	5.77	1.61
101-106	1.50	5.23	0.57	0.47	2.08	5.87	1.37
106-110	2.70	5.11	0.51	0.81	2.09	6.22	1.23
110-115	3.56	5.13	0.37	1.14	2.18	6.72	1.13
115-120	3.55	5.15	0.26	1.41	2.38	6.84	1.11
120-126	3.14	5.14	0.25	1.67	2.94	6.91	1.11
126-133	2.93	5.29	0.29	2.15	4.56	7.87	1.14
133-141	2.99	5.11	0.33	2.69	6.32	9.08	1.17
141-150	3.17	5.37	0.36	3.06	6.96	9.84	1.17
150-160	3.37	5.41	0.36	3.54	7.05	10.15	1.13
160-171	3.42	5.39	0.29	4.18	7.12	10.44	1.02
171-185	3.18	5.47	0.20	4.92	7.12	10.73	0.88
185-200	2.51	5.32	0.16	5.77	7.12	10.89	0.84
200-220	1.59	5.44	0.16	6.35	7.13	11.10	0.89
220-243	0.93	5.52	0.21	6.89	7.16	11.41	0.73
243-273	0.75	5.64	0.32	7.55	6.94	11.73	0.67

m (GeV)	Scale (%)	Eff. SF (ρ) (%)	Det. Res. (%)	Bkg. Est. (%)	FSR (%)	Total (%)	Acc. (%)
273-320	0.76	5.64	0.36	7.92	6.44	11.69	0.64
320-380	0.77	5.68	0.36	8.13	6.29	11.78	0.56
380-440	0.80	5.58	0.36	8.95	6.57	12.46	0.48
440-510	0.84	5.72	0.36	10.38	6.73	13.66	0.41
510-600	0.86	5.63	0.36	11.09	8.04	14.84	0.37
600-700	0.86	5.65	0.41	13.46	11.21	18.43	0.32
700-830	0.86	5.52	0.51	19.25	13.87	24.39	0.28
830-1000	0.77	5.45	0.57	42.63	14.01	45.21	0.25
1000-1500	0.59	5.34	0.57	81.43	12.52	82.57	0.36
1500-3000	0.51	5.24	0.57	100.29	11.68	101.11	0.65

Table A.1: Summary of the systematic uncertainties for the differential cross section $d\sigma/dm$ measurement. ‘Total’ refers to the quadratic sum of all sources of uncertainties except for the uncertainty from acceptance correction.

A.2 ² Summary of the results for full phase space $d\sigma/dm$ measurement in dielectron channel

m (GeV)	Central value (pb/GeV)	Stat. Unc. (pb/GeV)	Exp. Unc. (pb/GeV)	Theo. Unc. (pb/GeV)	Total Unc. (pb/GeV)
15-20	2.2×10^2	5.4×10^0	2.2×10^1	1.3×10^1	2.6×10^1
20-25	1.0×10^2	3.1×10^0	1.0×10^1	4.9×10^0	1.2×10^1
25-30	5.2×10^1	1.8×10^0	5.2×10^0	4.9×10^0	7.4×10^0
30-35	2.8×10^1	1.2×10^0	3.0×10^0	4.4×10^0	5.4×10^0
35-40	1.9×10^1	7.4×10^{-1}	2.3×10^0	3.0×10^0	3.8×10^0
40-45	1.2×10^1	4.7×10^{-1}	1.5×10^0	1.6×10^0	2.2×10^0
45-50	8.4×10^0	3.3×10^{-1}	1.1×10^0	9.6×10^{-1}	1.5×10^0
50-55	5.7×10^0	2.6×10^{-1}	7.1×10^{-1}	5.4×10^{-1}	9.3×10^{-1}
55-60	5.7×10^0	2.1×10^{-1}	6.5×10^{-1}	4.3×10^{-1}	8.0×10^{-1}
60-64	4.3×10^0	2.6×10^{-1}	4.4×10^{-1}	2.9×10^{-1}	5.9×10^{-1}
64-68	4.9×10^0	2.4×10^{-1}	4.4×10^{-1}	2.8×10^{-1}	5.7×10^{-1}
68-72	5.7×10^0	2.8×10^{-1}	4.6×10^{-1}	2.7×10^{-1}	6.0×10^{-1}
72-76	6.9×10^0	2.9×10^{-1}	5.1×10^{-1}	2.8×10^{-1}	6.5×10^{-1}
76-81	1.0×10^1	2.9×10^{-1}	7.2×10^{-1}	3.5×10^{-1}	8.5×10^{-1}
81-86	2.5×10^1	3.9×10^{-1}	1.7×10^0	6.9×10^{-1}	1.9×10^0
86-91	1.5×10^2	6.1×10^{-1}	9.5×10^0	3.5×10^0	1.0×10^1
91-96	1.5×10^2	5.5×10^{-1}	9.7×10^0	2.9×10^0	1.0×10^1
96-101	1.3×10^1	1.8×10^{-1}	8.2×10^{-1}	2.1×10^{-1}	8.7×10^{-1}
101-106	4.9×10^0	1.0×10^{-1}	3.1×10^{-1}	6.7×10^{-2}	3.3×10^{-1}
106-110	2.6×10^0	9.6×10^{-2}	1.8×10^{-1}	3.3×10^{-2}	2.0×10^{-1}
110-115	1.5×10^0	6.2×10^{-2}	1.1×10^{-1}	1.7×10^{-2}	1.2×10^{-1}
115-120	1.1×10^0	4.8×10^{-2}	7.7×10^{-2}	1.2×10^{-2}	9.2×10^{-2}
120-126	7.9×10^{-1}	3.5×10^{-2}	5.8×10^{-2}	8.8×10^{-3}	6.8×10^{-2}
126-133	5.7×10^{-1}	2.5×10^{-2}	4.7×10^{-2}	6.5×10^{-3}	5.4×10^{-2}
133-141	3.3×10^{-1}	1.9×10^{-2}	3.1×10^{-2}	3.9×10^{-3}	3.7×10^{-2}
141-150	3.1×10^{-1}	1.5×10^{-2}	3.1×10^{-2}	3.6×10^{-3}	3.5×10^{-2}
150-160	1.7×10^{-1}	1.1×10^{-2}	1.8×10^{-2}	1.9×10^{-3}	2.1×10^{-2}
160-171	1.4×10^{-1}	8.9×10^{-3}	1.5×10^{-2}	1.3×10^{-3}	1.7×10^{-2}
171-185	1.0×10^{-1}	6.5×10^{-3}	1.1×10^{-2}	8.9×10^{-4}	1.3×10^{-2}
185-200	5.4×10^{-2}	4.4×10^{-3}	6.0×10^{-3}	4.5×10^{-4}	7.5×10^{-3}
200-220	4.3×10^{-2}	3.2×10^{-3}	4.8×10^{-3}	3.8×10^{-4}	5.8×10^{-3}

m (GeV)	Central value (pb/GeV)	Stat. Unc. (pb/GeV)	Exp. Unc. (pb/GeV)	Theo. Unc. (pb/GeV)	Total Unc. (pb/GeV)
220-243	3.0×10^{-2}	2.4×10^{-3}	3.5×10^{-3}	2.2×10^{-4}	4.3×10^{-3}
243-273	1.5×10^{-2}	1.5×10^{-3}	1.8×10^{-3}	1.0×10^{-4}	2.4×10^{-3}
273-320	9.3×10^{-3}	7.9×10^{-4}	1.1×10^{-3}	5.9×10^{-5}	1.3×10^{-3}
320-380	4.9×10^{-3}	4.9×10^{-4}	5.9×10^{-4}	2.7×10^{-5}	7.7×10^{-4}
380-440	2.8×10^{-3}	3.6×10^{-4}	3.6×10^{-4}	1.3×10^{-5}	5.0×10^{-4}
440-510	4.9×10^{-4}	1.9×10^{-4}	6.9×10^{-5}	2.0×10^{-6}	2.1×10^{-4}
510-600	5.9×10^{-4}	1.2×10^{-4}	8.8×10^{-5}	2.2×10^{-6}	1.4×10^{-4}
600-700	3.1×10^{-4}	8.2×10^{-5}	5.8×10^{-5}	1.0×10^{-6}	1.0×10^{-4}
700-830	5.9×10^{-5}	3.4×10^{-5}	1.5×10^{-5}	1.7×10^{-7}	3.8×10^{-5}
830-1000	9.6×10^{-6}	5.7×10^{-6}	4.4×10^{-6}	2.5×10^{-8}	7.1×10^{-6}
1000-1500	9.1×10^{-6}	4.9×10^{-6}	7.5×10^{-6}	3.3×10^{-8}	9.0×10^{-6}
1500-3000	4.3×10^{-7}	4.3×10^{-7}	4.3×10^{-7}	2.8×10^{-9}	6.2×10^{-7}

Table A.2: Summary of the results for $d\sigma/dm$ measurement in dielectron channel. “Stat. Unc.” is the statistical uncertainty and “Exp. Unc.” means the systematic uncertainty from experimental part including the luminosity uncertainty. “Theo. Unc.” means the systematic uncertainty from theoretical part (PDF and variation of coupling constant). “Total” is a quadratic sum of statistical, experimental and theoretical uncertainties.

2 A.3 Summary of the results for post-FSR $d\sigma/dm$ measurement in dielectron channel

m_{93} (GeV)	Central value (pb/GeV)	Stat. Unc. (pb/GeV)	Exp. Unc. (pb/GeV)	Total Unc. (pb/GeV)
15-20	2.1×10^{-1}	4.8×10^{-3}	1.9×10^{-2}	1.9×10^{-2}
20-25	1.7×10^{-1}	4.8×10^{-3}	1.6×10^{-2}	1.7×10^{-2}
25-30	1.5×10^{-1}	4.9×10^{-3}	1.4×10^{-2}	1.5×10^{-2}
30-35	1.4×10^{-1}	5.0×10^{-3}	1.4×10^{-2}	1.5×10^{-2}
35-40	1.6×10^{-1}	5.6×10^{-3}	1.8×10^{-2}	1.9×10^{-2}
40-45	1.9×10^{-1}	6.7×10^{-3}	2.4×10^{-2}	2.5×10^{-2}
45-50	2.8×10^{-1}	8.3×10^{-3}	3.5×10^{-2}	3.6×10^{-2}
50-55	3.2×10^{-1}	1.0×10^{-2}	4.0×10^{-2}	4.1×10^{-2}
55-60	5.1×10^{-1}	1.2×10^{-2}	5.6×10^{-2}	5.8×10^{-2}
60-64	6.5×10^{-1}	1.9×10^{-2}	6.6×10^{-2}	6.9×10^{-2}
64-68	9.7×10^{-1}	2.5×10^{-2}	8.5×10^{-2}	8.8×10^{-2}
68-72	1.3×10^0	3.1×10^{-2}	1.1×10^{-1}	1.1×10^{-1}
72-76	1.9×10^0	3.7×10^{-2}	1.4×10^{-1}	1.5×10^{-1}
76-81	3.1×10^0	4.2×10^{-2}	2.2×10^{-1}	2.2×10^{-1}
81-86	7.0×10^0	6.2×10^{-2}	4.7×10^{-1}	4.8×10^{-1}
86-91	3.5×10^1	1.1×10^{-1}	2.1×10^0	2.1×10^0
91-96	2.9×10^1	1.0×10^{-1}	1.8×10^0	1.8×10^0
96-101	2.8×10^0	3.6×10^{-2}	1.7×10^{-1}	1.7×10^{-1}
101-106	1.1×10^0	2.0×10^{-2}	6.7×10^{-2}	7.0×10^{-2}
106-110	6.2×10^{-1}	1.9×10^{-2}	3.9×10^{-2}	4.4×10^{-2}
110-115	3.9×10^{-1}	1.3×10^{-2}	2.6×10^{-2}	2.9×10^{-2}
115-120	2.8×10^{-1}	1.1×10^{-2}	1.9×10^{-2}	2.2×10^{-2}
120-126	2.0×10^{-1}	7.9×10^{-3}	1.4×10^{-2}	1.6×10^{-2}
126-133	1.5×10^{-1}	5.8×10^{-3}	1.0×10^{-2}	1.2×10^{-2}
133-141	9.3×10^{-2}	4.5×10^{-3}	6.4×10^{-3}	7.8×10^{-3}
141-150	8.6×10^{-2}	3.8×10^{-3}	6.3×10^{-3}	7.4×10^{-3}
150-160	5.2×10^{-2}	2.9×10^{-3}	3.9×10^{-3}	4.8×10^{-3}
160-171	4.1×10^{-2}	2.3×10^{-3}	3.3×10^{-3}	4.0×10^{-3}
171-185	3.0×10^{-2}	1.7×10^{-3}	2.5×10^{-3}	3.0×10^{-3}
185-200	1.9×10^{-2}	1.3×10^{-3}	1.6×10^{-3}	2.1×10^{-3}
200-220	1.5×10^{-2}	9.7×10^{-4}	1.3×10^{-3}	1.6×10^{-3}

m (GeV)	Central value (pb/GeV)	Stat. Unc. (pb/GeV)	Exp. Unc. (pb/GeV)	Total Unc. (pb/GeV)
220-243	1.0×10^{-2}	7.5×10^{-4}	9.6×10^{-4}	1.3×10^{-3}
243-273	5.6×10^{-3}	4.7×10^{-4}	5.4×10^{-4}	7.2×10^{-4}
273-320	3.5×10^{-3}	2.8×10^{-4}	3.5×10^{-4}	4.5×10^{-4}
320-380	1.9×10^{-3}	1.8×10^{-4}	2.0×10^{-4}	2.7×10^{-4}
380-440	1.2×10^{-3}	1.4×10^{-4}	1.3×10^{-4}	1.9×10^{-4}
440-510	2.4×10^{-4}	7.7×10^{-5}	2.9×10^{-5}	8.2×10^{-5}
510-600	2.7×10^{-4}	4.9×10^{-5}	3.5×10^{-5}	5.9×10^{-5}
600-700	1.4×10^{-4}	3.5×10^{-5}	2.1×10^{-5}	4.1×10^{-5}
700-830	2.9×10^{-5}	1.6×10^{-5}	5.8×10^{-6}	1.7×10^{-5}
830-1000	5.9×10^{-6}	3.5×10^{-6}	2.6×10^{-6}	4.3×10^{-6}
1000-1500	5.0×10^{-6}	2.7×10^{-6}	4.1×10^{-6}	4.9×10^{-6}
1500-3000	2.5×10^{-7}	2.5×10^{-7}	2.7×10^{-7}	3.6×10^{-7}

Table A.3: Summary of the results for the fiducial (post-FSR) $d\sigma/dm$ measurement in dielectron channel. “Stat. Unc.” is the statistical uncertainty and ‘Exp. Unc.’ is the systematic uncertainty from experimental part including the luminosity uncertainty. “Total” is a quadratic sum of statistical and experimental uncertainties.

A.4 ²Summary of the results for full phase space $d\sigma/dm$ measurement in combined channel

m (GeV)	Central value (pb/GeV)	Total Unc. (pb/GeV)
15-20	2.4×10^2	1.8×10^1
20-25	9.9×10^1	6.5×10^0
25-30	5.1×10^1	4.6×10^0
30-35	2.7×10^1	3.1×10^0
35-40	1.6×10^1	1.5×10^0
40-45	1.1×10^1	6.1×10^{-1}
45-50	8.3×10^0	4.2×10^{-1}
50-55	6.1×10^0	2.7×10^{-1}
55-60	5.2×10^0	2.1×10^{-1}
60-64	4.7×10^0	2.0×10^{-1}
64-68	4.8×10^0	2.2×10^{-1}
68-72	5.3×10^0	2.2×10^{-1}
72-76	6.4×10^0	2.4×10^{-1}
76-81	9.5×10^0	3.6×10^{-1}
81-86	2.0×10^1	8.1×10^{-1}
86-91	1.5×10^2	5.0×10^0
91-96	1.5×10^2	4.9×10^0
96-101	1.3×10^1	5.2×10^{-1}
101-106	4.8×10^0	1.8×10^{-1}
106-110	2.5×10^0	1.1×10^{-1}
110-115	1.6×10^0	6.6×10^{-2}
115-120	1.0×10^0	5.2×10^{-2}
120-126	7.5×10^{-1}	3.9×10^{-2}
126-133	5.2×10^{-1}	2.5×10^{-2}
133-141	3.5×10^{-1}	2.0×10^{-2}
141-150	2.7×10^{-1}	1.7×10^{-2}
150-160	1.8×10^{-1}	1.2×10^{-2}
160-171	1.3×10^{-1}	9.7×10^{-3}
171-185	9.1×10^{-2}	7.0×10^{-3}
185-200	5.8×10^{-2}	4.4×10^{-3}
200-220	4.2×10^{-2}	3.6×10^{-3}

m (GeV)	Central value (pb/GeV)	Total Unc. (pb/GeV)
220-243	2.9×10^{-2}	2.5×10^{-3}
243-273	1.6×10^{-2}	1.6×10^{-3}
273-320	9.3×10^{-3}	8.8×10^{-4}
320-380	5.0×10^{-3}	4.9×10^{-4}
380-440	1.8×10^{-3}	2.5×10^{-4}
440-510	8.5×10^{-4}	1.6×10^{-4}
510-600	5.5×10^{-4}	9.7×10^{-5}
600-700	3.1×10^{-4}	5.9×10^{-5}
700-830	7.4×10^{-5}	2.7×10^{-5}
830-1000	2.2×10^{-5}	1.1×10^{-5}
1000-1500	1.0×10^{-5}	3.6×10^{-6}
1500-3000	2.8×10^{-7}	3.8×10^{-7}

2
 Table A.4: Summary of the results for $d\sigma/dm$ measurement in combined channel. The “Total Unc” is a quadratic sum of statistical, experimental and theoretical uncertainties without luminosity uncertainty.

Bibliography

- [1] CMS Collaboration, “Forward-backward asymmetry of DrellYan lepton pairs in pp collisions at $\sqrt{s} = 8$ TeV”, Eur. Phys. J. C **76**, no. 6, 325 (2016) doi:10.1140/epjc/s10052-016-4156-z arXiv:1601.04768 [hep-ex].
- [2] CMS Collaboration, “Measurement of the Drell-Yan Cross Section in pp Collisions at $\sqrt{s} = 7$ TeV”, JHEP **1110**, 007 (2011) doi:10.1007/JHEP10(2011)007 arXiv:1108.0566 [hep-ex].
- [3] CMS Collaboration, “Measurement of the differential and double-differential Drell-Yan cross sections in proton-proton collisions at $\sqrt{s} = 7$ TeV”, JHEP **1312**, 030 (2013) doi:10.1007/JHEP12(2013)030 arXiv:1310.7291 [hep-ex].
- [4] CMS Collaboration, “Measurements of differential and double-differential Drell-Yan cross sections in proton-proton collisions at 8 TeV”, Eur. Phys. J. C **75**, no. 4, 147 (2015) doi:10.1140/epjc/s10052-015-3364-2 arXiv:1412.1115 [hep-ex].
- [5] CMS Collaboration, “Measurement of the differential Drell-Yan cross section in proton-proton collisions at 13 TeV”, CMS-PAS-SMP-16-009.
- [6] D. Griffiths, “Introduction to Elementary Particles”, New York, USA: Wiley (1987).
- [7] D. Perkins, “Introduction to high energy physics”, Cambridge, UK: Cambridge University Press (1982).

- [8] M. Gaillard, P. Grannis and F. Sciulli, “The standard model of particle physics”, Rev. Mod. Phys. **71**, S96 (1999).
- [9] Particle Data Group, “Review of Particle Physics (RPP)”, Phys. Rev. D **86**, 010001 (2012) doi:10.1103/PhysRevD.86.010001.
- [10] M. Gell-Mann, “A Schematic Model of Baryons and Mesons”, Phys. Lett. **8**, 214 (1964) doi:10.1016/S0031-9163(64)92001-3.
- [11] R. Ellis, W. Stirling and B. Webber, “QCD and Collider Physics”, Cambridge Monographs on Particle Physics, Nuclear Physics and Cosmology, Cambridge University Press (2003).
- [12] G. Dissertori, I. Knowles and M. Schmelling, Quantum Chromodynamics: High Energy Experiments and Theory, International Series of Monographs on Physics, OUP Oxford (2009).
- [13] S. Weinberg, “A Model of Leptons”, Phys. Rev. Lett. **19**, 1264 (1967) doi:10.1103/PhysRevLett.19.1264.
- [14] P. W. Higgs, “Broken Symmetries and the Masses of Gauge Bosons”, Phys. Rev. Lett. **13**, 508 (1964) doi:10.1103/PhysRevLett.13.508.
- [15] F. Englert and R. Brout, “Broken Symmetry and the Mass of Gauge Vector Mesons”, Phys. Rev. Lett. **13**, 321 (1964) doi:10.1103/PhysRevLett.13.321.
- [16] G. S. Guralnik, C. R. Hagen and T. W. B. Kibble, “Global Conservation Laws and Massless Particles”, Phys. Rev. Lett. **13**, 585 (1964) doi:10.1103/PhysRevLett.13.585.
- [17] ATLAS Collaboration, “Observation of a new particle in the search for the Standard Model Higgs boson with the ATLAS detector at the LHC”, Phys.

- Lett. B **716** (2012) 1 doi:10.1016/j.physletb.2012.08.020 arXiv:1207.7214 [hep-ex].
- [18] CMS Collaboration, “Observation of a new boson at a mass of 125 GeV with the CMS experiment at the LHC”, Phys. Lett. B **716**, 30 (2012) doi:10.1016/j.physletb.2012.08.021 arXiv:1207.7235 [hep-ex].
- [19] ⁴⁶ A. Salam, “Gauge Unification of Fundamental Forces” Rev. Mod. Phys. **52**, 525 (1980) doi:10.1103/RevModPhys.52.525.
- [20] ³⁷ S. L. Glashow, “Towards a Unified Theory: Threads in a Tapestry”, Rev. Mod. Phys. **52**, 539 (1980) doi:10.1103/RevModPhys.52.539.
- [21] ⁷ J. Goldstone, A. Salam and S. Weinberg, “Broken Symmetries”, Phys. Rev. **127**, 965 (1962) doi:10.1103/PhysRev.127.965.
- [22] ¹ S. D. Drell and T. M. Yan, “Partons and their Applications at High-Energies”, Annals Phys. **66**, 578 (1971) doi:10.1016/0003-4916(71)90071-6.
- [23] J. C. Collins and D. E. Soper, “The Theorems of Perturbative QCD”, Ann. Rev. Nucl. Part. Sci. **37**, 383 (1987) doi:10.1146/annurev.ns.37.120187.002123.
- [24] G. Bozzi, S. Catani and G. Ferrera *et al.*, “¹Transverse-momentum resummation: A Perturbative study of Z production at the Tevatron”, Nucl. Phys. B **815**, 174 (2009) doi:10.1016/j.nuclphysb.2009.02.014 arXiv:0812.2862 [hep-ph].
- [25] ¹ A. V. Lipatov, M. A. Malyshev and N. P. Zotov, “Drell-Yan lepton pair production at high energies in the k_t -factorization approach”, JHEP **1112**, 117 (2011) doi:10.1007/JHEP12(2011)117 arXiv:1110.6582 [hep-ph].
- [26] ⁴⁴ R. P. Feynman, “Very high-energy collisions of hadrons”, Phys. Rev. Lett. **23**, 1415 (1969) doi:10.1103/PhysRevLett.23.1415.
- [27] ¹¹⁷ G. F. Sterman, “QCD and jets”, hep-ph/0412013.

- [28] ¹²⁰ V. D. Barger and R. J. N. Phillips, “Collider Physics”, REDWOOD CITY, USA: ADDISON-WESLEY (1987) 592 P.
- [29] ³ Y. L. Dokshitzer, “Calculation of the Structure Functions for Deep Inelastic Scattering and e+ e- Annihilation by Perturbation Theory in Quantum Chromodynamics.”, Sov. Phys. JETP **46**, 641 (1977).
- [30] V. N. Gribov and L. N. Lipatov, “Deep inelastic e p scattering in perturbation theory”, Sov. J. Nucl. Phys. **15**, 438 (1972).
- [31] G. Altarelli and G. Parisi, “Asymptotic Freedom in Parton Language”, Nucl. Phys. B **126**, 298 (1977) doi:10.1016/0550-3213(77)90384-4.
- [32] ¹⁰⁵ F. Halzen and A. D. Martin, “Quarks And Leptons: An Introductory Course In Modern Particle Physics”, New York, USA: Wiley (1984).
- [33] ⁵ J. Pumplin, ⁵ D. R. Stump and ⁵ J. Huston *et al.*, “New generation of parton distributions with uncertainties from global QCD analysis”, JHEP **0207**, 012 (2002) doi:10.1088/1126-6708/2002/07/012 [hep-ph/0201195].
- [34] A. D. Martin, W. J. Stirling and R. S. Thorne *et al.*, “Parton distributions for the LHC”, Eur. Phys. J. C **63**, 189 (2009) doi:10.1140/epjc/s10052-009-1072-5 arXiv:0901.0002 [hep-ph].
- [35] ¹⁰¹ ZEUS and H1 Collaborations, “Extraction of the proton parton density functions using a NLO-QCD fit of the combined H1 and ZEUS inclusive DIS cross sections” doi:10.3360/dis.2008.25 arXiv:0808.1854 [hep-ph].
- [36] ⁶ R. D. Ball, L. Del Debbio and S. Forte *et al.*, “A first unbiased global NLO determination of parton distributions and their uncertainties”, Nucl. Phys. B **838**, 136 (2010) doi:10.1016/j.nuclphysb.2010.05.008 arXiv:1002.4407 [hep-ph].

- [37] ⁹¹ NNPDF Collaboration, “Parton distributions for the LHC Run II”, JHEP **1504**, 040 (2015) doi:10.1007/JHEP04(2015)040 arXiv:1410.8849 [hep-ph].
- [38] ¹² CDF Collaboration, “Studying the Underlying Event in Drell-Yan and High Transverse Momentum Jet Production at the Tevatron”, Phys. Rev. D **82**, 034001 (2010) doi:10.1103/PhysRevD.82.034001 arXiv:1003.3146 [hep-ex].
- [39] ⁷⁹ Y. K. Kim and U. K. Yang, “Initial State Gluon Radiation in Drell-Yan Dilepton Production”, CDF/PHYS/CDFR/6804 (2004).
- [40] ⁸ T. Sjostrand and M. van Zijl, “A Multiple Interaction Model for the Event Structure in Hadron Collisions”, Phys. Rev. D **36**, 2019 (1987) doi:10.1103/PhysRevD.36.2019.
- [41] ¹⁴ S. D. Drell and T. M. Yan, “Massive Lepton Pair Production in Hadron-Hadron Collisions at High-Energies”, Phys. Rev. Lett. **25**, 316 (1970) doi:10.1103/PhysRevLett.25.316.
- [42] J. C. Collins, D. E. Soper and G. F. Sterman, “Factorization of Hard Processes in QCD”, Adv. Ser. Direct. High Energy Phys. **5**, 1 (1989) doi:10.1142/9789814503266_0001 [hep-ph/0409313].
- [43] ⁶ J. M. Campbell, J. W. Huston and W. J. Stirling, “Hard Interactions of Quarks and Gluons: A Primer for LHC Physics”, Rept. Prog. Phys. **70**, 89 (2007) doi:10.1088/0034-4885/70/1/R02 [hep-ph/0611148].
- [44] ¹ R. Field, “Applications of perturbative QCD Frontiers in physics”, Addison-Wesley, The Advanced Book Program (1989).
- [45] ¹¹¹ B. Delamotte, “A Hint of renormalization”, Am. J. Phys. **72**, 170 (2004) doi:10.1119/1.1624112 [hep-th/0212049].

- [46] ¹⁷¹ L. Evans and P. Bryant, “LHC Machine”, ¹⁴ JINST **3**, S08001 (2008) doi:10.1088/1748-0221/3/08/S08001.
- [47] ATLAS Collaboration, “The ATLAS Experiment at the CERN Large Hadron Collider”, JINST **3**, S08003 (2008) doi:10.1088/1748-0221/3/08/S08003.
- [48] CMS Collaboration, “The CMS Experiment at the CERN LHC”, JINST **3**, S08004 (2008) doi:10.1088/1748-0221/3/08/S08004.
- [49] TOTEM Collaboration, “The TOTEM experiment at the CERN Large Hadron Collider”, JINST **3**, S08007 (2008) doi:10.1088/1748-0221/3/08/S08007.
- [50] LHCf Collaboration, “The LHCf detector at the CERN Large Hadron Collider”, JINST **3**, S08006 (2008) doi:10.1088/1748-0221/3/08/S08006.
- [51] ¹³ ALICE Collaboration, “The ALICE experiment at the CERN LHC”, JINST **3**, S08002 (2008) doi:10.1088/1748-0221/3/08/S08002.
- [52] LHCb Collaboration, “The LHCb Detector at the LHC”, JINST **3**, S08005 (2008) doi:10.1088/1748-0221/3/08/S08005.
- [53] W. Herr and B. Muratori, “Concept of luminosity”.
- [54] CMS Collaboration, “CMS, the magnet project: Technical design report”, CERN-LHCC-97-10.
- [55] ⁵⁵ CMS Collaboration, “CMS, tracker technical design report”, CERN-LHCC-98-06, CMS-TDR-5.
- [56] CMS Collaboration, “The CMS tracker : addendum to the Technical Design Report”, CERN-LHCC-2000-016, CMS-TDR-5-add-1.
- [57] CMS Collaboration, “CMS: The electromagnetic calorimeter. Technical design report”, ¹⁶ CERN-LHCC-97-33, CMS-TDR-4.

- [58] CMS Collaboration, “Addendum to the CMS ECAL technical design report: Changes to the CMS ECAL electronics”, CERN-LHCC-2002-027.
- [59] P. Lecoq *et al.*, “Lead tungstate (PbWO₄) scintillators for LHC EM calorimetry”, Nucl. Instrum. Meth. A **365**, 291 (1995) doi:10.1016/0168-9002(95)00589-7.
- [60] A. A. Annenkov, M. V. Korzhik and P. Lecoq, “Lead tungstate scintillation material”, Nucl. Instrum. Meth. A **490**, 30 (2002) doi:10.1016/S0168-9002(02)00916-6.
- [61] CMS Collaboration, “Avalanche photodiodes and vacuum phototriodes for the electromagnetic calorimeter of the CMS experiment at the Large Hadron Collider”, Nucl. Instrum. Meth. A **604**, 193 (2009) doi:10.1016/j.nima.2009.01.089.
- [62] CMS Collaboration, “CMS: The hadron calorimeter technical design report”, CERN-LHCC-97-31.
- [63] CMS Collaboration, “CMS, the Compact Muon Solenoid. Muon technical design report”, CERN-LHCC-97-32.
- [64] CMS Collaboration, “CMS. The TriDAS project. Technical design report, vol. 1: The trigger systems”, CERN-LHCC-2000-038.
- [65] N. Metropolis and S. Ulam, “The Monte Carlo Method”, Journal of the American Statistical Association **44** 247, 335-441 (1949) doi:10.1080/01621459.1949.10483310.
- [66] B. Andersson, G. Gustafson and G. Ingelman *et al.*, “Parton Fragmentation and String Dynamics”, Phys. Rept. **97**, 31 (1983) doi:10.1016/0370-1573(83)90080-7.
- [67] B. Andersson, G. Gustafson and B. Soderberg, “A General Model for Jet Fragmentation”, Z. Phys. C **20**, 317 (1983) doi:10.1007/BF01407824.

- [68] T. Sjostrand, “The Merging of Jets”, Phys. Lett. **142B**, 420 (1984) doi:10.1016/0370-2693(84)91354-6.
- [69] B. R. Webber, “A QCD Model for Jet Fragmentation Including Soft Gluon Interference”, Nucl. Phys. B **238**, 492 (1984) doi:10.1016/0550-3213(84)90333-X
- [70] ⁹ J. Alwall *et al.*, “MadGraph/MadEvent v4: The New Web Generation”, JHEP **0709**, 028 (2007) doi:10.1088/1126-6708/2007/09/028 arXiv:0706.2334 [hep-ph].
- [71] ⁶ J. Alwall, M. Herquet and F. Maltoni *et al.*, “MadGraph 5 : Going Beyond”, JHEP **1106**, 128 (2011) doi:10.1007/JHEP06(2011)128 arXiv:1106.0522 [hep-ph].
- [72] S. Frixione and B. R. Webber, “Matching NLO QCD computations and parton shower simulations”, JHEP **0206**, 029 (2002) doi:10.1088/1126-6708/2002/06/029 [hep-ph/0204244].
- [73] ⁶⁰ J. Alwall *et al.*, “The automated computation of tree-level and next-to-leading order differential cross sections, and their matching to parton shower simulations”, JHEP **1407**, 079 (2014) doi:10.1007/JHEP07(2014)079 arXiv:1405.0301 [hep-ph].
- [74] CMS Collaboration, “Event generator tunes obtained from underlying event and multiparton scattering measurements”, Eur. Phys. J. C **76**, no. 3, 155 (2016) doi:10.1140/epjc/s10052-016-3988-x arXiv:1512.00815 [hep-ex].
- [75] ²⁰ R. Frederix and S. Frixione, “Merging meets matching in MC@NLO”, JHEP **1212**, 061 (2012) doi:10.1007/JHEP12(2012)061 arXiv:1209.6215 [hep-ph].
- [76] T. Sjostrand, S. Mrenna and P. Z. Skands, “PYTHIA 6.4 Physics and Manual”, JHEP **0605**, 026 (2006) doi:10.1088/1126-6708/2006/05/026 [hep-ph/0603175].

- [77] T. Sjstrand ⁸⁵ *et al.*, “An Introduction to PYTHIA 8.2”, Comput. Phys. Commun. **191**, 159 (2015) doi:10.1016/j.cpc.2015.01.024 arXiv:1410.3012 [hep-ph].
- [78] ⁶ P. Nason, “A New method for combining NLO QCD with shower Monte Carlo algorithms”, JHEP **0411**, 040 (2004) doi:10.1088/1126-6708/2004/11/040 [hep-ph/0409146].
- [79] S. Frixione, P. Nason and C. Oleari, “Matching NLO QCD computations with Parton Shower simulations: the POWHEG method”, JHEP **0711**, 070 (2007) doi:10.1088/1126-6708/2007/11/070 arXiv:0709.2092 [hep-ph].
- [80] S. Alioli, P. Nason and C. Oleari *et al.*, “A general framework for implementing NLO calculations in shower Monte Carlo programs: the POWHEG BOX”, JHEP **1006**, 043 (2010) doi:10.1007/JHEP06(2010)043 arXiv:1002.2581 [hep-ph].
- [81] S. Alioli, P. Nason and C. Oleari *et al.*, “NLO vector-boson production matched with shower in POWHEG”, JHEP **0807**, 060 (2008) doi:10.1088/1126-6708/2008/07/060 arXiv:0805.4802 [hep-ph].
- [82] [GEANT4 Collaboration], “GEANT4: A Simulation toolkit”, Nucl. Instrum. Meth. A **506**, 250 (2003) doi:10.1016/S0168-9002(03)01368-8
- [83] J. Allison *et al.*, “Geant4 developments and applications”, IEEE Trans. Nucl. Sci. **53**, 270 (2006) doi:10.1109/TNS.2006.869826
- [84] ¹³ K. Rose, “Deterministic annealing for clustering, compression, classification, regression, and related optimization problems”, Proceedings of the IEEE **86**, 2210 (1998) doi:10.1109/5.726788.
- [85] ³³ CMS Collaboration, “Energy Calibration and Resolution of the CMS Electromagnetic Calorimeter in pp Collisions at $\sqrt{s} = 7$ TeV”, JINST **8**, P09009 (2013) doi:10.1088/1748-0221/8/09/P09009 arXiv:1306.2016 [hep-ex].

- [86] ⁷ CMS Collaboration, “Performance of Electron Reconstruction and Selection with the CMS Detector in Proton-Proton Collisions at $s = 8$ TeV”, JINST **10**, no. 06, P06005 (2015) doi:10.1088/1748-0221/10/06/P06005 arXiv:1502.02701 [physics.ins-det].
- [87] ⁵ R. Fruhwirth, “Application of Kalman filtering to track and vertex fitting”, Nucl. Instrum. Meth. A **262**, 444 (1987) doi:10.1016/0168-9002(87)90887-4.
- [88] T. Speer, ⁴⁵ R. Fruhwirt, “A Gaussian-sum filter for vertex reconstruction”, Computer Physics Communications **174** 935 (2006) doi:10.1016/j.cpc.2006.01.005.
- [89] CMS Collaboration, “Energy smearing and scale correction”, ⁶⁶ URL: <https://twiki.cern.ch/twiki/bin/viewauth/CMS/EGMSmearer> (visited on 2016-02-18).
- [90] ¹⁸ CMS Collaboration, “Particle-Flow Event Reconstruction in CMS and Performance for Jets, Taus, and MET”, CMS-PAS-PFT-09-001.
- [91] CMS Collaboration, “Commissioning of the Particle-flow Event Reconstruction with the first LHC collisions recorded in the CMS detector”, CMS-PAS-PFT-10-001.
- [92] ⁹ M. Cacciari and G. P. Salam, “Pileup subtraction using jet areas”, Phys. Lett. B **659**, 119 (2008) doi:10.1016/j.physletb.2007.09.077 arXiv:0707.1378 [hep-ph].
- [93] M. Cacciari, G. P. Salam and G. Soyez, “The Catchment Area of Jets”, JHEP **0804**, 005 (2008) doi:10.1088/1126-6708/2008/04/005 arXiv:0802.1188 [hep-ph].
- [94] ¹⁷ M. Cacciari, G. P. Salam and G. Soyez, “FastJet User Manual”, Eur. Phys. J. C **72**, 1896 (2012) doi:10.1140/epjc/s10052-012-1896-2 arXiv:1111.6097 [hep-ph].

- [95] M. Cacciari, G. P. Salam and G. Soyez, “The Anti-k(t) jet clustering algorithm,” JHEP **0804**, 063 (2008) doi:10.1088/1126-6708/2008/04/063 arXiv:0802.1189 [hep-ph].
- [96] CMS Collaboration, “Cut Based Electron ID for Run 2”, <https://twiki.cern.ch/twiki/bin/view/CMS/CutBasedElectronIdentificationRun2> (visited on 2015-12-22).
- [97] CMS Collaboration, “Baseline muon selections for Run-II”, <https://twiki.cern.ch/twiki/bin/view/CMS/SWGuideMuonIdRun2> (visited on 2016-07-04).
- [98] R. Gavin, Y. Li, F. Petriello and S. Quackenbush, “FEWZ 2.0: A code for hadronic Z production at next-to-next-to-leading order”, Comput. Phys. Commun. **182**, 2388 (2011) doi:10.1016/j.cpc.2011.06.008 arXiv:1011.3540 [hep-ph].
- [99] Y. Li and F. Petriello, “Combining QCD and electroweak corrections to dilepton production in FEWZ”, Phys. Rev. D **86**, 094034 (2012) doi:10.1103/PhysRevD.86.094034 arXiv:1208.5967 [hep-ph].
- [100] D. Bourilkov, “Photon-induced Background for Dilepton Searches and Measurements in pp Collisions at 13 TeV”, arXiv:1606.00523 [hep-ph].
- [101] V. Blobel, “An Unfolding method for high-energy physics experiments”, hep-ex/0208022.
- [102] G. D’Agostini, “A Multidimensional unfolding method based on Bayes’ theorem”, Nucl. Instrum. Meth. A **362**, 487 (1995) doi:10.1016/0168-9002(95)00274-X.
- [103] CMS Collaboration, “Measurement of the Inclusive W and Z Production Cross Sections in pp Collisions at $\sqrt{s} = 7$ TeV”, JHEP **1110**, 132 (2011) doi:10.1007/JHEP10(2011)132 arXiv:1107.4789 [hep-ex].

- [104] CMS Collaboration, “Details of the Tag and Probe procedure for Egamma”,
<https://twiki.cern.ch/twiki/bin/viewauth/CMS/ElectronScaleFactorsRun2>
(visted on 2016-06-26).
- [105] CMS Collaboration, “CMS Luminosity Measurement for the 2015 Data Taking Period”, CMS-PAS-LUM-15-001.
- [106] M. R. Whalley, D. Bourilkov and R. C. Group, “The Les Houches accord PDFs (LHAPDF) and LHAGLUE”, hep-ph/0508110.
- [107] D. Bourilkov, R. C. Group and M. R. Whalley, “LHAPDF: PDF use from the Tevatron to the LHC”, hep-ph/0605240.
- [108] A. Buckley, J. Ferrando and S. Lloyd *et al.*, “LHAPDF6: parton density access in the LHC precision era”, Eur. Phys. J. C **75**, 132 (2015)
doi:10.1140/epjc/s10052-015-3318-8 arXiv:1412.7420 [hep-ph].
- [109] E. Barberio, B. van Eijk and Z. Was, “PHOTOS: A Universal Monte Carlo for QED radiative corrections in decays”, Comput. Phys. Commun. **66**, 115 (1991)
doi:10.1016/0010-4655(91)90012-A.
- [110] E. Barberio and Z. Was, “PHOTOS: A Universal Monte Carlo for QED radiative corrections. Version 2.0”, Comput. Phys. Commun. **79**, 291 (1994)
doi:10.1016/0010-4655(94)90074-4.
- [111] CMS Collaboration, “Measurement of inclusive W and Z boson production cross sections in pp collisions at $\sqrt{s}=13$ TeV”, CMS-PAS-SMP-15-004.
- [112] G. D. Lafferty and T. R. Wyatt, “Where to stick your data points: The treatment of measurements within wide bins”, Nucl. Instrum. Meth. A **355**, 541 (1995) doi:10.1016/0168-9002(94)01112-5.

- [113] A. Valassi, "Combining correlated measurements of several different physical quantities", Nucl. Instrum. Meth. A **500**, 391 (2003) doi:10.1016/S0168-9002(03)00329-2.



PRIMARY SOURCES

- | | | |
|---|--|-----------|
| 1 | cms.desy.de
Internet Source | 5% |
| 2 | S. Chatrchyan, V. Khachatryan, A. M. Sirunyan,
A. Tumasyan et al. "Measurement of the
differential and double-differential Drell-Yan
cross sections in proton-proton collisions at $\sqrt{s} = 7 \text{ TeV}$ ", Journal of High Energy
Physics, 2013
Publication | 2% |
| 3 | bura.brunel.ac.uk
Internet Source | 1% |
| 4 | arpi.unipi.it
Internet Source | 1% |
| 5 | www.infn.it
Internet Source | 1% |
| 6 | link.springer.com
Internet Source | 1% |
| 7 | www.research-collection.ethz.ch
Internet Source | 1% |
-

8	digbib.ubka.uni-karlsruhe.de	1 %
Internet Source		
9	arxiv.org	1 %
Internet Source		
10	Submitted to Higher Education Commission Pakistan	1 %
Student Paper		
11	publikationen.bibliothek.kit.edu	1 %
Internet Source		
12	ekpwww.ekp.kit.edu	<1 %
Internet Source		
13	boa.unimib.it	<1 %
Internet Source		
14	d-nb.info	<1 %
Internet Source		
15	repository.ubn.ru.nl	<1 %
Internet Source		
16	amsdottorato.unibo.it	<1 %
Internet Source		
17	eprints.lancs.ac.uk	<1 %
Internet Source		
18	Stober, Fred Markus. "Measurement of the three-jet mass cross-section at 7 TeV", Universität Karlsruhe, 2012.	<1 %

- 19 web.iihe.ac.be <1 %
Internet Source
-
- 20 cp3.irmp.ucl.ac.be <1 %
Internet Source
-
- 21 lss.fnal.gov <1 %
Internet Source
-
- 22 Schmidt, Evelyn. "Search for the Standard Model Higgs boson in the $H \rightarrow W^+W^- \rightarrow \ell^+\nu\ell^-\bar{\nu}$ decay mode in proton-proton collisions at $\sqrt{s}=7\text{ TeV}$ and $\sqrt{s}=8\text{ TeV}$ with the ATLAS experiment", Universität Freiburg, 2013.
Publication <1 %
-
- 23 arjuna.ist.utl.pt <1 %
Internet Source
-
- 24 Submitted to Imperial College of Science, Technology and Medicine <1 %
Student Paper
-
- 25 www.freidok.uni-freiburg.de <1 %
Internet Source
-
- 26 Springer Theses, 2014. <1 %
Publication
-
- 27 The CMS Collaboration. "The CMS experiment

28

Abbaneo, D, Abbiendi, G, Abbrescia, M,
Abdullin, S, Acosta, D, Acosta, JG, Adair, A,
Adam, N, Adam, W, Adams, MR, Adams, T,
Adiguzel, A, Adler, V, Adzic, P, Afanasiev, S,
Agostino, L, Agram, JL, Aguilar-Benitez, M,
Aguilo, E, Ahmad, M, Ahmed, I, Ahuja, S,
Akchurin, N, Akgun, B, Akgun, U, Akin, IV,
Alagoz, E, Albajar, C, Albayrak, EA, Albergo, S,
Albrow, M, Alcaraz Maestre, J, Alda Junior,
WL, Aldaya Martin, M, Alexander, J, Aliev, T,
Almeida, N, Alver, B, Alverson, G, Alves, GA,
Amapane, N, Amsler, C, Anagnostou, G,
Anastassov, A, Anderson, J, Anderson, M,
Andrea, J, Andreev, V, Andreev, Y, Andrews,
W, Anghel, IM, Ansari, MH, Antonelli, L,
Antunovic, Z, Apanasevich, L, Apollinari, G,
Appelt, E, Apresyan, A, Aranyi, A, Arce, P,
Arcidiacono, R, Arenton, MW, Arfaei, H, Argiro,
S, Arisaka, K, Arneodo, M, Arora, S, Asghar,
MI, Askew, A, Assran, Y, Ata, M, Atac, M,
Atramentov, O, Attikis, A, Auffray, E,
Autermann, C, Auzinger, G, Avery, P,
Avetisyan, A, Azarkin, M, Azhgirey, I, Aziz, T et
al. "Measurement of the Drell-Yan cross section
in pp collisions at $\sqrt{s}=7$ TeV", Springer, 2011.

<1 %

29

Hartert, Jochen. "Measurement of the W->enu and Z/gamma*>ee Production Cross-Sections in Proton-Proton Collisions at sqrt(s)=7 TeV with the ATLAS Experiment", Universität Freiburg, 2012.

Publication

<1 %

30

Submitted to University of Sheffield

Student Paper

<1 %

31

Chatrchyan, S., V. Khachatryan, A. M. Sirunyan, A. Tumasyan, W. Adam, T. Bergauer, M. Dragicevic, J. Erö, C. Fabjan, M. Friedl, R. Frühwirth, V. M. Ghete, N. Hörmann, J. Hrubec, M. Jeitler, W. Kiesenhofer, V. Knünz, M. Krammer, I. Krätschmer, D. Liko, I. Mikulec, D. Rabady, B. Rahbaran, C. Rohringer, H. Rohringer, R. Schöfbeck, J. Strauss, A. Taurok, W. Treberer-Treberspurg, W. Waltenberger, C.-E. Wulz, V. Mossolov, N. Shumeiko, J. Suarez Gonzalez, S. Alderweireldt, M. Bansal, S. Bansal, T. Cornelis, E. A. Wolf, X. Janssen, A. Knutsson, S. Luyckx, L. Mucibello, S. Ochesanu, B. Roland, R. Rougny, Z. Staykova, H. Haevermaet, P. Mechelen, N. Remortel, A. Spilbeeck, F. Blekman, S. Blyweert, J. D'Hondt, A. Kalogeropoulos, J. Keaveney, M. Maes, A. Olbrechts, S. Tavernier, W. Doninck, P. Mulders, G. P. Onsem, I. Villella, C. Caillol, B.

Clerbaux, G. Lentdecker, L. Favart, A. P. R.
Gay, T. Hreus, A. Léonard, P. E. Marage, A.
Mohammadi, L. Perniè, T. Reis, T. Seva, L.
Thomas, C. Vander Velde, P. Vanlaer, J. Wang,
V. A. "Measurement of the differential and
double-differential Drell-Yan cross sections in
proton-proton collisions at $\sqrt{s} = 7 \text{ TeV}$ ",
Journal of High Energy Physics, 2013.

Publication

32

elpub.bib.uni-wuppertal.de

Internet Source

<1 %

33

v-scheiner.brunel.ac.uk

Internet Source

<1 %

34

Francesco Pandolfi. "Search for the Standard Model Higgs Boson in the $H \rightarrow ZZ \rightarrow l + l - qq$ Decay Channel at CMS", Springer Nature, 2013

Publication

<1 %

35

pastel.archives-ouvertes.fr

Internet Source

<1 %

36

Bauer, Julia. "Perspektiven zur Beobachtung der elektroschwachen Produktion einzelner Top-Quarks mit dem CMS Experiment", Universität Karlsruhe, 2010.

Publication

<1 %

37

ubm.opus.hbz-nrw.de

Internet Source

<1 %

38	Submitted to Cranfield University Student Paper	<1 %
39	iopscience.iop.org Internet Source	<1 %
40	Submitted to University of Bristol Student Paper	<1 %
41	JINDAL, M. "Drell-Yan process at Large Hadron Collider", Pramana: Journal of Physics/03044289, 20110301 Publication	<1 %
42	www.iihe.ac.be Internet Source	<1 %
43	www-d0.fnal.gov Internet Source	<1 %
44	media.proquest.com Internet Source	<1 %
45	etd.adm.unipi.it Internet Source	<1 %
46	edoc.hu-berlin.de Internet Source	<1 %
47	confluence.desy.de Internet Source	<1 %
48	porthos.ist.utl.pt Internet Source	<1 %

49

www-ekp.physik.uni-karlsruhe.de

Internet Source

<1 %

50

edoc.ub.uni-muenchen.de

Internet Source

<1 %

51

eprints.whiterose.ac.uk

Internet Source

<1 %

52

Submitted to Middle East Technical University

Student Paper

<1 %

53

Abbaneo, D, Abbiendi, G, Abbrescia, M,
Abdullin, S, Acosta, D, Acosta, JG, Acosta, MV,
Adam, N, Adam, W, Adams, MR, Adams, T,
Adiguzel, A, Adler, V, Adzic, P, Agostino, L,
Agram, JL, Aguilar-Benitez, M, Aguilo, E,
Ahmad, M, Ahmad, WH, Ahmed, I, Ahuja, S,
Akchurin, N, Akgun, B, Akgun, U, Akin, IV,
Alagoz, E, Albajar, C, Albayrak, EA, Albergo, S,
Albrow, M, Alexander, J, Aliev, T, Allfrey, P,
Almeida, N, Alver, B, Alverson, G, Alves, GA,
Amapane, N, Ambroglini, F, Amsler, C,
Anagnostou, G, Anastassov, A, Anderson, J,
Anderson, M, Andrea, J, Andreev, V, Andreev,
Y, Andrews, W, Anghel, IM, Antonelli, L,
Antunovic, Z, Apanasevich, L, Apollinari, G,
Appelt, E, Apresyan, A, Aranyi, A, Arce, P,
Arcidiacono, R, Arenton, MW, Arfaei, H, Argiro,
S, Arisaka, K, Arneodo, M, Asaadi, J, Asghar,
MI, Askew, A, Assran, Y, Ata, M, Atac, M,

<1 %

Atramentov, O, Attikis, A, Auffray, E,
Autermann, C, Auzinger, G, Avery, P,
Avetisyan, A, Azarkin, M, Azhgirey, I, Aziz, T,
Azzi, P, Azzolini, V, Azzurri, P, Baarmand et al.
"Prompt and non-prompt J/psi production in pp
collisions at root s=7 TeV", Springer Verlag,
2012.

Publication

54

www.openaccessrepository.it

Internet Source

<1 %

55

Tröndle, Daniel Cedric. "Search for
Supersymmetrie using Multileptonic Signatures
in Proton-Proton Collisions with the CMS
Detector at the LHC", Universität Karlsruhe,
2012.

Publication

56

digital.csic.es

Internet Source

<1 %

57

Martin, William Patrick(Hobson, PR).
"Measurement of the single top tW associated
production cross section at 7 TeV with 4.9 fb-1
of data in the dilepton decay channel at the
LHC using the CMS detector", Brunel University
School of Engineering and Design PhD Theses,
2013.

Publication

<1 %

www.hephy.at

58

Internet Source

<1 %

59

Springer Theses, 2015.

<1 %

60

discoverycenter.nbi.ku.dk

Internet Source

<1 %

61

scpc00.unige.ch

Internet Source

<1 %

62

atlas-archiv.desy.de

Internet Source

<1 %

63

portal.uni-freiburg.de

Internet Source

<1 %

64

ediss.uni-goettingen.de

Internet Source

<1 %

65

Abbaneo, D, Abbiendi, G, Abbrescia, M,
Abdullin, S, Acosta, D, Acosta, JG, Acosta, MV,
Adair, A, Adam, N, Adam, W, Adams, MR,
Adams, T, Adiguzel, A, Adler, V, Adzic, P,
Afanasiev, S, Agostino, L, Agram, JL, Aguilar-
Benitez, M, Aguilo, E, Ahmad, M, Ahmad, WH,
Ahuja, S, Akchurin, N, Akgun, B, Akgun, U,
Akin, IV, Alagoz, E, Albajar, C, Albayrak, EA,
Albergo, S, Albrow, M, Alcaraz Maestre, J, Alda
Junior, WL, Alexander, J, Aliev, T, Almeida, N,
Alver, B, Alverson, G, Alves, GA, Amapane, N,

<1 %

Amsler, C, Anagnostou, G, Anastassov, A, Anderson, J, Anderson, M, Andrea, J, Andreev, V, Andreev, Y, Andrews, W, Anghel, IM, Anjos, TS, Antonelli, L, Antunes, JR, Antunovic, Z, Apanasevich, L, Apollinari, G, Appelt, E, Apresyan, A, Aranyi, A, Arce, P, Arcidiacono, R, Arenton, MW, Arfaei, H, Argiro, S, Arisaka, K, Arneodo, M, Arora, S, Asghar, MI, Askew, A, Assran, Y, Ata, M, Atac, M, Atramentov, O, Attikis, A, Auffray, E, Autermann, C, Auzinger, G, Avdeeva, E, Avery, P, Avetisyan, A, Azarkin, M et al. "Measurement of the rapidity and transverse momentum distributions of Z bosons in pp collisions at $\sqrt{s}=7$ TeV", American Physical Society, 2012.

Publication

66

www.qucosa.de

Internet Source

<1 %

67

The Large Hadron Collider, 2015.

Publication

<1 %

68

Göringer, Christian. "Search for high mass resonances decaying into electron-positron pairs in proton-proton collisions at $\text{sqrt}(s) = 7$ TeV with the ATLAS detector", 08: Physik, Mathematik und Informatik. 08: Physik, Mathematik und Informatik, 2013.

Publication

<1 %

69

Dietrich, Janet. "Search for supersymmetric particles in final states with jets and missing energy with the ATLAS Experiment at the LHC", Universität Freiburg, 2011.

<1 %

Publication

70

www.physics.uiowa.edu

<1 %

Internet Source

71

The CMS Collaboration. "CMS Physics Technical Design Report, Volume II: Physics Performance", Journal of Physics G Nuclear and Particle Physics, 06/01/2007

<1 %

Publication

72

Submitted to University College London

<1 %

Student Paper

73

paperity.org

<1 %

Internet Source

74

Peiffer, Thomas. "Erste Messung der Ladungsasymmetrie und Suche nach schweren Resonanzen in der Top-Quark-Paarproduktion mit dem CMS-Experiment", Universität Karlsruhe, 2011.

<1 %

Publication

75

tdx.cat

<1 %

Internet Source

76

cvfeller.cv.ic.ac.uk

<1 %

Internet Source

77	www.science.gov Internet Source	<1 %
78	Gruschke, Jasmin. "Nachweis von Top-Quarks und erste Messung des $t\bar{t}$ -Wirkungsquerschnitts bei einer Schwerpunktsenergie von 7 TeV mit dem CMS-Experiment am LHC. Observation of Top Quarks and First Measurement of the $t\bar{t}$ -Production Cross Section at a Centre-of-Mass Energy of the 7 TeV with the CMS Experiment at the LHC", Universität Karlsruhe, 2011. Publication	<1 %
79	www-cdf.fnal.gov Internet Source	<1 %
80	www.phy.duke.edu Internet Source	<1 %
81	Submitted to Brunel University Student Paper	<1 %
82	Niegel, Martin. "Search for Supersymmetry in Trimuon Final States with the CMS Detector", Universität Karlsruhe, 2009. Publication	<1 %
83	www.nikhef.nl Internet Source	<1 %

84	Submitted to Universiteit van Amsterdam Student Paper	<1 %
85	sro.sussex.ac.uk Internet Source	<1 %
86	Submitted to Kyungpook National University Student Paper	<1 %
87	physics.puchd.ac.in Internet Source	<1 %
88	Khachatryan, V., A. M. Sirunyan, A. Tumasyan, W. Adam, T. Bergauer, M. Dragicevic, J. Erö, M. Friedl, R. Frühwirth, V. M. Ghete, C. Hartl, N. Hörmann, J. Hrubec, M. Jeitler, W. Kiesenhofer, V. Knünz, M. Krammer, I. Krätschmer, D. Liko, I. Mikulec, D. Rabady, B. Rahbaran, H. Rohringer, R. Schöfbeck, J. Strauss, W. Treberer-Treberspurg, W. Waltenberger, C.-E. Wulz, V. Mossolov, N. Shumeiko, J. Suarez Gonzalez, S. Alderweireldt, S. Bansal, T. Cornelis, E. A. De Wolf, X. Janssen, A. Knutsson, J. Lauwers, S. Luyckx, S. Ochesanu, R. Rougny, M. Van De Klundert, H. Van Haevermaet, P. Van Mechelen, N. Van Remortel, A. Van Spilbeeck, F. Blekman, S. Blyweert, J. D'Hondt, N. Daci, N. Heracleous, J. Keaveney, S. Lowette, M. Maes, A. Olbrechts, Q. Python, D. Strom, S. Tavernier,	<1 %

W. Van Doninck, P. Van Mulders, G. P. Van Onsem, I. Villella, C. Caillol, B. Clerbaux, G. De Lentdecker, D. Dobur, L. Favart, A. P. R. Gay, A. Grebenyuk, A. Léonard, A. Mohammadi, L. Perniè, A. Randle-conde, T. Reis, T. Seva et al. "Measurements of differential and double-differential Drell–Yan cross sections in proton–proton collisions at $\sqrt{s} = 8$ TeV", The European Physical Journal C, 2015.

Publication

89	uu.diva-portal.org	<1 %
90	particle.hep.lu.se	<1 %
91	Springer Tracts in Modern Physics, 2016.	<1 %
92	133.11.24.21	<1 %
93	www3.tsl.uu.se	<1 %
94	Lange, Clemens(Husemann, Ulrich, Lacker, Heiko and Masetti, Lucia). "A novel approach to precision measurements of the top quark-antiquark pair production cross section with the ATLAS experiment", Mathematisch-	<1 %

Naturwissenschaftliche Fakultät I, 2013.

Publication

95	www-zeus.desy.de Internet Source	<1 %
96	download.iop.org Internet Source	<1 %
97	digre.pmf.unizg.hr Internet Source	<1 %
98	docnum.umons.ac.be Internet Source	<1 %
99	Submitted to Royal Holloway and Bedford New College Student Paper	<1 %
100	Warsinsky, Markus (Dr. Frank Krauss, Prof. Dr. Markus Schumacher, Prof. Dr. Michael Kobel, Technische Universität Dresden, Institut für Kern- und Teilchenphysik and Technische Universität Dresden, Physik). "Studies of b-associated production and muonic decays of neutral Higgs bosons at the ATLAS experiment within the Minimal Supersymmetric Standard Model", Saechsische Landesbibliothek- Staats- und Universitaetsbibliothek Dresden, 2008. Publication	<1 %
101	Submitted to University of Keele Student Paper	<1 %

- 102 Ott, Jochen. "Search for Resonant Top Quark Pair Production in the Muon+Jets Channel with the CMS Detector", Universität Karlsruhe, 2012. <1 %
Publication
-
- 103 A. M. Sirunyan, A. Tumasyan, W. Adam, E. Asilar et al. "Search for associated production of dark matter with a Higgs boson decaying to $b\bar{b}$ or $\gamma\gamma$ at $s = 13$ TeV", Journal of High Energy Physics, 2017 <1 %
Publication
-
- 104 Springer Theses, 2016. <1 %
Publication
-
- 105 hss.ulb.uni-bonn.de <1 %
Internet Source
-
- 106 www.mi.infn.it <1 %
Internet Source
-
- 107 personal.ifae.es <1 %
Internet Source
-
- 108 JINDAL, M. "Measurement of the Drell-Yan differential cross-section $d\sigma/dM$ at $\sqrt{s} = 7$ TeV", Pramana: Journal of Physics, 2012. <1 %
Publication
-
- 109 boris.unibe.ch <1 %
Internet Source
-

- 110 Chwalek, Thorsten. "Messung der W-Boson-Helizitätsanteile in Top-Quark-Zerfällen mit dem CDF II Experiment und Studien zu einer frühen Messung des ttbar-Wirkungsquerschnitts mit dem CMS Experiment", Universität Karlsruhe, 2010. <1 %
Publication
-
- 111 Submitted to University of Durham <1 %
Student Paper
-
- 112 www.eusflat.org <1 %
Internet Source
-
- 113 Ellis, John, Kazuki Sakurai, and Michael Spannowsky. "Search for sphalerons: IceCube vs. LHC", Journal of High Energy Physics, 2016. <1 %
Publication
-
- 114 www.tantrik-astrologer.in <1 %
Internet Source
-
- 115 Khachatryan, V., A. M. Sirunyan, A. Tumasyan, W. Adam, E. Asilar, T. Bergauer, J. Brandstetter, E. Brondolin, M. Dragicevic, J. Erö, M. Friedl, R. Frühwirth, V. M. Ghete, C. Hartl, N. Hörmann, J. Hrubec, M. Jeitler, V. Knünz, A. König, M. Krammer, I. Krätschmer, D. Liko, T. Matsushita, I. Mikulec, D. Rabady, B. Rahbaran, H. Rohringer, J. Schieck, R. <1 %

Schöfbeck, J. Strauss, W. Treberer-Treberspurg, W. Waltenberger, C. -E. Wulz, V. Mossolov, N. Shumeiko, J. Suarez Gonzalez, S. Alderweireldt, T. Cornelis, E. A. De Wolf, X. Janssen, A. Knutsson, J. Lauwers, S. Luyckx, M. Van De Klundert, H. Van Haevermaet, P. Van Mechelen, N. Van Remortel, A. Van Spilbeeck, S. Abu Zeid, F. Blekman, J. D'Hondt, N. Daci, I. De Bruyn, K. Deroover, N. Heracleous, J. Keaveney, S. Lowette, L. Moreels, A. Olbrechts, Q. Python, D. Strom, S. Tavernier, W. Van Doninck, P. Van Mulders, G. P. Van Onsem, I. Van Parijs, P. Barria, H. Brun, C. Caillol, B. Clerbaux, G. De Lentdecker, G. Fasanella, L. Favart, A. Grebenyuk et al.
"Measurement of $\mathrm{t\bar{t}}$ production with additional jet activity, including b quark jets, in the dilepton decay channel using pp collisions at $\sqrt{s} = 8 \text{ TeV}$ ", The European Physical Journal C, 2016.

Publication

116

Cakir, Muammer Altan. "Standard Model Background Studies for SUSY Searches with the CMS Detector at the LHC", Universität Karlsruhe, 2010.

Publication

<1 %

- 117 cds.cern.ch <1 %
Internet Source
- 118 www-zeus.physik.uni-bonn.de <1 %
Internet Source
- 119 Renz, Manuel. "Erste Messung des Wirkungsquerschnitts der Top-Quark-Paarproduktion bei $\text{sqrt}(s) = 7 \text{ TeV}$ im Elektron+Jets Kanal mit dem CMS-Experiment", Universität Karlsruhe, 2011.
Publication <1 %
- 120 physics.wm.edu <1 %
Internet Source
- 121 ekpwww.physik.uni-karlsruhe.de <1 %
Internet Source
- 122 -of-audit-committee <1 %
Internet Source
- 123 Hackstein, Christoph. "Searches for the Higgs Boson at the LHC Based on its Couplings to Vector Bosons", Universität Karlsruhe, 2011.
Publication <1 %
- 124 Scheurer, Armin. "Algorithms for the Identification of b-Quark Jets with First Data at CMS", Universität Karlsruhe, 2008.
Publication <1 %
- 125 w3.atomki.hu

<1 %

126	arbur.net Internet Source	<1 %
127	www.hep.uiuc.edu Internet Source	<1 %
128	Submitted to Chonnam National University Student Paper	<1 %
129	archiv.ub.uni-heidelberg.de Internet Source	<1 %
130	yliu.web.cern.ch Internet Source	<1 %
131	www.tdx.cat Internet Source	<1 %
132	personalpages.to.infn.it Internet Source	<1 %
133	Khachatryan, V., A. M. Sirunyan, A. Tumasyan, W. Adam, E. Asilar, T. Bergauer, J. Brandstetter, E. Brondolin, M. Dragicevic, J. Erö, M. Flechl, M. Friedl, R. Frühwirth, V. M. Ghete, C. Hartl, N. Hörmann, J. Hrubec, M. Jeitler, V. Knünz, A. König, M. Krammer, I. Krätschmer, D. Liko, T. Matsushita, I. Mikulec, D. Rabady, B. Rahbaran, H. Rohringer, J. Schieck, R. Schöfbeck, J. Strauss, W. Treberer-	<1 %

Treberspurg, W. Waltenberger, C. -E. Wulz, V. Mossolov, N. Shumeiko, J. Suarez Gonzalez, S. Alderweireldt, T. Cornelis, E. A. De Wolf, X. Janssen, A. Knutsson, J. Lauwers, S. Luyckx, M. Van De Klundert, H. Van Haevermaet, P. Van Mechelen, N. Van Remortel, A. Van Spilbeeck, S. Abu Zeid, F. Blekman, J. D'Hondt, N. Daci, I. De Bruyn, K. Deroover, N. Heracleous, J. Keaveney, S. Lowette, L. Moreels, A. Olbrechts, Q. Python, D. Strom, S. Tavernier, W. Van Doninck, P. Van Mulders, G. P. Van Onsem, I. Van Parijs, P. Barria, H. Brun, C. Caillol, B. Clerbaux, G. De Lentdecker, G. Fasanella, L. Favart, A. Grebenyuk et al. "Forward–backward asymmetry of Drell–Yan lepton pairs in pp collisions at $\sqrt{s} = 8 \text{ TeV}$ ", The European Physical Journal C, 2016.

Publication

134	Submitted to Queen Mary and Westfield College	<1 %
135	www.triumf.ca Internet Source	<1 %
136	wwweth.cern.ch Internet Source	<1 %
137	Büge, Volker. "Virtualisation of Grid Resources	

and Prospects of the Measurement of Z Boson Production in Association with Jets at the LHC", Universität Karlsruhe, 2008.

<1 %

Publication

- 138 Fasanella, Daniele <1981>(Rossi, Antonio Maria). "Study of the X(3872) state with the CMS experiment at LHC", Alma Mater Studiorum - Università di Bologna, 2012.

<1 %

Publication

- 139 Submitted to University of Oxford
Student Paper

<1 %

- 140 Submitted to Vrije Universiteit Brussel
Student Paper

<1 %

- 141 www.microplanning.com.au
Internet Source

<1 %

- 142 jinst.sissa.it
Internet Source

<1 %

- 143 cris.cumulus.vub.ac.be
Internet Source

<1 %

- 144 villaolmo.mib.infn.it
Internet Source

<1 %

- 145 Submitted to KTH - The Royal Institute of Technology
Student Paper

<1 %

- 146 www.ifw-dresden.de

<1 %

147 www.doria.fi <1 %
Internet Source

148 hermes.desy.de <1 %
Internet Source

149 Steinbach, Peter (Prof. Dr. Michael Kobel, Prof. Dr. Ulrich Husemann and Technische Universität Dresden, Fakultät Mathematik und Naturwissenschaften). "A Cross Section Measurement Of Events With Two Muons At The Z^0 Resonance And At Least One Heavy Flavour Jet At The ATLAS Experiment Of The Large Hadron Collider", Saechsische Landesbibliothek- Staats- und Universitaetsbibliothek Dresden, 2012.

Publication

150 www.scribd.com <1 %
Internet Source

151 committees.web.cern.ch <1 %
Internet Source

152 Olive, Keith A.. "Testing the variation of fundamental constants with astrophysical and spectroscopic data.(Report)", Canadian Journal of Physics, April 2011 Issue <1 %

Publication

154

Aaij, R., B. Adeva, M. Adinolfi, A. Affolder, Z. Ajaltouni, S. Akar, J. Albrecht, F. Alessio, M. Alexander, S. Ali, G. Alkhazov, P. Alvarez Cartelle, A. A. Alves, S. Amato, S. Amerio, Y. Amhis, L. An, L. Anderlini, J. Anderson, M. Andreotti, J. E. Andrews, R. B. Appleby, O. Aquines Gutierrez, F. Archilli, P. d'Argent, A. Artamonov, M. Artuso, E. Aslanides, G. Auriemma, M. Baalouch, S. Bachmann, J. J. Back, A. Badalov, C. Baesso, W. Baldini, R. J. Barlow, C. Barschel, S. Barsuk, W. Barter, V. Batozskaya, V. Battista, A. Bay, L. Beaucourt, J. Beddow, F. Bedeschi, I. Bediaga, L. J. Bel, I. Belyaev, E. Ben-Haim, G. Bencivenni, S. Benson, J. Benton, A. Berezhnoy, R. Bernet, A. Bertolin, M.-O. Bettler, M. van Beuzekom, A. Bien, S. Bifani, T. Bird, A. Birnkraut, A. Bizzeti, T. Blake, F. Blanc, J. Blouw, S. Blusk, V. Bocci, A. Bondar, N. Bondar, W. Bonivento, S. Borghi, A. Borgia, M. Borsato, T. J. V. Bowcock, E. Bowen, C. Bozzi, D. Brett, M. Britsch, T. Britton, J. Brodzicka, N. H. Brook, A. Bursche et al. "Measurement of the forward Z boson production cross-section in pp collisions at $s = 7 \text{ TeV}$ ", Journal of High Energy Physics, 2015.

<1 %

155	www.weizmann.ac.il	<1 %
156	epub.uni-regensburg.de	<1 %
157	www.iop.org	<1 %
158	theory.fnal.gov	<1 %
159	lpc.fnal.gov	<1 %
160	cms.doe.gov	<1 %
161	dzero.phy.uic.edu	<1 %
162	www.civil.usyd.edu.au	<1 %
163	www.nastro.org.uk	<1 %
164	www.theophys.kth.se	<1 %
165	etd.lib.fsu.edu	<1 %

- 166 th-www.if.uj.edu.pl <1 %
Internet Source
- 167 www.phys.ufl.edu <1 %
Internet Source
- 168 www.ippp.dur.ac.uk <1 %
Internet Source
- 169 repository.liv.ac.uk <1 %
Internet Source
- 170 repositorium.sdum.uminho.pt <1 %
Internet Source
- 171 Held, Hauke. "Measurement of the Jet Momentum Resolution and Search for a light Standard Model Higgs Boson in the H(bb)W(lv) Channel with the CMS Detector at the LHC", Universität Karlsruhe, 2012. <1 %
Publication
- 172 Codispoti, Giuseppe <1979>(Castro, prof. Andrea). "Sensitivity of the Top quark mass measurement with the CMS experiment at LHC using t-tbar multijet simulated events", Alma Mater Studiorum - Università di Bologna, 2011. <1 %
Publication
- 173 Khachatryan, V., A. M. Sirunyan, A. Tumasyan, W. Adam, E. Asilar, T. Bergauer, J. Brandstetter, E. Brondolin, M. Dragicevic, J. <1 %

Erö, M. Friedl, R. Frühwirth, V. M. Ghete, C. Hartl, N. Hörmann, J. Hrubec, M. Jeitler, V. Knünz, A. König, M. Krammer, I. Krätschmer, D. Liko, T. Matsushita, I. Mikulec, D. Rabady, B. Rahbaran, H. Rohringer, J. Schieck, R. Schöfbeck, J. Strauss, W. Treberer-Treberspurg, W. Waltenberger, C.-E. Wulz, V. Mossolov, N. Shumeiko, J. Suarez Gonzalez, S. Alderweireldt, T. Cornelis, E. A. De Wolf, X. Janssen, A. Knutsson, J. Lauwers, S. Luyckx, S. Ochesanu, R. Rougny, M. Van De Klundert, H. Van Haevermaet, P. Van Mechelen, N. Van Remortel, A. Van Spilbeeck, S. Abu Zeid, F. Blekman, J. D'Hondt, N. Daci, I. De Bruyn, K. Deroover, N. Heracleous, J. Keaveney, S. Lowette, L. Moreels, A. Olbrechts, Q. Python, D. Strom, S. Tavernier, W. Van Doninck, P. Van Mulders, G. P. Van Onsem, I. Van Parijs, P. Barria, C. Caillol, B. Clerbaux, G. De Lentdecker, H. Delannoy, D. Dobur et al.
"Measurement of differential cross sections for Higgs boson production in the diphoton decay channel in pp collisions at $\sqrt{s}=8\text{ TeV}$ ", The European Physical Journal C, 2016.

Publication

Exclude quotes

Off

Exclude matches

Off

Exclude bibliography

Off